Using Deep Learning Approaches for Microwave Imaging

by

Vahab Khoshdel

A Thesis submitted to the Faculty of Graduate Studies of

The University of Manitoba

in partial fulfilment of the requirements of the degree of

DOCTOR OF PHILOSOPHY

Department of Electrical and Computer Engineering
University of Manitoba
Winnipeg, Manitoba, Canada

Abstract

This thesis investigates utilizing deep learning techniques to enhance Microwave Imaging (MWI). MWI has been used for a broad range of applications, from medical imaging and security to industrial engineering, subsurface prospection and stored-grain monitoring. Like other applications, medical imaging and stored-grain monitoring, which are of interest in this thesis, have recently received a lot of attention. While traditional MWI approaches have made great progress in recent years, there are still many fundamental challenges. Lower resolution compared to other imaging modalities, as well as the many reconstruction artifacts are the main challenges for MWI. In the first part of this thesis, in order to remove reconstruction artifacts and enhance the tomographic reconstructions of the complex-valued permittivity obtained using traditional MWI techniques in the breast imaging application, a 2D Convolutional Neural Network (CNN) based on the U-Net architecture is proposed. The proposed CNN takes in images obtained using the Contrast-Source Inversion (CSI) technique and attempts to produce the true image of the permittivity. The results demonstrate that the trained CNN not only removes common artifacts in CSI reconstructions, but also improves tumor detection performance.

Considering these promising results on 2D images and with the hope of being able to deal with 3D real-world microwave imaging problems, we expand the U-Net architecture to enhance the 3D reconstructed breast images as the second part of this thesis. A 3D CNN was developed and trained to improve the tomographic

reconstructions. Significantly, the results show that while the network is trained only with 3D images obtained synthetically, it works well with 3D images obtained from both synthetic and experimental data.

Finally, a novel CNN architecture is developed to replace the inversion technique itself. The proposed architecture is a multi-branch deep convolutional neural network designed to solve electromagnetic inverse scattering problems. Inspired by traditional iterative techniques for solving the electromagnetic inverse scattering problems, the proposed CNN architecture takes in scattered-field data and prior information to produce 3D images of grain moisture content in the stored-grain application. The proposed CNN's input is of two types: a complex-valued vector of scattered-field data, and a 3D image of the background moisture distribution as prior information. Thus, a multi-branch architecture consisting of decoder-only, and encoder-decoder, convolutional branches is proposed. The reconstructed moisture distribution images produced by the proposed CNN show that the network can not only reconstruct the 3D moisture distribution images directly from measured scattered-field data for high contrast objects-of-interest, but it also achieves a higher imaging quality compared with traditional inversion techniques in microwave imaging.

Contributions

The research contributions shown in this Ph.D. thesis are reported as three peer-reviewed journal papers. The Introduction, Conclusion and Future Work chapters are newly written. In all of these published works, the first author is the candidate, and the other authors are the candidate's advisors with the supervisory role.

It should be noted that other candidate's papers in which the candidate is not the first author have not been included in this thesis, but are listed below. The candidate's research has been published in prestigious journals, namely Sensors, Journal of Imaging, IEEE Access *, Neural Computing and Applications, and IEEE Journal on Multiscale and Multiphysics Computational Techniques. The full list of the candidate's publications are listed on the next page.

From the list of the publications presented below, the following articles have been included in this thesis in the form of a Chapter. These are [J1], [J2], [J3].

- **Articles Published in Refereed Journals**

[J1]. **Vahab Khoshdel** and Mohammad Asefi and Ahmed Ashraf and Joe LoVetri, "A Multi-Branch Deep Convolutional Fusion Architecture for 3D Microwave Inverse Scattering: Stored Grain Application" Submitted in *Neural Computing and Applications*, 2020.

[J2]. **Vahab Khoshdel** and Mohammad Asefi and Ahmed Ashraf and Joe LoVetri, "Full 3D Microwave Breast Imaging Using a Deep-Learning Technique" *Journal of Imaging*, vol. 3, no 4, pp. 864-875, 2020.

[J3]. **Vahab Khoshdel** and Ahmed Ashraf and Joe LoVetri, "Enhancement of Multimodal Microwave-Ultrasound Breast Imaging Using a Deep-Learning Technique" *Sensors*, vol. 19, Iss. 18, 2019.

[J4]. P. Mojabi, **V. Khoshdel** and J. LoVetri, "Tissue-Type Classification with Uncertainty Quantification of Microwave and Ultrasound Breast Imaging: A Deep Learning Approach," *IEEE Access*, (2020)

[J5]. P. Mojabi, M. Hughson **V. Khoshdel**, I. Jeffery and J. LoVetri, "CNN for Compressibility to Permittivity Mapping for Combined Ultrasound-Microwave Breast Imaging," Submitted in *IEEE Transactions On Multiscale and Multiphysics Computational Techniques*, (2020)

- **Conference Papers and Abstracts**

[C1]. **Vahab Khoshdel**, Ahmed Ashraf, Joe LoVetri, "Using a Deep-Learning Technique for Microwave-Ultrasound Breast Imaging", *PhotonIcs and Electromagnetics Research Symposium*, Rome, Italy, 2019

[C2]. Keeley Edwards, Kennedy Krakalovich, Ryan Kruk, **Vahab Khoshdel**, Joe LoVetri, Colin Gilmore, and Ian Jeffrey, " The implementation of neural networks for phaseless parametric inversion." *URSI GASS 2020*, Rome, Italy, 2020

Acknowledgments

I still remember my first meeting with Dr. LoVetri in his office and his words. Before that meeting, things were not looking so bright. I had no idea where my PhD was heading and whether it was possible to finish the PhD given my circumstances. Dr. LoVetri gave me hope and a chance to prove myself. First of all, thank you for being an awesome human being. I would also like to thank you for all your constant support, priceless guidance, and tireless efforts during the research at the University of Manitoba. You set a great example for me as a researchers, teacher and advisor.

I would also like to thank my co-advisor Dr. Ahmed Ashraf for all his priceless guidance from the first day. Without his support, I could not have done what I was able to do. I am also very thankful to my friends at the Electromagnetic Imaging Laboratory at the University of Manitoba.

I would like to express my appreciation for the time taken by my examining committee members: Prof. Ian Jeffery and Prof. Idris Elbakri from the University of Manitoba, and my External Examiner, Prof. Xudong CHEN, from National University of Singapore. I would also like to recognize the University of Manitoba for providing me the IGSES, IGSS, and UMGF scholarships, which helped me focus on my studies.

Finally, my deep and sincere gratitude goes to my family for their continuous and unparalleled love, help, and support. I am forever indebted to them for giving

me the opportunities and experiences that have made me who I am. They selflessly encouraged me to explore new directions in life and seek my destiny.

Table of Contents

List of Tables

List of Figures

1

Introduction

1.1 An Overview of Electromagnetic Imaging

Electromagnetic Imaging can be defined as inferring the internal structure of an object by interrogating it with electromagnetic fields (from static frequencies to microwave frequencies). Indeed, the purpose of electromagnetic imaging and specifically Microwave Imaging (MWI), is the imaging of some internal propertie(s) of objects or regions of interest (OI/ROI) from the knowledge of measured scattered field information. As a non-destructive imaging technique, MWI utilizes information obtained only from outside the ROI. MWI has been widely used in a broad range of applications such as geophysical surveying [1,2], medical imaging [3,4], stored-grain monitoring [5], industrial non-destructive testing [6], and security screening [7].

In the research presented herein, electromagnetic imaging for breast imaging and stored grain monitoring has been investigated. For breast imaging, electromagnetic fields are at the microwave frequency range (300 MHz-30 GHz), and for the grain monitoring are at the radio frequency range. It should be noted that while this thesis focuses on these two applications, similar approaches could be applied for other electromagnetic imaging applications.

MWI for medical applications has attracted significant attention in recent decades. The physics behind microwave medical imaging is that different tissues have different dielectric properties at microwave frequencies. It has been shown that the dielectric properties of abnormal tissue (e.g., malignant tissue) are significantly different than that of normal tissues [8, 9]. This difference in dielectric values is detectible as a contrast in the reconstructed microwave image.

Electromagnetic Imaging for stored grain monitoring has been recently proposed [10,11]. The possibility of using electromagnetic waves to quantitatively image grains, and the motivation to do so, derives from the well-known fact that the dielectric properties of agricultural products vary with their physical attributes, such as the moisture content and the temperature, which, in turn, indicates their physiological state.

1.1.1 Microwave Imaging Terminology

Here, the terminology typically used with MWI as used in this thesis is introduced. MWI is used to reconstruct the constitutive parameters (complex permittivity ϵ and permeability μ) of an object of interest, e.g., the breast, or a region-of-interest (ROI), in the stored-grain imaging application. In the breast imaging application, transmitters (antennas and/or probes) surround the OI and use electromagnetic signals in the microwave frequency range (0.3 GHz to 300 GHz) to interrogate the OI. In the stored-grain imaging application, the transmitters and receivers are imbedded at the periphery of the ROI to collect data. When one antenna acts as a transmitter the others antennas act as receivers in the system and a vector network analyzer (VNA) is used to measure the electromagnetic energy flowing between the two antennas to infer the internal composition of the OI's constitutive parameters. Using this collected

data, one reconstructs the distribution, i.e., image, of the constitutive parameters within the imaging domain.

The image can be quantitative, where actual numerical values for the property being reconstructed are given, or qualitative, where relative values of the contrast induced by the varying properties are included in the image. For traditional quantitative imaging, which is of concern in this thesis, a numerical inversion model is used in optimization-based methods. Based on the system's numerical inversion model, expected receiver field estimates are produced using a calculation tool called a "forward solver". The "inverse solver" is the optimization-based computational tool that produces an image of the OI using the measured fields from the MWI system and forward solver. Figure 1.1 shows an overview of this procedure.

A simplified diagram of an MWI system is shown in Figure 1.2. It should be borne in mind that every transceiver can send and receive a signal but not simultaneously. A simplified OI is depicted with only two regions: one with constitutives ϵ_1 and μ_1, and another with constitutives ϵ_2 and μ_2. The area where the OI is bounded is our imaging domain $\mathcal{D}$, and $\mathcal{S}$ is a discrete measurement surface where the transceivers are located. Ω is defined as the system's boundary, and, for the systems considered in this thesis, a metallic surface comprises either all or part of the boundary is used to indicate the system's boundary. Using a metallic system boundary offers many benefits to MWI, such as accuracy in boundary modeling and the ability to isolate the inside of the chamber from the transceiver cables electromagnetically, and anything else outside the boundary [12]. In Figure 1.2, (a) and (b) show a simple MWI system and its numerical model, respectively. In this particular case, the depiction shows the use of FEM where the numerical model breaks the problem area into mesh elements. Typically, mesh elements are triangles in 2-D and tetrahedrals in 3-D to approximate

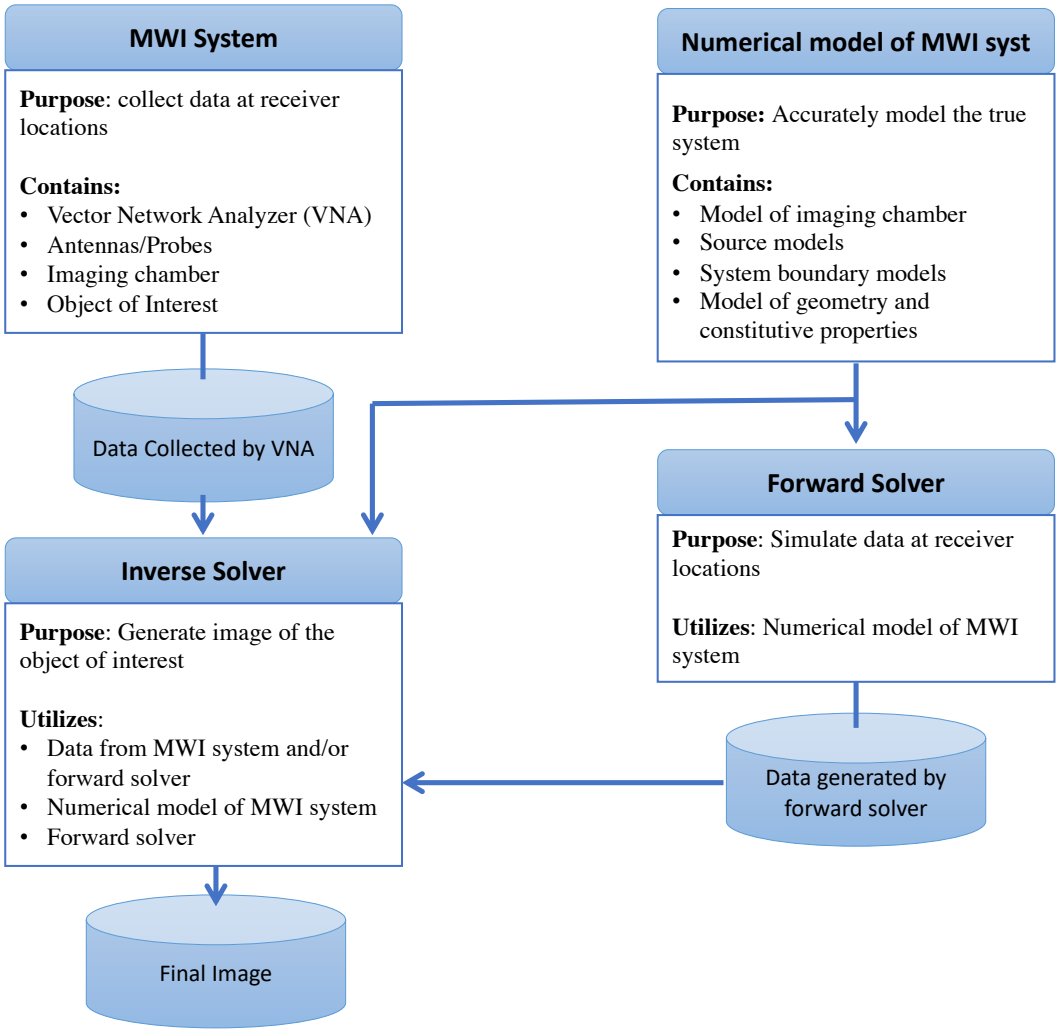

Figure 1.1: An overview of the hardware and software used in MWI. Data is collected by a MWI system and used by an inverse solver to create an image. This requires a numerical inversion of the MWI system including an arbitrary OI. The forward solver simulates the data collected at the receivers.

the different shapes and boundaries in the actual system. Each element can have a constant value of permittivity and permeability; therefore, to have an accurate model, mesh elements should line up with the geometry of OI. Transceivers and boundaries in the system should be approximated by the numerical model. In this thesis the transceivers are modelled as ideal electric or magnetic dipoles and the metal boundary as Perfect Electric Conductors (PECs)- more details on the transceivers can be found in [13]. It is clear that the forward solver's ability to model the system and OI accurately has a significant effect on the reconstruction quality.

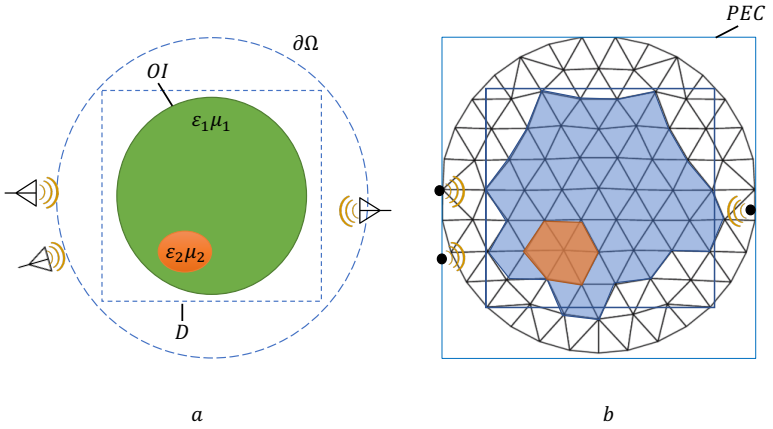

Figure 1.2: A microwave imaging setup for breast cancer imaging. Data collected by the receivers on the measurement surface S is used to reconstruct an object of interest in the imaging domain $\mathcal{D}$

The inverse problem can be considered as an optimization problem because it attempts to minimize an error functional, the simplest of which would be the difference between the measured fields and those fields produced by the forward solver. It updates the reconstructed image iteratively by reducing the difference between actual fields and simulated fields. Note that this example simplifies the real MWI problem slightly to improve clarity. For instance, while the reconstruction in this example

shows only two areas, the actual image is a more complex permittivity map, where the permittivities of each element in the numerical model are different.

1.1.2 Forward Solvers

Forward solvers are employed by imaging techniques to simulate the resulting electromagnetic field when a transmitter radiates in the presence of the OI. Forward solvers are formulated in the time-domain or frequency-domain (also known as time-harmonic). The frequency-domain algorithm is often used for quantitative imaging methods since they usually have better signal-to-noise ratio and collecting frequency-domain data is simpler than collecting time-domain data. However, these techniques are computationally expensive.

To solve the forward problem, time-harmonic algorithms can be implemented as integral equation (IE) or partial differential equation (PDE) solvers. In the case of complex system geometries or inhomogeneous backgrounds, since computing the numerical Green's function is expensive, it has been shown that PDE solvers have better performance [14, 15]. The finite-element method FEM [16] and the finite-difference method (FDM) [17] are two common time-harmonic PDE forward solvers. Both methods are able to support inhomogeneous backgrounds [18,19], and FEM can support high-order polynomial field expansions [20]. FEM can support unstructured grids, while FDM because of having geometric modelling errors due to the required grid structure of the discretization, can not. The other side of the picture is that compared with FDM, FEM is a more complicated method.

The Discontinuous Galerkin Method (DGM) has recently been developed and utilized as the forward solver for MWI. DGM is a flexible forward solver that could use electric and/or magnetic field data to reconstruct the electric and/or magnetic tar-

gets. DGM is a time-harmonic PDE solver; therefore, it can support inhomogeneous backgrounds. Compared with other techniques, DGM has several desirable features which are described in full detail in [13].

1.1.3 Imaging Algorithms (Inverse Solvers)

In order to solve the inverse problem, imaging algorithms use the measurement data collected at several locations surrounding the OI from which one estimates several attributes of the OI. Ill-posedness and nonlinearity are considered the main challenges in inverse problems which the imaging algorithm must overcome. As defined by Hadamard, the mathematical inverse problem is ill-posed [21], because the solution might be non-unique, unstable (small changes in the measured area cause large differences in the reconstructed image), and/or nonexistent. One of the aspects that makes inverse problems for MWI ill-posed is that there is a null space in the standard error-norm functional that compares the collected data to that generated by the forward model. Also, since both the constitutive parameters and fields within the OI are unknown and multiplicatively contribute to the fields outside the OI, it is nonlinear.

Computational complexity is the next challenge of inversion techniques [22]. This problem is more severe when we are dealing with real-world imaging problems, because they often must be solved in 3D to reduce modelling error. Researchers attempt to alleviate this challenge by performing the majority of computations in parallel [23].

As previously mentioned, inversion algorithms associated with MWI can be divided into qualitative and quantitative techniques. In qualitative methods such as radar-based methods, the image is reconstructed into different scattering regions without corresponding quantitative values. The reduction of computational complexity

is the advantage of these methods; however, since they only reconstruct relative contrast values within the object of interest, they are less useful for medical diagnostic applications. For instance, consider a qualitative breast image in which several small scatterers are reconstructed within the breast - without having the quantitative parameters of these scatterers it is difficult to distinguish them between tumours and high-contrast healthy breast tissue [13].

Quantitative imaging methods attempt to reconstruct the permittivity and/or permeability maps. The two main categories of quantitative imaging methods are global optimization methods (e.g., Genetic Algorithms) and local optimization methods (e.g., Gradient-based techniques such as CSI [24] and Gauss-Newton inversion (GNI) [25]). Global optimization attempt to optimize over the entire solution space, and therefore more forward solves are needed, which makes them computationally more expensive than local optimization methods.

By using regularization techniques, Gradient-based approaches are able to deal with the ill-posedness of the inverse problem [14,26,27]. In addition, iteratively reconstructing the OI by minimizing a cost-function enable the gradient-based approaches to deal with the nonlinearity.

In all the work presented in this thesis, the Finite Element Contrast Source Inversion (FEM-CSI) is used as the inversion technique. CSI is the inversion algorithm, and FEM is the forward solver it employs. The Electromagnetic Imaging Laboratory (EIL), at the University of Manitoba, has been researching and developing 2D and 3D FEM-CSI for years. This technique is implemented as a fully parallel production code that can be used in many scientific and industrial applications [5, 11, 14, 19, 28]. This implementation is a time-harmonic PDE solver that supports electric or magnetic field measurement data and inhomogeneous backgrounds. The CSI technique

with full detail is described in [24], but is briefly described it in Section 2.3.

1.2 Research Rationale and Objectives

Despite all the advances in microwave imaging and electromagnetic inversion techniques, it is well-known that due to non-linearity and the ill-posedness of the inverse scattering problem, the reconstruction of the complex and irregular scatterer is still a challenging task [29]. Reconstruction artifacts, low resolution compared with other modalities, and high computational cost are the main challenges for traditional electromagnetic inversion techniques [19, 30–32].

Recently, Deep Learning techniques (DL), especially the Convolutional Neural Networks (CNNs), have opened many exciting avenues to solve different scientific and technical problems. These include applications such as natural language processing, speech recognition, and computer vision [33].

CNNs are deep neural networks originally designed to process images. In CNNs, the parameterized local convolutions, at successively subsampled image-sizes, allow the learning of feature maps at multiple scales of pixel-organization [33]. Historically, CNNs were mainly used for image classification [34–36]. However, with the advent of encoder-decoder architectures [37, 38], CNNs, and their variants are increasingly being used for learning tensor-to-tensor (e.g. image-to-image, or vector-to-image) transformations, thereby enabling various data-driven and learning based image reconstruction applications [39].

CNNs have also been applied to medical imaging for segmentation [40, 41], as well as detection and classification [42–44]. Using deep learning methods for the common modalities of medical imaging, such as MRI [45] and Ultrasound [46–48], has been well studied. Considering the promising result of using DL methods for other imaging

modalities and the existing challenges in traditional electromagnetic inversion techniques, investigating how deep learning can be used to facilitate microwave imaging is a great need. Consequently, researchers have recently begun to take advantage of machine learning opportunities to improve Microwave Imaging (MWI) performance. In Section 1.3, some of these primary studies are reviewed. Despite all these successes, insight on the best approach of combining DL with the knowledge of the underlying physics as well as traditional non-learning techniques for MWI is an open question. Therefore, this dissertation investigates utilizing deep learning methods, specifically CNNs in different aspects of microwave imaging.

Considering the entire processes of microwave imaging, potentially, CNNs could be utilized in at least five different ways. First, one could use CNNs as a post-processing technique to enhance the reconstructed images obtained from traditional inversion techniques. The second idea is using CNNs for data calibration. Thirdly, we can use CNNs to replace the inversion technique itself, where the CNN will generate images from the calibrated or synthetic data. Fourth, we can use CNNs to simultaneously replace both the inversion algorithm as well as calibration, allowing us to go from measured data to an image. Finally, there is the possibility of using a deep CNN to perform the whole process: from experimental data right to the image. A schematic of the microwave imaging processes and the five mentioned options for using CNNs is shown in Figure 1.3.

In this thesis, we first examine the use of deep convolutional neural networks as a post-processing technique to enhance the 2D reconstructed images in dual-mode MW/US breast imaging. In order to generate the input for the proposed deep learning technique, first we perform preliminary (rough) reconstructions of the complex-valued permittivity using the contrast source inversion (CSI) technique. CIS is considered

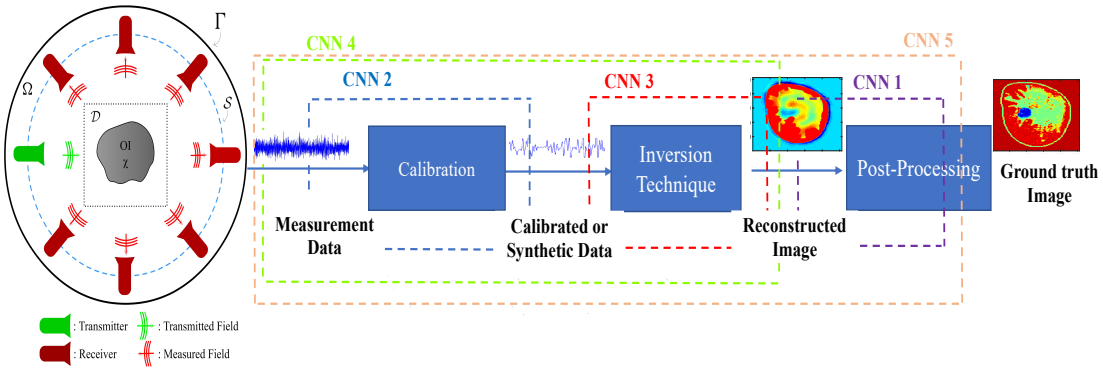

Figure 1.3: Schematic describing options for using CNNs in the microwave imaging process.

one of the most successful traditional iterative algorithms for solving the inverse problems associated with MW breast imaging (Section 2.3 describes CSI technique in more detail). Imaging algorithms, specifically CIS, is known to produce imaging artifacts in its reconstructed outputs, which makes it difficult to use these reconstructions for further image analysis, such as tumor detection, tissue type classification, and image segmentation. This is true even when ultrasound-derived tissue regions are utilized as prior information in dualmode reconstructions. Therefore to remove these artifacts, a U-Net-based convolutional neural network is trained that takes a rough CSI reconstruction as input and attempts to produce the true image of the complex tissue permittivity (CNNs is utilized as a post-processing technique like CNN1 in Figure 1.3). The developed U-Net based architecture consists of successive convolutional and downsampling layers, followed by successive deconvolutional and upsampling layers. Moreover, the skip connections between the corresponding contractive and expansive layers keep the gradients from vanishing that helps in the optimization process [35,37]. To use a U-Net for reconstruction, the original objective of the U-Net is replaced with

the sum of pixelwise squared reconstruction errors between the true real part of permittivity and the output of U-Net [35]. In this chapter, we also quantify the ability of the developed U-Net to categorize and identify tissues in CSI reconstructed images. The specific goal now is to detect tumors within breast images of the reconstructed real and imaginary parts of the complex-valued permittivity.

The following chapter expands the proposed CSI-Deep-Learning technique for 3D images of the complex-valued permittivity of the breast. Although 2D imaging allows us to develop and study several techniques and strategies —since, in real-world problems, physical measurements are 3D phenomena— developing a 3D CNN is crucial. Several studies have provided convincing arguments to demonstrate the importance of using full 3D imaging and 2D imaging limitations. [49]. Consequently, in this chapter, we have expanded the U-Net architecture to be able to reconstruct 3D images from 3D CSI results. To train the CNN, the 3D artifact-laden CSI reconstructed images are fed to the network as inputs and the network attempts to generate the true permittivity image of the breast. The results show that not only does the trained CNN work well with synthetic images, but it also performs well with images created using experimentally obtained microwave scattered-field data from an MWI system: the same MWI system for which a numerical model was utilized in the creation of the synthetic 3D images.

In addition to challenges in obtaining highly accurate reconstructions of the complex-valued permittivity by traditional iterative methods, for most cases the permittivity, an electromagnetic property, is not the desired final outcome. In biomedical imaging, for example, the desired result may be an image of tissue-types [50], or a classification of cancerous versus non-cancerous tissues (*i.e.*, tumor or cancerous tissue detection). In the stored-grain application, one is interested in the moisture content of the grain

as a function of position within the grain bin. Therefore, we ask whether a subsequent mapping can be implemented to convert the permittivity into the desired outcome. While some advancement has been made in this direction, such a mapping is challenging to incorporate directly into traditional inverse scattering algorithms [51]. In order to overcome all these challenges, a multi-branch deep convolutional fusion architecture is proposed. While previous chapters used CNNs as a post-processing technique to enhance the reconstructed images, this chapter proposes two novel CNN architectures to replace the inversion technique itself. Inspired by objective-function techniques for solving the electromagnetic inverse scattering problems, the CNN architecture producing the best results takes in the scattered field data and prior information to produce 3D images of the moisture content. Since we have inputs of different formats, i.e. complex-valued vector of scattered field data and a 3D image volume of prior information, we develop a multi-branch architecture consisting of decoder-only, and encoder-decoder, convolutional branches. The two branches are later fused to produce the final reconstructed 3D image.

It is clear that training the proposed deep-learning-based inversion model needs a large dataset consisting of different models. Due to the lack of a large enough dataset of microwave imaging for breast, in this chapter, we consider another important application, stored grain monitoring, for which we could gather considerable amount of training data. The input-output pairs consist of scattered field data and prior information, along with the true numerical grain bin images which were synthetically generated are used to train the CNN. The trained CNN model achieves a higher imaging quality compared with traditional inversion techniques in microwave imaging. It should be noted that using the trained CNN models enable us to use microwave imaging for quasi-real-time monitoring applications by eliminating the reconstruction

time.

1.3 Background on Using Deep Learning for Microwave Imaging

Researchers have begun using machine learning techniques to improve microwave imaging (MWI) performance. State-of-the-art deep-learning-based MWI techniques fall into two categories: a learning-assisted objective-function approach and a direct learning approach. In the first category, deep learning has been combined with one of the traditional algorithms to enhance electromagnetic inversion's performance (Like CNN1 and CNN2 in Fig 1.3).

As one of the early attempts in the first category, Caorsi and Gamba applied a fully connected NN with one hidden layer to detect simple cylindrical objects inside a given domain of interest and restore their geometric and electrical properties [52]. Their proposed model takes in the electric field values scattered by the object and attempts to retrieve the position, radius, and dielectric permittivity of an unknown circular cylinder. They have shown that a well-trained neural network is able to perform this task. These promising results pointed out that neural network models could be utilized in the electromagnetic inverse scattering problems.

Shah et al. also proposed a convolutional neural network to learn the nonlinearity inherent in microwave imaging [53]. In this technique, the authors developed a deep-learning-based technique to estimate the total electric field from an approximation that is obtained by a Born-approximated solution. Results illustrate the capability of the proposed technique for a 2D breast microwave imaging problem. In fact, the results demonstrate that the proposed technique is able to estimate the total electric

field with high accuracy to the true total electric field, and then it could improve contrast recovery.

Gerazov and Conceicao have investigated the tumor-type classification for inhomogeneous breast tissues in medical microwave imaging by using a deep learning technique [54]. In this study, a dataset of Finite Difference Time Domain (FDTD) numerical simulations of tumour models embedded in homogeneous breast adipose tissue is used. The proposed architecture is a two-step technique; the first part is designed for preprocessing and feature extraction from the FDTD simulation results. Then these features are fed into the trained deep learning based classifier. The results show that the use of deep neural networks is beneficial and can improve the classification performance.

Wang and Xu developed a deep convolutional neural network technique, namely super-resolution CNN, which can generate high-resolution breast images from low-resolution models [55]. Note that the holographic microwave imaging technique is used to obtain the image datasets. Their experimental tests also showed that the proposed CNN improved the image quality, and the enhanced images have the potential for microwave breast tumor detection.

Recently, Li et al. tried to utilize a deep neural network for nonlinear electromagnetic inverse scattering. They have demonstrated the capability of the proposed DNN in learning a general model approximating the underlying EM inverse scattering system. However, the targets used were simple, uniform, low contrast targets. In addition, while in real-world imaging problems, the electromagnetic fields scatter and propagate through three-dimensional (3D) objects, this research is limited to two-dimensional inversion problems [56]. It has been shown that having a viable 3D imaging technique is vital for having an appropriate reconstruction technique [23].

Most recently, Edwards et al. have used a machine learning technique for the parametric inversion of grain bin measurements. The proposed neural network can obtain four inversion parameters (grain height, cone angle, and bulk real and imaginary permittivity of the grain) from uncalibrated experimental data, which could then be used as prior information for the traditional microwave imaging techniques. Interestingly, they have shown that the trained NN on synthetic data sets also works well with experimental data, which is crucial for practical applications. Their results illustrate that compared with existing optimization-based parametric inversion methods; the machine learning model is a faster and more cost-effective long-term solution [57].

In the second category, deep learning techniques are employed to reconstruct an image directly from measurement data (Like CNN2, CNN4, and CNN5 in Figure 1.3). While promising studies have been performed for other imaging modalities, like MRI [45] and Ultrasound [46], there is a great need to investigate how deep learning can be utilized to perform the inversion in microwave imaging.

The early attempts to solve the inverse scattering problem for microwave imaging have been investigated by Rekanos, in which he utilized radial basis function neural network to solve the inverse scattering problem of microwave imaging [74]. The proposed radial basis function neural network was trained to estimate the position and the size of proliferated marrow inside the bone of a limb.

Recently, to tackle the well-known electromagnetic inverse scattering problem's challenges, Yao et al. proposed a novel two-step machine learning-based technique [58]. In the first step, a deep convolutional neural network with complex values is used to obtain the initial contrast (permittivities) of the dielectric scatterers from the measured scattering data. In the second step, a complex-valued deep residual

convolutional neural network takes in the previously obtained contrast to enhance the image reconstruction. Numerical tests have shown that the proposed technique can improve the accuracy of image reconstruction.

Wei and Chen proposed using a deep learning technique based on the U-Net architecture to solve nonlinear inverse problems, where pixel bases represent scatterers [59]. This research has developed three different training schemes, including direct inversion, backpropagation, and dominant current schemes. In the direct inversion scheme, the complex scattered fields were directly used to retrieve profiles of relative permittivities. In contrast, in the other two schemes, CNN is combined with back-propagation and dominant current techniques, respectively. Surprisingly, results demonstrate that the proposed direct inversion technique has a better performance than the other two schemes in terms of accuracy. It should be noted both synthetic and experimental data have been used to evaluate the proposed methods.

Ran et al. also tried to apply CNN to the time-harmonic electromagnetic diagnostic of a dielectric microstructure [60]. They have employed a multisource-multireceiver configuration in a free-space to provide the discrete scattered fields and used a method of moments (MoM) to model the field. Indeed similar to the chapter, they have focused on using CNN to replace the inverse solver. To evaluate the proposed CNN scheme is compared with the contrast-source inversion (CSI) technique. Results show that the proposed CNN outperforms the CSI results. Although these results are significant, the targets they used are simple homogeneous targets with low contrast.

This chapter has tried to review the most related articles on using deep learning techniques for electromagnetic imaging. A summary of papers that are considered here is provided in Figure 1.4. Also, very recently, Chen et al. have tried to review and summarize most state-of-the-art deep learning methods for solving inverse scattering

problems [61]. They also tried to reviews the promises and pitfalls of deep learning for inverse scattering problems.

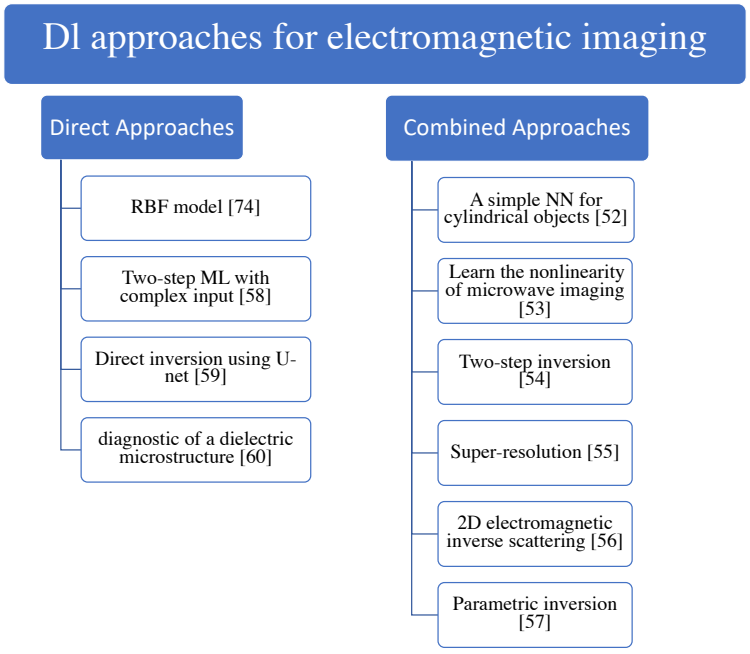

Figure 1.4: A summary of papers that study using machine learning approaches for microwave imaging

2

Paper1: Enhancement of Multimodal Microwave-Ultrasound Breast Imaging Using a Deep-Learning Technique

---

2.1 Abstract

We present a deep learning method used in conjunction with dual-modal microwave-ultrasound imaging to produce tomographic reconstructions of the complex-valued permittivity of numerical breast phantoms. We also assess tumor segmentation performance using the reconstructed permittivity as a feature. The contrast source inversion (CSI) technique is used to create the complex-permittivity images of the breast with ultrasound-derived tissue regions utilized as prior information. However, imaging artifacts make the detection of tumors difficult. To overcome this issue we train a convolutional neural network (CNN) that takes in, as input, the dual-modal CSI reconstruction and attempts to produce the true image of the complex tissue permittivity. The neural network consists of successive convolutional and downsampling layers, followed by successive deconvolutional and upsampling layers based on the U-Net architecture. To train the neural network, the input-output pairs consist of CSI's dual-modal reconstructions, along with the true numerical phantom images

from which the microwave scattered field was synthetically generated. The reconstructed permittivity images produced by the CNN show that the network is not only able to remove the artifacts that are typical of CSI reconstructions, but can also improve the detectability of tumors. The performance of the CNN is assessed using a four-fold cross-validation on our dataset that shows improvement over CSI both in terms of reconstruction error and tumor segmentation performance.

2.2 Introduction

In quantitative microwave imaging, scattered-field data arising from the illumination of an object-of-interest (OI) by microwave energy is acquired via a data-acquisition setup. From the collected scattered-field data one then seeks to infer, or *reconstruct*, information about the spatial distribution of the physical properties of the OI that affect the scattering process, *i.e.* its permittivity. The reconstruction is in the form of two quantitative images corresponding to the real and imaginary parts of the complex-valued permittivity.

Mathematically, the so-called inversion of the scattered-field data to reconstruct an image of the physical properties is accomplished by solving an *inverse problem*. Typically, a numerical forward model that relates any particular distribution of properties to the collected data is introduced into the inverse problem. The more general the reconstruction model the more difficult solving the inverse problem becomes, often leading to what are known as ill-posed inverse problems. Ill-posedness means that there may be no or many possible distributions of the properties that lead to the data (*i.e.*, non-existence and non-uniquenes of solutions to the mathematical inverse problem), and that small changes in the data may lead to arbitrarily large changes in the inferred distributions of the properties (*i.e.*, instability of the solution). Note

that ill-posedness is a property of the mathematical formulation of the inverse problem corresponding to a particular setup of the wavefield process. One may attempt to change the physical process being used to collect the scattered-field data but ultimately the ill-posedness arises because of the limited amount of data one is able to collect as well as the fact that the data must be collected remotely, *i.e.* away from the location of the properties one is wanting to infer.

This is indeed the case for the inverse problems associated with quantitative microwave imaging (MWI) [62] and ultrasound imaging (USI) [63, 64]. Both MWI and USI attempt a quantitative reconstruction of the spatial distribution of the physical properties affecting the wavefield processes associated with each of these modalities. In MWI one seeks to reconstruct the complex-valued permittivity of the OI, whereas in USI one reconstructs, *e.g.*, the complex-valued compressibility and the mass-density of the OI. It has long been recognized that the reconstructions of physical properties, such as permittivity, would be extremely useful for medical imaging since different kinds of biological tissues have been shown to have distinct electrical properties. For the detection of breast cancer significant effort has gone into the characterization of breast tissues [8].

There have been significant advances in the use of microwave imaging for breast cancer detection and monitoring during the past two decades [65, 66]. Microwave breast imaging techniques generally split into those that produce a qualitative image of the breast's interior structure and those that produce a quantitative image of the complex permittivity of the breast tissues. Quantitative techniques take advantage of the different dielectric properties of normal breast tissue (e.g., skin, adipose, and fibroglandular) and cancerous tumors [8, 9]. The main approach for solving ill-posed inverse problems associated with quantitative MW/US breast imaging are computa-

tionally expensive iterative methods where the inversion model consists of a numerical solution of a complex electromagnetic or ultrasound scattering problem [64, 66]. While such iterative methods have improved dramatically over the years, providing improved resolution and accuracy of the reconstructed properties, as well as more efficient implementations, there are still many fundamental trade-offs between these three aspects due to operational, financial, and physical constraints [66]. The greatest challenge to MWI becoming clinically accepted for breast imaging is its lower resolution compared to other biomedical modalities as well as the many reconstruction artifacts that are produced related to the nonlinearity and ill-posedness of the associated inverse problem. Progress in MWI has recently been made by incorporating prior information obtained from some alternate modality. For instance, it has recently been shown that spatial segmentation priors derived from magnetic resonance imaging or Xray computed tomography can significantly improve MWI [67]. In this paper we take advantage of the recent progress in a multimodal ultrasound/microwave imaging procedure wherein the breast region is first segmented into tissue regions using an ultrasound (US) technique and subsequently these tissue-regions are incorporated as prior information into either a qualitative, [68], or quantitative microwave imaging technique [69].

Deep learning is currently an extremely active research area that has produced huge successes in a broad range of applications such as speech recognition, computer vision, and natural language processing [33]. Researchers have begun to investigate how deep learning techniques can be effectively applied in biomedical imaging and inverse problem [70] [43]. Studies have shown that deep learning can provide state-of-the-art performance for tumor classification [54], segmentation [40], and the post-processing of X-ray CT images [71] [72].

Neural networks have recently been combined with microwave image construction techniques as a means of learning the forward model for a complex data-acqusition system [73]. Also, Rekanos has proposed using radial basis function neural networks to solve a simple inverse problem associated with the microwave imaging [74]. In this technique they estimate the position and size of proliferated marrow inside bone. Most recently, Li et. al have studied how deep neural networks can be used to take microwave images created using the back-projection (BP) method and have the network output a much improved image [75]. This by-passes the use of iterative techniques to solve the full nonlinear electromagnetic inverse problem as back-projection is a linear construction technique. The results of that work are significant because they show how a network trained using only BP images obtained from synthetically generated data can then generalize to BP images created using experimental data. Although the generalization to experimental data is significant, the targets they used are simple homogeneous targets with low contrast. That is, the targets used by them for training the network had no internal structure. To the best of our knowledge utilizing deep learning techniques to enhance microwave imaging for high contrast objects-of-interest that have complicated internal structure, such as the breast imaging application that we consider herein, have not been previously studied.

In this paper, we explore one method of utilizing deep learning in dual-mode MW/US breast imaging that utilizes the Contrast Source Inversion (CSI) technique. In addition, we quantify the developed framework's ability to categorize and/or identify tissues in the images. The specific goal is to identify tumors within breast images of the reconstructed real and imaginary parts of the complex valued permittivity.

2.3 CSI-Deep-Learning Microwave Breast Imaging

2.3.1 Contrast Source Inversion

The first part of the CSI-Deep-Learning technique developed herein is to perform preliminary (rough) reconstructions of the complex-valued permittivity using the CSI technique. Traditionally, regularized iterative algorithms have remained the method of choice for solving inverse problems associated with MW breast imaging. Since its creation in 1997 the CSI technique has become a leading numerical optimization based reconstruction method for inverse problems [24]. The method can be briefly described as follows for the type of 2D Transverse-Magnetic tomographic reconstructions considered herein. We define an imaging domain, $\mathcal{D}$, within the problem domain Ω of a MW or US (wavefield) imaging setup as shown in 2.1. An unknown isotropic, non-magnetic OI is located in $\mathcal{D}$ and is surrounded by a background medium of known electrical and acoustic properties. The complex relative permittivity of the OI is $\epsilon_r(\boldsymbol{r})$, where $\boldsymbol{r}$ is a 2D position vector. The corresponding electric contrast is defined as $\chi(\boldsymbol{r}) \triangleq (\epsilon_r(\boldsymbol{r}) - \epsilon_n(\boldsymbol{r}))/\epsilon_n(\boldsymbol{r})$ where $\epsilon_n(\boldsymbol{r})$ is an imposed numerical background complex relative permittivity (with $\chi(\boldsymbol{r}) = 0$ for $\boldsymbol{r} \notin \mathcal{D}$), which may be inhomogeneous so as to represent any prior information we wish to impose (notice that at any location where $\epsilon_n(\boldsymbol{r}) = \epsilon_r(\boldsymbol{r})$ the contrast will be zero). With the OI in $\mathcal{D}$ a total field E_t is produced by a source t and is measured at points located on a measurement surface $\mathcal{S}$. An incident field E_t^{inc} is defined when there is no OI in $\mathcal{D}$; rather the region is occupied by the imposed (known) numerical background $\epsilon_n(\boldsymbol{r})$. The scattered

electric field is then defined by $E_t^{\text{sct}} \triangleq E_t - E_t^{\text{inc}}$ and satisfies the scalar Helmholtz equation $\nabla^2 E_t^{\text{sct}}(\boldsymbol{r}) + k_n^2(\boldsymbol{r}) E_t^{\text{sct}}(\boldsymbol{r}) = -k_n^2(\boldsymbol{r}) w_t(\boldsymbol{r})$ where $k_n(\boldsymbol{r}) = \omega\sqrt{\mu_0 \epsilon_0 \epsilon_n(\boldsymbol{r})}$ is the wavenumber in the imposed numerical background, and $w_t(\boldsymbol{r}) \triangleq \chi(\boldsymbol{r}) E_t(\boldsymbol{r})$ is the contrast source that produces the scattered field for that transmitter.

The boundary-value problem (BVP) defined by this second-order Partial Differential Equation (PDE) and the boundary conditions is solved using the Finite-Element Method (FEM) [76]. Thus, the problem domain (Ω) is divided into a mesh of triangular elements upon which linear-basis functions are specified whose parameters are dependent only on the geometry of the mesh. Applying FEM to the BVP discretizes the problem producing a matrix equation for the unknown scattered-field in terms of the contrast source (for each transmitter t).

The inverse problem is that of minimizing the CSI cost-functional that is defined with respect to the contrast sources, w_t, and the contrast, χ. This functional is constructed as the sum of normalized data-error and domain-error functionals written as

$$\begin{aligned} \mathcal{F}^{\text{CSI}}(\chi, w_t) &= \mathcal{F}^{\mathcal{S}}(w_t) + \mathcal{F}^{\mathcal{D}}(\chi, w_t) \\ &= \frac{\sum_t \|f_t - \boldsymbol{\mathcal{M}}_{\mathcal{S}} \boldsymbol{\mathcal{L}}[w_t]\|_{\mathcal{S}}^2}{\sum_t \|f_t\|_{\mathcal{S}}^2} + \\ &\quad \frac{\sum_t \left\|\chi \odot E_t^{\text{inc}} - w_t + \chi \odot \boldsymbol{\mathcal{M}}_{\mathcal{D}} \boldsymbol{\mathcal{L}}[w_t]\right\|_{\mathcal{D}}^2}{\sum_t \|\chi \odot E_t^{\text{inc}}\|_{\mathcal{D}}^2} \end{aligned} \tag{2.1}$$

For each transmitter t, f_t holds the measured scattered-field data at the receiver locations, E_t^{inc} is the vector of incident field mesh values inside $\mathcal{D}$. The matrix $\boldsymbol{\mathcal{L}}$ is the inverse of the FEM matrix operator that transforms contrast source variables w_t in $\mathcal{D}$ to scattered field values within the whole domain Ω. The operator $\boldsymbol{\mathcal{M}}_{\mathcal{S}}$ transforms

field values from Ω to receiver locations on the measurement surface $\mathcal{S}$ whereas the operator $\boldsymbol{\mathcal{M}}_{\mathcal{D}}$ transforms values from Ω to points inside $\mathcal{D}$. The vector χ holds the contrast over the FEM mesh nodal values located inside $\mathcal{D}$. The notation $a \odot b$ denotes the Hadamard (*i.e.*, element-wise) product. The CSI objective functional $\mathcal{F}^{\text{CSI}}(\chi, w_t)$ is minimized by updating the contrast source w_t and the contrast χ variables sequentially.

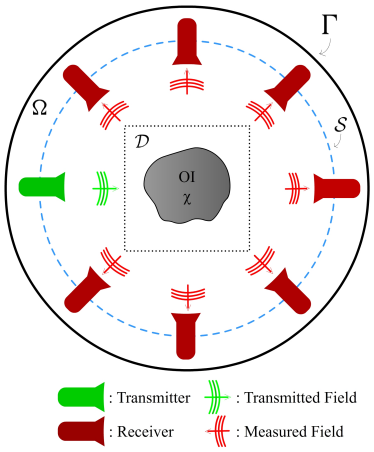

Figure 2.1: Schematic representation of a wavefield imaging setup

On its own, CSI is not able to effectively reconstruct the high-contrast complex-valued permittivities associated with breast tissues, but recent advances have shown that incorporating prior information regarding the location of specific tissue regions into CSI as an inhomogeneous numerical background leads to much improvement [19, 30]. Even so, the algorithm still produces imaging artifacts that make further image analysis difficult. In [77], it was shown how US-derived prior tissue regions can greatly improve reconstructions based on qualitative radar techniques. Herein, we use these US-derived tissue regions as prior information for CSI-based MWI.

2.3.2 Machine Learning Approach to Reconstruction

One of the main reasons for imaging artifacts in CSI reconstructions is the possibility of a non-realistic map of permittivities producing realistic measurement data. Any numerical optimization algorithm is thus prone to getting stuck in a bad local minima corresponding to non-realistic map of permittivities. As seen in the previous section, to discourage bad solutions, the CSI objective does incorporate a regularization term. However, even with regularization, artifacts in CSI outputs are common. In this paper we aim to fuse the CSI technique with a deep learning approach – our objective is to learn a data-driven mapping, $\mathcal{G}$, from a rough CSI reconstruction to the true permittivity ($\mathcal{G} : \epsilon^{CSI} \rightarrow \epsilon^{true}$). Since the permittivity values are complex, CSI output has a real and an imaginary part; so does the desired permittivity ϵ^{true}. It is worth noting that the real and imaginary parts of the permittivity have very different scales, and a reconstruction loss to find the optimal $\mathcal{G}$ can easily get dominated by one of the components. Several normalization options can be considered; however, to simplify, we decompose the task of estimating $\mathcal{G}$ into two parts, $\mathcal{G}_R$ and $\mathcal{G}_I$. Essentially we learn two separate functions to reconstruct the real and imaginary parts of the permittivity. If the permittivity map is an $M \times N$ image, then each of the learned functions maps $M \times N$ complex domain to $M \times N$ real domain (e.g., $\mathcal{G}_R : \mathbb{C}^{M \times N} \mapsto \mathbb{R}^{M \times N}$). The complex output of CSI can be treated as a 2-channel image. As such, to learn the two functions, the input and output are both images. In particular, we aim to realize $\mathcal{G}_R$ and $\mathcal{G}_I$ through deep neural networks.

2.3.3 Choice of Neural Network Architecture

Traditional convolutional neural networks (CNNs) were originally designed as classifiers – for input they would take in an image, and as output they would produce a decision or an object category. However, recent years have seen several variations in architectures for which the input and output are both images. The requirement for the neural network output to be an image often arises in applications such as image segmentation. For tumor segmentation, the U-Net architecture has shown very promising results [40]. The architecture consists of successive convolutional and downsampling layers, followed by successive deconvolutional and upsampling layers. Moreover, the skip connections between the corresponding contractive and expansive layers keep the gradients from vanishing that helps in the optimization process. To use the architecture for our reconstruction problem, we change the segmentation objective of the U-Net architecture, and replace it with the sum of pixelwise squared reconstruction errors between the true permittivity and the network output.

Note that our training data, which forms the input to the CNN, are complex valued images. Thus, a choice needs to be made on a CNN architecture that can accommodate complex values. Very little has been reported on the training of U-Net with complex weights, although recently there has been some work on training neural networks with complex weights for convolutional architectures [78]. To establish a proof-of-concept, in this paper we make the choice of testing two different U-Net architectures having real-valued weights, described as follows.

Architecture 1: The input to the first network consists of three CSI reconstructions after 250 iterations: we use the real and imaginary parts along with the magnitude of the complex-valued permittivity. The network is trained to output ei-

ther the real or the imaginary part of the corresponding true permittivity map. That is, two independent networks, with three input images and one output image, are trained to reconstruct the real and imaginary parts of the permittivity.

Architecture 2: The input is same as the first architecture but the output consists of all three images corresponding to the magnitude, the real and imaginary parts of the true complex-valued permittivity. Hence, only one network with three inputs and three outputs is trained.

The schematic for the first architecture is shown in Fig. 2.2.

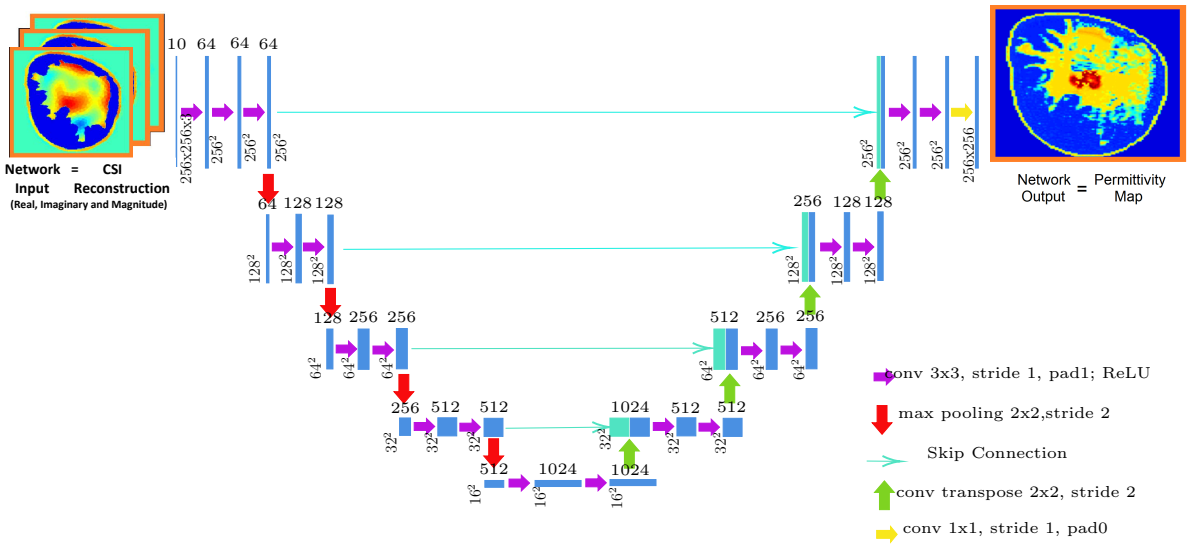

Figure 2.2: Schematic for the U-Net Architecture 1 for the proposed permittivity reconstruction. The input to the network is the CSI reconstruction, and the network is trained to output the corresponding true permittivity map. Two networks with the above architecture were trained to reconstruct the real and imaginary parts of the permittivity.

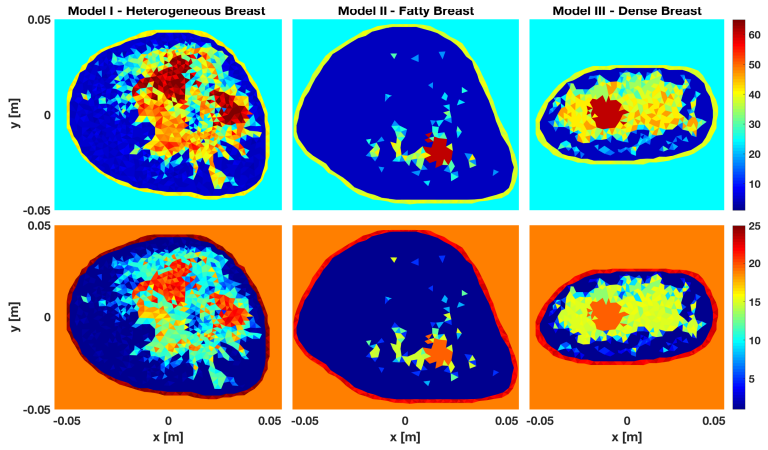

Figure 2.3: Three breast models: I - Heterogeneously dense breast, II - Fatty, III - Very dense breast. Top row - real part, bottom row - imaginary part of permittivity.

2.3.4 Datasets

To create the synthetic scattered-field data for training and testing the CSI-deep-neural-network, MRI-derived numerical breast phantoms are first created by converting each pixel value in tomographic slices of MRI breast images to a corresponding complex-valued permittivity. As base models, three different MRI-derived breast models are utilized as shown in Fig. 2.3. Breast Model I, shown in the left column of Fig. 2.3, is a heterogeneously dense breast of dimensions 10 cm $\times$ 9.5 cm with two tumors of approximate dimensions 1.9 $\times$ 2.3 cm and 1.9 $\times$ 1.8 cm centered at (0.9, 18.4) and (30.14, 2.8). Breast Model II, shown in the middle column, is a 11.2 cm $\times$ 9.6 cm fatty breast that contains one tumor of size 1.5 cm $\times$ 1.6 cm centered at (7.3, 3). Breast Model III is a very dense breast having dimensions of 10 cm $\times$ 5 cm and contains one tumor of size 2.3 cm $\times$ 1.6 cm centered at (4.1, 2.7). All tumors are within the fibroglandular tissue. Ultrasound scattered-field data is generated for each model and is utilized to generate prior information in the form of three tissue regions:

a skin layer, a fat region, and the fibroglandular region (similar to what was done in [77]). This prior is utilized as an inhomogeneous numerical background in each of the CSI-based MWI reconstructions that constitute the datasets for training and testing the deep neural network. The forward data is obtained using a finite-element 2D electromagnetic field solver and 5% noise is added to the forward data before it is inverted using the FEM-CSI technique. Details can be found in [68].

In order to generate a sufficient number of examples having various tumors to train the neural networks considered herein, the permittivity values at the pixels where the tumors exist in the three breast models are first set to that of fibroglandular tissue. Then, for each breast model, 400 phantoms are generated with either a single or two tumors occupying the fibroglandular region. In particular 200 phantoms have one tumor and the other 200 are generated with two tumors. The generated tumors have an approximate maximum diameter of 1.1 - 1.5 cm and are randomly located within the fibroglandular region (contiguous pixels are randomly grown from a starting point until a maximum diameter is reached). Examples of numerical phantoms for each breast model are shown in the right column of Fig. 2.4. A total of 400 phantoms were generated for each of the three models, so our dataset consists of 1200 breast phantoms with 600 examples each for single and two tumors. Microwave as well as ultrasound scattered-field data was generated for each of the 1200 phantoms and multimodal CSI reconstructions were performed.

2.4 Numerical Experiments

All the CNNs were implemented in Python 3.6 using the Keras library running Tensorflow as backend. We used a Tesla P100-PCIE-12GB graphic processor and Intel(R) CPU(3.50 GHz). The convolutional layer weights were initialized by Gaussian

random distribution using Xavier's method to obtain an appropriate scale [79]. We used a batch size of 10 and ran training for 75 epochs.

2.4.1 U-Net Training and Quantitative Assessment

Four-fold cross-validation strategy has been utilized to evaluate the proposed deep neural network for all experiments. Two types of training settings were performed differentiated by the breast models used for training. U-net A is trained using only the real part of CSI reconstruction for five different frequencies whereas U-Net B is trained using the real and imaginary part for five different frequencies. For both U-nets training was done using 600 images of the dataset were divided into 4 groups consisting of 150 images (75 from each breast model). To implement the four-fold cross-validation, four networks were trained, each using three groups for training (450 images) and tested using the remaining hold-out group (150 images). Thus all 600 cases featured as test examples when they were not part of the training set. Quantitatively assessment has been done to evaluate the reconstruction performance and the tumor segmentation capability of the trained U-Nets. Root Mean Squared (RMS) reconstruction error between the network output and the true permittivity values has been performed to evaluate the reconstruction quality. The Area Under the Curve (AUC) of the pixel-wise Receiver Operating Characteristics (ROC) using the reconstructed permittivity as a feature has been used to quantify the tumor segmentation performance. For comparison we also computed RMS reconstruction error and performed ROC analysis on CSI-only reconstructions. The results of this quantitative evaluation are shown in Table 1 and Table 2.

Two types of training settings were performed differentiated by the breast models used for training. U-Net A was trained using images from all three types of breast

models whereas U-Nets B, C, and D were trained using images from only two types of breast models. Details of the testing that was performed is as follows:

Training Setting: U-Net A: In this setting, training was done using examples from all three breast models. The 1200 images of the dataset were divided into 4 groups consisting of 300 images (100 from each breast model). To implement the four-fold cross-validation, four networks were trained, each using three groups for training (900 images) and tested using the remaining hold-out group (300 images). Thus all 1200 cases featured as test examples when they were not part of the training set.

Training Setting: U-Net B, U-Net C and U-Net D: In this setting, three different U-Nets where breast examples from one type of breast model was excluded from the training set were trained. In U-Net B examples from breast Model III were excluded, in U-Net C examples from breast Model II were excluded, and in U-Net D examples from breast Model I were excluded from the training set. The training images were taken from the same groupings of the four-fold cross-validation used for U-Net A but now only 600 images from three of the groups were used for training. Testing was performed using images from the hold-out group. In addition testing was performed using all combinations of breast model from the hold-out group. That is, utilizing from either breast Model I, II, III, I & II, I & III, or II & III. The first three combinations consist of only 100 images while the latter three consist of 200 images from the hold-out group. This type of testing was motivated by the fact that each model is significantly different from the rest of the models; excluding them from the training set taxes the neural network when during testing it is presented with reconstructions from the unseen model.

Performance Metrics: We quantitatively assess both the reconstruction capability and the tumor segmentation performance of the trained U-Nets. To assess the recon-

struction quality, we use the root mean squared (RMS) reconstruction error between the network output and the true permittivity values (for both the real and imaginary parts separately). To quantify the tumor segmentation performance, we use the area under the curve (AUC) of the pixel-wise receiver operating characteristics (ROC) using the reconstructed permittivity as a feature. Pixel-wise ROC-AUC is a good performance measure for tumor segmentation since it quantifies the separation between the distribution of permittivities of tumor and non-tumor pixels [80]. For comparison we computed RMS reconstruction error and performed ROC analysis on CSI-only reconstructions. The results of this quantitative evaluation are shown in Tables 2.1 and 2.2.

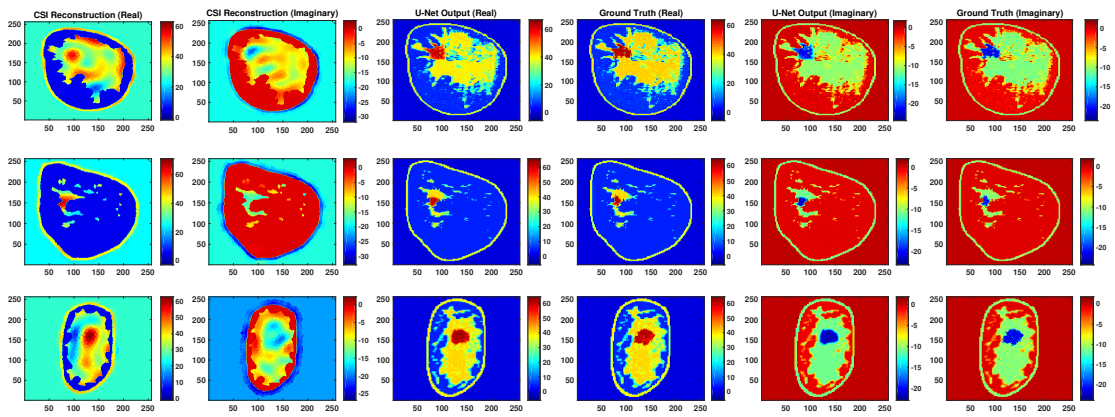

Figure 2.4: Representative reconstructions from each breast model for U-Net A setup (Architecture 1: Training set: Breast Models I, II, III; Testing set: Breast Models: I, II, III)

2.4.2 Qualitative Evaluation of Robustness

To evaluate the robustness of the proposed methodology for creating the CNNs we check the sensitivity to the parameters of the training dataset. Specifically, the pa-

rameters that were used in generating the CSI images as well as the parameters used in presenting the images to the CNN. First, given that all CNNs were trained utilizing CSI images that were terminated after 250 iterations, the performance of the best performing trained network (U-Net A) is checked by testing with CSI reconstructions that were terminated after 20, 150 and 500 iterations. Comparative examples of output from U-Net A for these CSI images at these iteration numbers are shown in Figs. 2.5 and 2.6. This shows the performance of the CNN when tested against images that could vary substantially in terms of accuracy from the ones with which it was trained; a type of test against the proximity of the input to the test set.

An additional test regarding the required proximity of the input to the test set is to test the robustness of the network against geometric transformations of the input images such as rotation and flipping. Note that U-Net A was trained using only unrotated and unflipped images. Fig. 2.7 demonstrates the result of the trained network when the input images were rotated and flipped.

2.5 Results and Discussion

Tables 2.1 and 2.2 show the RMS reconstruction errors (cyan cells) and ROC-AUC (gray cells) for the different training and testing setups previously described. Fig. 2.8 shows ROCs when the test sets included breast models I, II, III (plot (a) and (c)) and only Model II (plot (b) and (d)).

From these results we find that U-Net A, which was trained on examples from all breast models, performs better (lower reconstruction error and higher AUC) than the both CSI and other U-Nets: B,C,D. This is expected because the three breast models vary considerably in their internal structure. Although the sub-optimal networks in all cases improve the RMS error over that obtained using CSI, the AUC is sometimes

improved but actually deteriorates for some of these networks.

It is expected that the CNN will perform worse when a whole class of breast models is not seen by the neural network during the training. From the results it can be observed that deterioration in the AUC is most pronounced in U-Net B (trained using Models I and II) and U-Net D (trained using Models II and III), when they are tested using the missing model. The same does not happen with U-Net C (trained using Models I and III). Its performance does not deteriorate substantially compared to U-Net A. It is too early to conclude from this observation that a U-Net trained on heterogeneously dense or very dense breast models can generalize to improve the CSI reconstructions of fatty breasts. It is possible that a thresholding technique might not be an effective test for detecting tumors which make up a large part of the fibroglandular tissue (as is the case for Model II breasts). This is because CSI on its own already detects the small amount of fibroglandular tissue in Model II breasts very well with few errors in the fatty tissue, thus, thresholding the image always detects a part of the fibroglandular tissue as tumor, and this has a good probability of being truly tumor (high true-positive rates). What this implies is that the thresholded ROC-AUC metric is not able to accurately report on the improvements U-Net is able to impart on the CSI reconstructions.

It is notable, however, that U-Net C is able to generalize and not corrupt Model II breasts (having never seen that type of breast). This is a surprising result and leads us to believe that a U-Net trained on a wider variety of breast models will be quite robust in providing improvements of CSI reconstructions.

In terms of robustness and generalization, although testing the networks on rotated and flipped images caused a drop in performance, the U-Net output remains much better than CSI. For qualitative visualization of results, representative exam-

ples of reconstruction are shown in Figs. 2.7. This is also true when testing with CSI reconstructions that were stopped at different iterations, as can be seen in Figs. 2.5 and 2.6.

The other observation relates to the differences between Architectures 1 and 2. Using Architecture 2, there seems to be a slight improvement in the AUC over Architecture 1 when the ROC is obtained using the imaginary part of the complex permittivity. On the other hand the RMS error slightly deteriorates, which is not surprising because Architecture 2 only has both the real and imaginary parts as an output and therefore both affect the cost-function. Given that the magnitude of the real part is greater than that of the imaginary part, the real part dominates the cost-function. It is surprising, though, that the AUC improves when Architecture 2 is used. This leaves the differences between Architectures 1 and 2 inconclusive. More research is required to differentiate the differences between these two Architectures. In addition, future work will explore the potential use of architectures utilizing complex weights (see for example [78]).

2.6 Conclusion

A deep learning technique using a CNN that takes in tomographic reconstructions representing the complex-valued permittivity of the breast obtained using the CSI algorithm and produces images that are much closer to the true permittivity has been introduced. The CNN reconstructed images show the network's ability to remove artifacts that are typical of CSI reconstructions. Not only is the RMS error between the CNN reconstructed images and the true permittivity images improved over the CSI reconstructions, but by using a simple thresholding detection algorithm tumors that are not detectable in CSI reconstructions are correctly detected in the CNN

Table 2.1: Comparison of reconstruction and tumor detection performance for architecture 1. The entries in the cells show the reconstruction RMS error (Cyan) and ROC-AUC (Gray) for the respective setting. The first part of table shows performance when the real part of the reconstructed permittivity was used to compute the reconstruction error and to generate ROC curve and the second part shows performance for Imaginary part

Models included in the Training Set	Reconstruction Technique	Breast models included in the Test Set						
		I, II, III	I	II	III	I, II	I, III	II, III
N/A	CSI	2.199	2.214	1.931	2.423	2.077	2.321	2.191
		0.897	0.868	0.892	0.897	0.890	0.882	0.915
I, II, III	U-Net A	0.122	0.144	0.075	0.135	0.114	0.140	0.110
		0.987	0.980	0.994	0.984	0.987	0.982	0.991
I, II	U-Net B	1.329	0.257	1.158	1.973	0.839	1.407	1.618
		0.596	0.908	0.653	0.442	0.871	0.593	0.387
I, III	U-Net C	0.694	0.253	1.151	0.232	0.834	0.243	0.830
		0.922	0.886	0.937	0.919	0.917	0.903	0.942
II, III	U-Net D	1.297	1.947	1.098	0.231	1.580	1.386	0.794
		0.758	0.587	0.730	0.929	0.631	0.740	0.904
N/A	CSI	7.103	6.894	6.548	7.806	6.723	7.364	7.205
		0.757	0.717	0.799	0.713	0.762	0.721	0.781
I, II, III	U-Net A	0.307	0.352	0.205	0.342	0.288	0.347	0.282
		0.987	0.981	0.992	0.985	0.987	0.983	0.990
I, II	U-Net B	1.884	0.594	1.572	2.797	1.188	2.022	2.268
		0.654	0.889	0.907	0.529	0.906	0.649	0.465
I, III	U-Net C	1.034	0.547	1.609	0.561	1.202	0.554	1.205
		0.913	0.888	0.937	0.895	0.912	0.894	0.929
II, III	U-Net D	1.843	2.754	1.512	0.567	2.221	1.989	1.142
		0.694	0.501	0.810	0.916	0.536	0.671	0.909

Table 2.2: Comparison of reconstruction and tumor detection performance for architecture 2. The results show performance when the real and imaginary part of the reconstructed permittivity was used to compute the reconstruction error and to generate ROC curve.

Models included in the Training Set	Reconstruction Technique	Breast models included in the Test Set						
		I, II, III	I	II	III	I, II	I, III	II, III
N/A	CSI	2.199	2.214	1.931	2.423	2.077	2.321	2.191
		0.897	0.868	0.892	0.897	0.890	0.882	0.915
I, II, III	U-Net A	0.126	0.149	0.078	0.140	0.119	0.145	0.114
		0.988	0.982	0.993	0.985	0.988	0.983	0.991
I, II	U-Net B	1.310	0.268	1.087	1.973	0.792	1.408	1.593
		0.623	0.892	0.944	0.515	0.912	0.612	0.434
I, III	U-Net C	0.678	0.241	1.125	0.236	0.813	0.238	0.813
		0.921	0.894	0.949	0.917	0.917	0.905	0.938
II, III	U-Net D	1.285	1.941	1.061	0.242	1.565	1.383	0.770
		0.753	0.581	0.841	0.924	0.620	0.734	0.918
N/A	CSI	7.103	6.894	6.548	7.806	6.723	7.364	7.205
		0.757	0.717	0.799	0.713	0.762	0.721	0.781
I, II, III	U-Net A	0.313	0.361	0.206	0.349	0.294	0.355	0.286
		0.989	0.985	0.992	0.987	0.989	0.987	0.991
I, II	U-Net B	1.899	0.599	1.607	2.807	1.213	2.030	2.287
		0.670	0.896	0.938	0.516	0.913	0.643	0.516
I, III	U-Net C	1.044	0.561	1.630	0.546	1.219	0.553	1.215
		0.918	0.889	0.943	0.910	0.914	0.901	0.935
II, III	U-Net D	1.851	2.751	1.547	0.558	2.232	1.985	1.163
		0.728	0.566	0.819	0.951	0.600	0.703	0.920

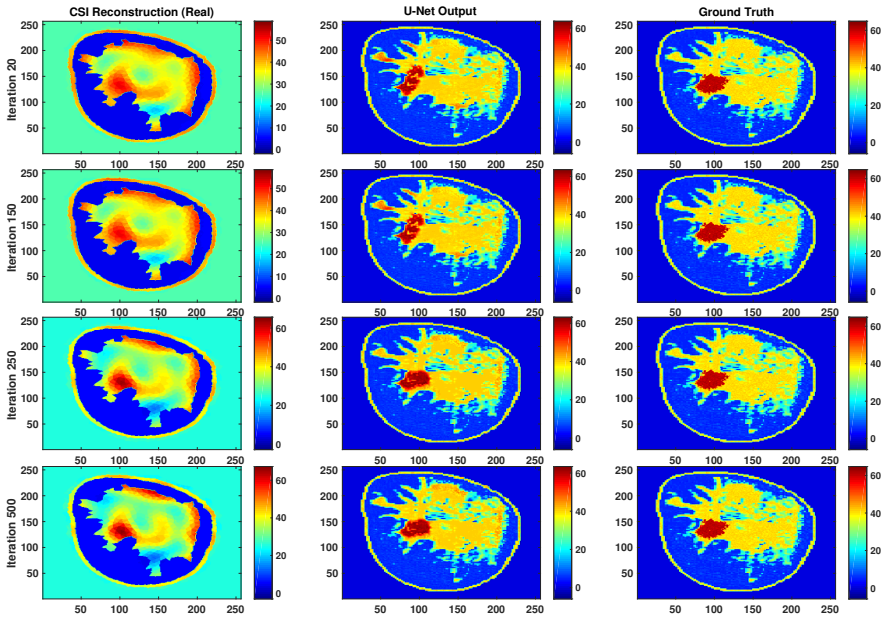

Figure 2.5: Representative reconstructions of the real part for a particular example when the test images were stopped at iteration number 20, 150 and 500 but the neural net was trained on iteration number 250.

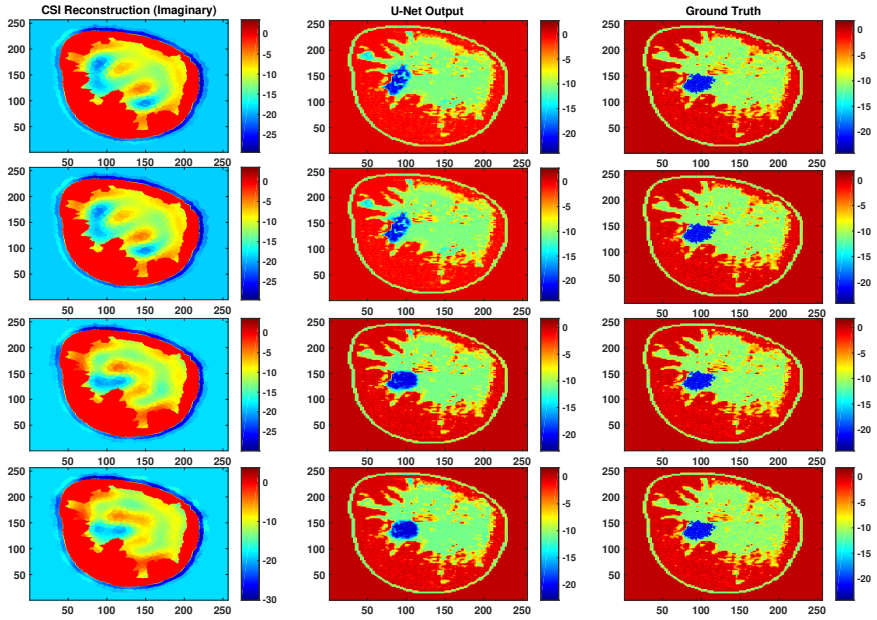

Figure 2.6: Representative reconstructions of the imaginary part for a particular example when the test images were stopped at iteration number 20, 150 and 500 but the neural net was trained on iteration number 250.

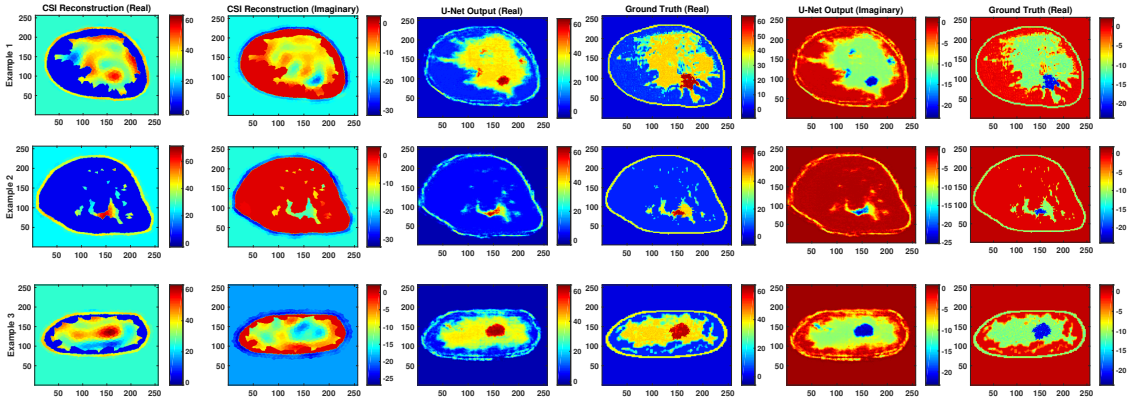

Figure 2.7: Representative reconstructions from each breast model when the test images were rotated and flipped but the neural net was trained on unrotated and unflipped images.

output. To assess the network's generalization we have conducted experiments by testing on examples that differ from the training examples in varying degrees in terms of breast models and geometric transformations. Though our dataset consisted of numerically generated phantoms, we used numerical breast models derived from MRI tomographic images to generate the multimodal MW/US reconstructions. Three types of breast phantoms that span the array of BI-RADS Breast Densities were used for this study. It was found that training with all three breast-types produced the most robust CNN: consistently improving the AUC and RMS error metrics over the CSI results. It was found that when certain breast model-types were missing from the training set, sometimes the AUC actualy degrades whereas the RMS is still improved. Thus, a significant finding of this work is that a wide diversity of breast-types should be used in the training of CNNs for this purpose.

The first step in extending this work is to train 3D-CNNs that take full-3D CSI images as input. The excellent results also motivate future work that will involve the use of experimental scattered-field data derived from real breast multimodal

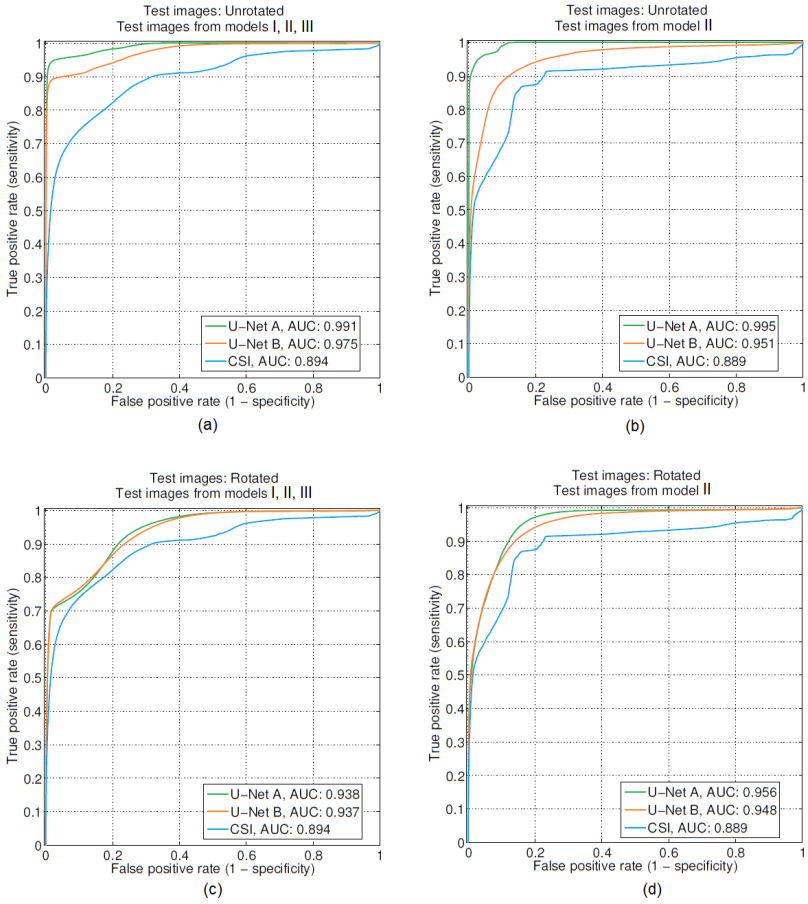

Figure 2.8: Comparison between the detection performance based on the reconstructed outputs of U-Net and CSI. For all the above cases U-Net A and U-Net B represent the settings when the network was trained on examples from models I, II, III and models I, III respectively. Training was always done on unrotated images. Testing scenarios (whether the images were rotated or not) as well as what models were included in testing are shown on top of each plot.

MW/US imaging. Preliminary tumor-detection results using experimental phanotms in a unique experimental breast imaging system have recently been reported [28]. Future work will test the ability of CNNs trained with 3D images to improve the CSI results obtained from that system.

3

Paper2: Full 3D Microwave Breast Imaging Using a Deep-Learning Technique

---

3.1 Abstract

A deep learning technique to enhance the 3D images of the complex-valued permittivity of the breast obtained via microwave imaging is investigated. The developed technique is an extension of one created to enhance 2D images. We employ a 3D Convolutional Neural Network, based on the U-Net architecture, that takes in 3D images obtained using the Contrast-Source Inversion (CSI) method and attempts to produce the true 3D image of the permittivity. The training set consists of 3D CSI images, along with the true numerical phantom images from which the microwave scattered field utilized to create the CSI reconstructions was synthetically generated. Each numerical phantom varies with respect to the size, number, and location of tumors within the fibroglandular region. The reconstructed permittivity images produced by the proposed 3D U-Net show that the network is not only able to remove the artifacts that are typical of CSI reconstructions, but it also enhances the detectability of the tumors. We test the trained U-Net with 3D images obtained from experimentally collected microwave data as well as with images obtained synthetically. Significantly, the results illustrate that although the network was trained using only images obtained

from synthetic data, it performed well with images obtained from both synthetic and experimental data. Quantitative evaluations are reported using ROC curves for the tumor detectability and RMS error for the enhancement of the reconstructions.

3.2 Introduction

Microwave Imaging (MWI) techniques that have been applied to the detection of breast cancer come in two forms: Radar-based techniques that attempt to detect tumors within the breast's interior [66], and inverse-scattering based methods that attempt to reconstruct complex permittivity maps corresponding to the distribution of the different breast tissues [65]. The quantitative techniques, which are of interest herein, rely on the fact that different breast tissues (e.g., skin, adipose, fibroglandular and cancerous tumors) have different dielectric properties in the microwave frequency band [8, 9].

Successfully implementing the inverse-scattering approach requires that one has a good numerical electromagnetic field model for the MWI system being used to acquire scattered-field data, including the antennas and the breast, but more importantly, requires that one solves a non-linear ill-posed inverse scattering problem. This is usually accomplished using computationally expensive iterative methods where the inversion model consists of a numerical solution of an electromagnetic forward scattering problem [62]. One challenge in using MWI for breast imaging is that the breast is a high-contrast object-of-interest (OI) having complicated internal structures and this produces unique artifacts in the quantitative reconstructions of the complex-valued permittivity of the breast tissue. Both the non-linearity and the ill-posedness of the inverse scattering problem become more difficult to deal with for high contrast OIs having such complicated internal structure because they lead to multiple reflections

within the OI.

The MWI technique we use in the work reported herein is the Contrast Source Inversion (CSI) method [24,76,81]. Although this is a state-of-the-art MWI technique it still succumbs to artifacts even when prior information is utilized to try to alleviate the non-linearity and ill-posedness of the problem [19,30]. Note that all MWI techniques, qualitative and quantitative alike, currently have difficulties with imaging artifacts [22,62,65,66].

Recently there has been intense interest in the use of deep learning techniques in a broad range of applications such as natural language processing, computer vision and speech recognition [33]. In medical imaging, utilizing deep learning techniques for segmentation [40,41], as well as detection and classification [42–44] has been well investigated, at least for the more common modalities. Studies have shown that there is significant potential in applying deep learning techniques for the purpose of removing artifacts from biomedical images generated using some common modalities. Kang et al. proposed a deep CNN using directional wavelets for low dose x-ray computed tomography (CT), and results illustrate that a deep CNN using directional wavelets was more efficient in removing low dose related CT noise [82]. Han et al. [83] and Jin et al. [72] independently proposed multi-scale residual learning networks using U-Net to remove these global streaking artifacts, In addition, domain adaptation from CT to MRI has been successfully demonstrated [84].

MWI researchers are also trying to use machine learning techniques to improve the performance of microwave imaging. For instance, researchers combined a neural network with microwave imaging to learn the forward model for a complex data-acquisition system [73]. Rekanos et al. proposed radial basis function neural network to estimate the position and size of proliferated marrow inside bone tissue with mi-

crowave imaging [74]. Le et al. tried to take benefit of a deep neural network to enhance the constructed images [56]. Their deep neural network was trained to take microwave images created using the back-projection (BP) method as an input and have the network output a much-improved image. In fact, they tried to by-pass the use of iterative techniques for solving the full nonlinear electromagnetic inverse problem. Most recently, we have investigated utilizing deep learning techniques to improve 2D microwave imaging for the breast imaging application [85]. Researchers employing Radar-based techniques have also been investigating machine learning approaches for the detection of breast lesions [86].

In this paper, we utilize a deep learning technique, based on Convolution Neural Networks (CNNs), to enhance full 3D MWI reconstructions obtained using a 3D CSI algorithm that uses the Finite Element Method (FEM) to solve the electromagnetic forward problem [28] . The enhancement removes reconstruction artifacts and improves the accuracy of the resulting images. We utilize a 3D 10-channel U-Net architecture for the CNN where the input and output are both 3D images, and each channel corresponds to the real and imaginary parts of the complex-valued permittivity images created using five different microwave frequencies.

In Section 4.3 we start by providing a brief description of the CSI-based methodology that we use, as well as the numerical phantoms and MWI parameters utilized to generate training images. We also provide details of our chosen deep learning approach. In Section 4.4 we describe the training data set as well as the parameters used for the network training. In continue, quantitative assessment and assessment of robustness for numerical experiments are described. Section 3.5 provides a brief description of our experimental setup and also the result of trained CNN for the experimental data. Finally, in section 4.6 we give our conclusion and explain our future

work.

3.3 3D CSI-Deep-Learning Methodology

In microwave data acquisition processes, electromagnetic fields scatter from, and propagate through the tissue in a three Dimensional (3D) space. However, to accelerate the image reconstruction process and reduce the computational complexity, researchers are trying to represent electromagnetic waves in 3D space as a simplified 2D model. However, studies have shown that simplifying 3D problems to 2D models can increase the level of artifacts in the recovered dielectric properties [49]. Moreover, in 2D imaging when the object of interest is small, there is a chance that it place between two consecutive imaging slice, then the reconstruction algorithm would not discover the target precisely. Hence, utilizing a viable 3D microwave image reconstruction will enhance the accuracy and quality of reconstruction [23]. While iterative methods have improved dramatically over the years, providing improved resolution and accuracy of the reconstructed properties, as well as more efficient implementations, there are still many fundamental trade-offs between these three aspects due to operational, financial, and physical constraints. Lower resolution in comparison with other modalities as well as the many reconstruction artifacts that are related to the nonlinearity and ill-posedness of the associated inverse problem, are the main reasons that MWI is not clinically accepted yet. Although it has been shown that using accurate prior information will reduce the Root-Mean-Squared (RMS) reconstruction error over the whole image [19, 30, 31, 69, 87], artifacts and reconstruction errors near the tumor can translate to poor tumor detection results [32].

3.3.1 Microwave Imaging via Contrast Source Inversion

The first part of the proposed 3D CSI-Deep-Learning methodology consists of quantitatively generating the complex-valued permittivity images using a MWI technique. Quantitative MWI requires that one solve a non-linear ill-posed inverse scattering problem. A plethora of algorithms have been developed during the past 40 years to solve this problem. They generally involve computationally expensive iterative methods to locally minimize a specially designed functional that incorporates a numerical inversion model approximating the relevant electromagnetic phenomena of the problem [22, 62]. In the past different MWI techniques have utilized tailored optimization algorithms with various functionals. Some of the most prominent techniques have been the Distorted Born Iterative Method [88], Gauss-Newton Inversion [25], the Levenberg-Marquardt method [89] and the Contrast Source Inversion technique [24]. Innovations on these foundational algorithms have allowed improvements to the obtainable imaging accuracy and resolution, especially in the area of breast imaging, *e.g.*, [90, 91]. Being an ill-posed problem, regularization techniques are required to solve the inverse scattering problem [26, 92].

As previously mentioned, to solve the electromagnetic inverse scattering problem associated with microwave breast imaging we employ the CSI method. The numerical inversion model utilized within the CSI algorithm is based on a full-vectorial 3D electromagnetic model of the MWI system that includes a quasi-resonant flat-faceted chamber [93, 94]. The 3D FEM-CSI algorithm is utilized with prior information in the form of an inhomogeneous background as was done in [28]. Breast images reconstructed from both synthetic and experimental scattered-field data are utilized in this work. The experimental data is collected using the same air-based quasi-

resonant imaging chamber described in [28]. Thus, the forward model for creating the synthetic data and the inversion model, both utilize a 3D finite element model of the same imaging chamber.

We consider both synthetic and actual experimental breast phantoms with three tissue types: fat, fibroglandular and tumor.. These breast phantoms are formed using a simple outer fat layer, and an interior fibroglandular region that contains one or more embedded tumors. The breast phantoms are positioned within the chamber as depicted in Fig. 3.1.

The phantoms are interrogated using microwave energy with magnetic-field probes located on the conductive chamber walls. The same probes are used as receivers. As described in [94], the 24 transmitters and receivers are ϕ-polarized. Data is collected at single frequencies and for every transmitter, 23 magnetic fields are recorded at the receiver locations. Thus, 552 complex numbers (magnitude and phase) are utilized to reconstruct the breast phantom that is located within the chamber. That is, the real and imaginary parts of the complex permittivity of the breast phantom are reconstructed using the CSI algorithm.

The forward data is obtained using a 3D-FEM electromagnetic field solver. Before inverting the data using the FEM-CSI algorithm, we add 5 % noise as is usual in creating synthetic data [76]. This procedure is performed at individual frequencies and for the work considered herein the frequency band of 1.1 GHz to 1.5 GHz is used. It has been shown that reconstruction artifacts appear at different locations of the imaging domain when different frequencies are used, whereas the tumor is typically reconstructed at approximately the same location [28]. In that work, it was shown that this feature can improve the tumor detection by using the intersection of thresholded images.

For the synthetically generated data and inversions, the permittivity is assumed to be constant over frequency. The complex permittivity values that are used are given in Table 3.1. For the experimental test case considered herein, the permittivities of the utilised tissue-mimicing liquids do vary with frequency (see [28] for details).

Table 3.1: Complex permittivity for different tissues

Permittivity			
Air	Fat	Fibroglandular	Tumor
1-0.001j	3-0.6j	20-21.6j	56.3-30j

It has been shown that successful CSI reconstructions can be obtained if one introduces a fat and fibroglandular region as prior information in the CSI algorithm. This prior information is in the form of an inhomogeneous numerical background against which the contrast is defined. That is, if $\epsilon_n(r)$ and $\epsilon(r)$ represent the background information and the desired complex permittivity, as functions of position, then the contrast $\chi(r) = (\epsilon(r) - \epsilon_n(r))/\epsilon_n(r)$ is one of the variables solved for in the CSI algorithm (the other variable being the contrast sources generated for each transmitter). Full details of the CSI algorithm, used in this way, are provided in [19, 30].

Introducing an inhomogeneous background in this way is a form of regularizing the inverse problem, but as was already mentioned, various reconstruction artifacts are still present in the CSI-reconstructed images. These artifacts increase the false-positive and reduce the true-positive tumor detection rates. For the case of 2D imaging, it was recently shown that using a deep-learning technique ameliorates this problem [85]. This has motivated the interest in using a similar deep-learning technique to improve 3D MWI. However, in addition to artifacts, 3D MWI also suffers from the problem of producing reconstructions that do no not reach the maximum permittivity values of the true phantom model. This was noted in [28] and therefore the detection threshold was based on a 85 percentage of the maximum reconstructed

value. Fortunately, the tumor permittivity values are at the extreme end of the scale, so such a procedure is successful. Improving the CSI reconstructions by correcting the reconstructed permittivity values, in addition to removing artifacts is the sought after goal of using a deep learning technique.

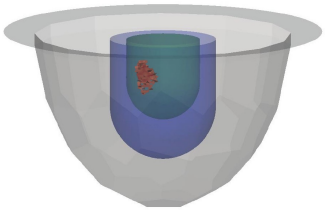

Figure 3.1: Simulated Breast Model. Gray, blue, green, and red regions represent air, fat, fibroglandular, and tumor, respectively.

3.3.2 Machine Learning Approach to Reconstruction

Combining the CSI technique with a deep learning approach is accomplished by learning a data-driven mapping, $\mathcal{G}$, from a CSI reconstruction to the true permittivity ($\mathcal{G} : \epsilon^{CSI} \rightarrow \epsilon^{true}$).

In this study, we learn a mapping from the real and imaginary parts of the permittivities in CSI reconstructions at several frequencies to a single real permittivity image. Thus, if the CSI complex permittivity map is an $L \times M \times N$ 3D image, and reconstructions at five frequencies are utilized, then each of the learned functions maps $5 \times L \times M \times N$ complex domain to $L \times M \times N$ real domain (e.g., $\mathcal{G}_R : \mathbb{C}^{5\times L\times M\times N} \mapsto \mathbb{R}^{L\times M\times N}$). The complex output of CSI at the five selected frequencies can be treated as a 10-channel image. We realized this mapping through a deep neural network as follows.

The desired mapping for our task at hand is an image-to-image transformation;

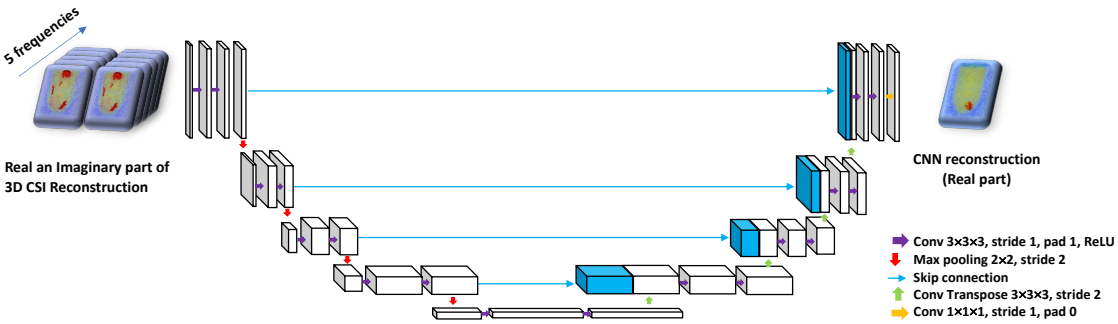

Figure 3.2: Schematic for the proposed U-Net to reconstruct the real part of permittivity. The input to the network is the 3D CSI reconstruction, and the network is trained to output the corresponding true 3D permittivity map.

there are multiple neural architectures that can implement this mapping. For instance, a naive choice could be a fully-connected single layer neural network which takes in CSI reconstruction as input and is trained to output the ground truth permittivity. However, such an architecture would be very prone to overfitting [33]. We therefore use a hierarchical convolutional neural network for our image-to-image transformation task. A good template for such a task is the U-Net architecture which is one of the most successful deep neural networks for image segmentation and reconstruction problems [37]. The architecture consists of successive convolutional and downsampling layers, followed by successive deconvolutional and upsampling layers. Moreover, the skip connections between the corresponding contractive and expansive layers keep the gradients from vanishing that helps in the optimization process [35,37]. To use a U-Net for reconstruction, the original objective of the U-Net is replaced with the sum of pixelwise squared reconstruction errors between the true real part of permittivity and the output of U-Net [37]. In our problem, the network input is the 3D CSI reconstructed complex images (after 500 iterations). Thus, there are two options for choosing the U-Net architecture, U-Net with complex weights and U-Net with

real weights. Very few studies have been done on the training of U-Net with complex weights, although very recently Trabelsi et al. tried to train the neural network with complex weights for convolutional architectures [78]. In this paper, we decided to use a U-Net architecture having real-valued weights. A schematic representation of our architecture is shown in Fig. 3.2. The motivation for choosing the neural network parameters (the number of convolutional layers, size and number of filters) is as follows. In a hierarchical multi-scale CNN, the effective receptive field of the convolution filters is variable at each layer, i.e. through successive sub-sampling it is possible to have larger receptive field even by using filters of smaller kernel size [95, 96]. As mentioned above, the input to our neural network is $L \times M \times N \times 10$; in particular, for each frequency, the dimension of our input image volume is $64 \times 64 \times 64$ (i.e. $L = M = N = 64$). If we start with a 3D receptive field of $3 \times 3 \times 3$, after four layers of successive convolutions and subsampling (by a factor of $1/2$), the receptive field would effectively span the entire image volume. We therefore use four convolutional layers with a 3D filter kernel size of $3 \times 3 \times 3$. Since after each convolutional layer the size of the image volume is reduced, we can increase the number of filters at each successive layer to enhance the representational power of the neural network [96]. In particular, we start with 32 filters for the first layer and successively double the number of filters after each layer (number of filters after the fourth layer is 512). This defines the encoder part of the U-net i.e. the part of neural network consisting of contractive convolutions. For the decoder part, we follow a symmetric architecture consisting of expansive convolutions [37].

3.4 Numerical Experiments

3.4.1 Datasets

While we tested our neural network on both experimental and synthetic data, for training we only used a synthetically generated dataset. The training dataset consisted of 600 numerical breast phantoms; tumors were randomly generated within the fibroglandular region of the phantom. Starting from a random initial position, tumor pixels were grown randomly till the maximum diameter reached a threshold. To have variability in the dataset, the threshold for the maximum diameter was also randomly sampled from the range: 1.1-1.5 cm. One half the dataset consisted of breast phantoms with one tumor, while the other half had phantoms with two tumors. We then employed a forward solver [76] to generate the scattered field data corresponding to the phantoms. CSI reconstructions were performed at five frequencies: 1.1, 1.2, 1.3, 1.4, and 1.5 GHz. These CSI reconstructions together with the corresponding ground-truth permittivity values for the phantoms formed our training data for the U-Net input and output respectively.

3.4.2 Network Training

All the CNNs were implemented using Python 3.6 and Keras 2.0.6 with Tensorflow backend. We used a Windows 10 computer with a Tesla P100-PCIE-12GB graphic processor and Intel(R) CPU(3.50 GHz). We used the popular Xavier initialization for the convolutional layer weights to obtain an appropriate scale [79]. We trained with a batch size of 10, for 200 epochs with Adam optimization. Four-fold cross-

validation strategy has been utilized to evaluate the proposed deep neural network for all experiments. The U-net is trained using the real and imaginary parts for five different frequencies as inputs. With 600 phantoms in our dataset, each fold in four-fold cross-validation consisted of 150 examples. For every fold, training was done using 450 cases, while the testing set consisted of the held-out 150 examples. Thus all 600 cases featured as test examples when they were not part of the training set. For the loss function, we use pixel wise mean squared error between the ground truth 3D image and the CNN 3D reconstructed image as follows:

$$RMSError = \frac{1}{LMN} \sum_{x=1}^{L} \sum_{y=1}^{M} \sum_{z=1}^{N} (I_{x,y,z}^{GT} - I_{x,y,z}^{CNN})^2 \tag{3.1}$$

where $I_{x,y,z}^{CNN}$ represents a 3D image reconstructed by the CNN and $I_{x,y,z}^{GT}$ represents a 3D ground truth image.

3.4.3 Quantitative Assessment

The CNN-enhanced reconstruction performance and the subsequent tumor segmentation based on thresholding was evaluated quantitatively. The Root Mean Squared (RMS) reconstruction error between the network output and the true permittivity values was used to evaluate the reconstruction quality. The performance of a detection algorithm is often assessed in terms of two types of error i.e. False Positive Rate (FPR) and False Negative Rate (FNR). FPR and FNR will vary depending on the decision threshold used on the output score of the detection algorithm. To quantify the ability of the output score to separate the two classes, we need to analyze the two errors for all possible thresholds. In particular, we performed Receiver Operating Characteristics (ROC) analysis to assess the ability of the reconstructed

complex permittivity to distinguish between tumor and non-tumor pixels. The ROC curve is a plot of True Positive Rate ($TPR = \frac{TP}{TP+FN}$) against the False Positive Rate ($FPR = \frac{FP}{FP+TN}$) for all thresholds. The Area Under the Curve (AUC) for the ROC is a metric quantifying the separability between tumor and non-tumor pixels [97]. For comparison we also computed RMS reconstruction error and performed ROC analysis on CSI-only reconstructions. ROC carries information about the relation of the true positives vs. the false positives. However, the information about the distributions of thresholds at which the different ratios fall would be lost in this curve. Therefore, the distance from any location on the ROC curve to the top-left corner of the plot is also an informative metric (we call this the "distance-to-maxTD" or "DMTD"plot). We use the DMTD curve as a complementary metric to display/analyze the relation between the true positive detection as well as the threshold at which a certain true positive to negative ratio happens. This will especially help us better understand the performance of the overlapping (or very similar) ROC curves for different scenarios. The depth of the curve tells us about the quality of the reconstruction; the lower the dip, the better the performance of the algorithm. The location of the dip carries information about the separation of the tumor relative to the background; for instance, the further the dip of the DMTD curve is to the left, the higher the separation between the background and tumor. Additionally, the width of the dip gives us information about the robustness of the algorithm; the wider the dip of the curve, the higher the chances of having a tumor with no artifacts (false positives) for the proper reconstruction of the tumor size and shape. The results of this quantitative evaluation by using four fold cross-validation strategy for all 600 images are shown in Fig. 4.5 and Table 3.2.

Fig. 3.4 illustrates the performance of the trained U-Net in comparison with

Table 3.2: Comparison of reconstruction and tumor detection performance

	RMS error		AUC	
	CSI	CNN	CSI	CNN
Synthetic Data	1.4356	1.161	0.935	0.957
Exprimental Data	1.250	1.172	0.794	0.938

CSI reconstruction for an arbitrary example with two tumors. Based on the AUC and RMS error metrics, it could be concluded that the proposed CNN is successful in term of reconstruction and tumor detection. However, in a previous study [28], it was shown that taking the intersection of multi-frequency thresholded 3D images performs the best at detecting tumors. Therefore, we compared our trained CNN with the intersection of multi-frequency thresholded 3D images in terms of detection. The superiority of the trained CNN to CSI results as well as to multi-frequency thresholded results are shown in Fig. 4.5. For this same example, the CSI reconstructions at the remaining four other frequencies are shown in Fig. 3.5. The resulting images for the real and imaginary parts of the permittivity after taking the intersection of the reconstructions that were thresholded at 85 percent of the maximum reconstructed permittivity value are also shown in the figure. Note that results using a CNN trained to reconstruct the imaginary part of the complex permittivity (not shown) are very similar to those using the CNN trained to reconstruct the real part in terms of tumor detection (ROC Curve) and reconstruction performance (RMS error). Thus, the ROC curve in Fig. 4.5 and RMS error in Table 3.2 , were computed using only reconstructions of the real part of the permittivity.

3.4.4 Assessment of Robustness

It is important to assess the robustness of our trained neural network when being tested on images different from those used during training. We investigate four aspects

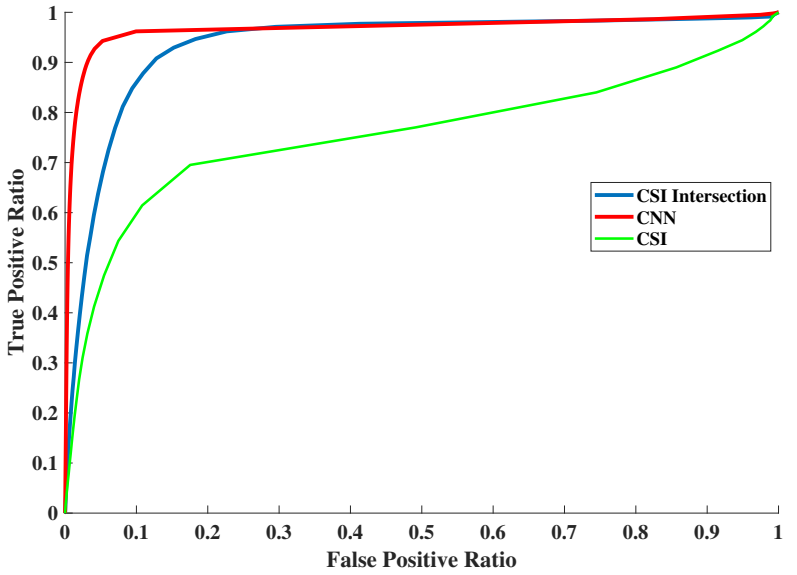

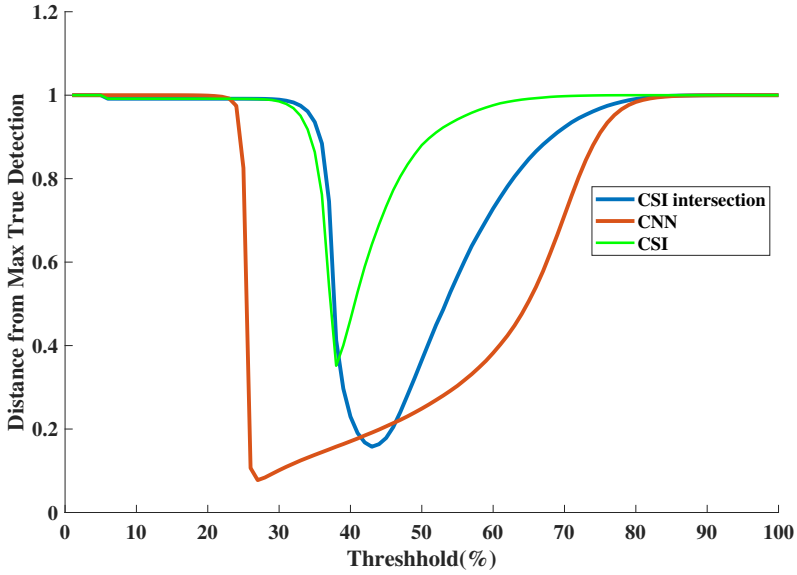

a

b

Figure 3.3: The detection performance using the reconstructed outputs of the CNN and CSI as well as the intersection of CSI reconstructions at the five chosen frequencies. (a) ROC curves derived from the reconstructions. (b) The DMTD curve.

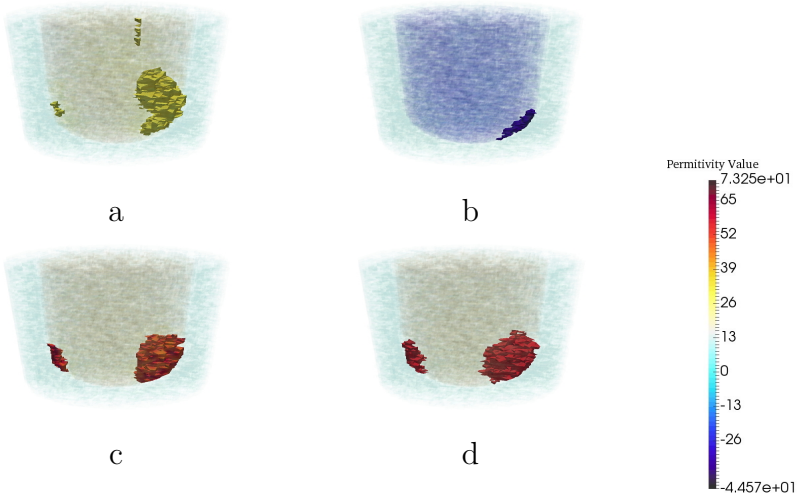

Figure 3.4: Reconstruction results for a particular example with two tumors. The real (a) and imaginary (b) part of CSI reconstruction at 1.1 GHz. (c) CNN reconstruction. (d) Ground truth.

of variation in test data as compared to the training data: (i) Changes in frequencies used to generate CSI reconstructions, (ii) Changes in breast phantom geometry, (iii) Changes in prior-information, and (v) breast phantom with no tumor.

Robustness to changes in frequency

First, given that the CNN was trained utilizing images created at 1.1, 1.2, 1.3, 1.4, and 1.5 GHz, the performance of the trained network was checked qualitatively by testing with CSI reconstructions that were created using data obtained at five arbitrarily chosen frequencies: 1.05, 1.15, 1.25, 1.35 and 1.45 GHz. Therefore, CSI reconstructions at chosen frequencies for five different breast phantoms has been created. These tests indicated that the trained U-Net was indeed superior to the CSI-only case. Results for one test example of the CSI and CNN outputs, from data obtained at 1.05 GHz, are shown in Fig. 3.6. This suggests that the CNN is robust to testing images reconstructed using frequencies in the same bandwidth as used for training (one does not

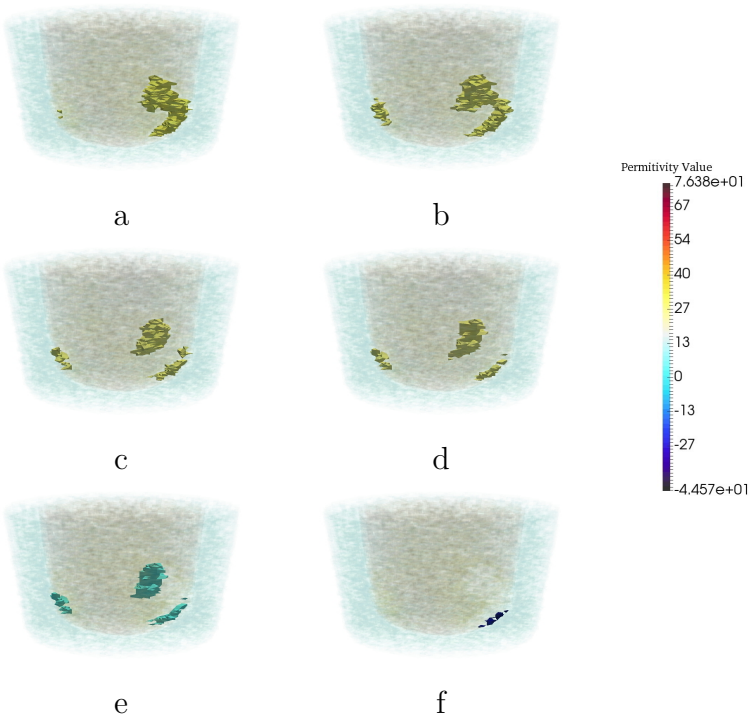

Figure 3.5: CSI reconstructions at four remaining frequencies for the same example as in Fig. 3.4 and resulting images after intersecting images thresholded at 85 percent of the maximum reconstructed permittivity. (a,b,c,d) The real part of CSI reconstructions at 1.2, 1.3, 1.4, and 1.5 GHz. (e) Intersection of real part of CSI reconstructions. (f) Intersection of imaginary part of CSI reconstructions.

have to rely on using the exact same frequencies). As will be seen shortly, however, this is not the case once much higher frequencies are used.

Robustness to changes in breast phantom geometry

The next test for the network's robustess is to check against geometric changes of the breast phantom model. Thus, a new model which has the same dimensions for the fat region but has a smaller fibroglandular region (the height of fibroglandular region is decreased by 0.9 cm) was generated. By using this new small model, five different breast phantoms with a random tumor have been generated to evaluate the trained CNN. Fig. 3.8 demonstrates the performance of the trained CNN for a particular example when the input images were CSI reconstructed images for this new model. As can be seen, the CNN significantly alters the CSI reconstructions (row 1) to bring them closer to the ground truth (row 2).

Robustness to imperfections in prior information

In order to understand the U-Net's ability to remove artifacts, the next test case artificially induces artifacts into the CSI reconstructions by utilizing incorrect, or imperfect, prior information. Clearly, using perfect prior information results in very good CSI reconstructions; however, perfect prior information regarding the structural shape of the fibroglandular region as well as the permittivity of the fibroglandular tissue is difficult to obtain in practical circumstances. It is well known that using CSI with imperfect prior information produces various reconstruction artifacts. To evaluate this aspect of robustness we introduced 10 percent error in the permittivity of the fibroglandular tissue used as prior information. Fig. 4.8 shows the performance of the CNN when tested with CSI reconstructions using imperfect permittivity in a

structurally perfect fibroglandular region. The ROC curves created from the CSI and CNN outputs corresponding to this case shown in the plots of Fig. 3.9. From the green colored curves we see that the CNN-enhanced reconstructions do provide an improvement over the CSI reconstructions. The distance-to-maxTD curve in Fig. 3.9 clearly shows that the range in threshold that could be used for good detection for the CNN-enhanced reconstructions is much wider than that could be used for the CSI reconstructions. When imperfect structural prior was used for a test case it was found that neither the CSI nor the CNN reconstructions performed well. This is the last test performed using synthetically generated images.

Robustness to breast phantom with no tumor

last, given that the CNN was trained only on breast phantom in presence of tumor, the last test in this section has been done to check the performance of the trained CNN for breast phantom with no tumor. Note that to prevent having zero scattered field data, we have to use imperfect prior information. We introduced 5 percent error in the permittivity of the fibroglandular tissue used as prior information. Fig 3.10 demonstrates the performance of the trained network when the input images were CSI reconstructed images with no tumor.

3.5 Experimental Tests and Results

The experimental setup described in [28, 94] was used to collect data to test the described neural network. A depiction of the imaging chamber and the breast phantom used in the experiment is shown in Fig. 3.11. This chamber has 44 facets and contains 24 magnetic field probes and the breast phantom used in the chamber has three regions with similar sizes and properties to those of the numerical breast phantom

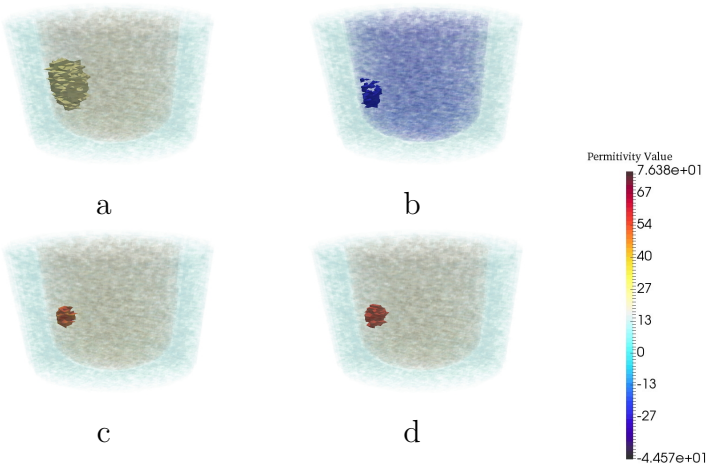

Figure 3.6: Reconstruction results for a particular example with one tumor at 1.05 GHz. The real (a) and imaginary (b) part of CSI reconstruction. (c) CNN reconstruction. (d) Ground truth.

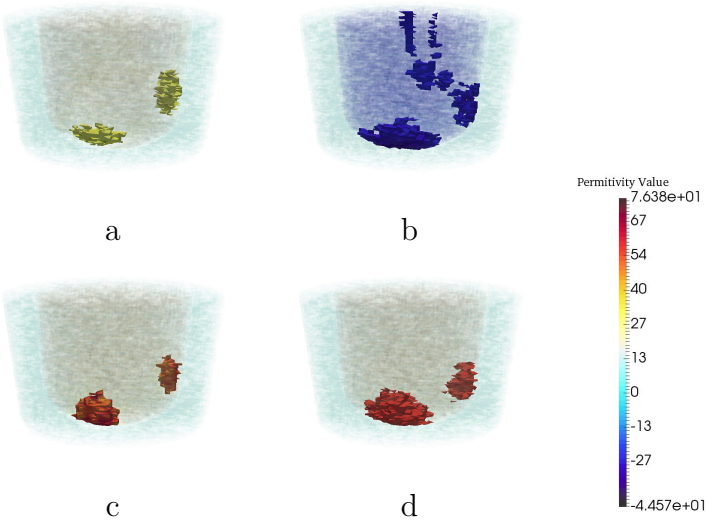

Figure 3.7: Reconstruction results for a particular example with two tumor when the training images are CSI results with perfect prior information but the neural net was tested on imperfect prior information. The real (a) and imaginary (b) part of CSI reconstruction. (c) CNN reconstruction. (d) Ground truth.

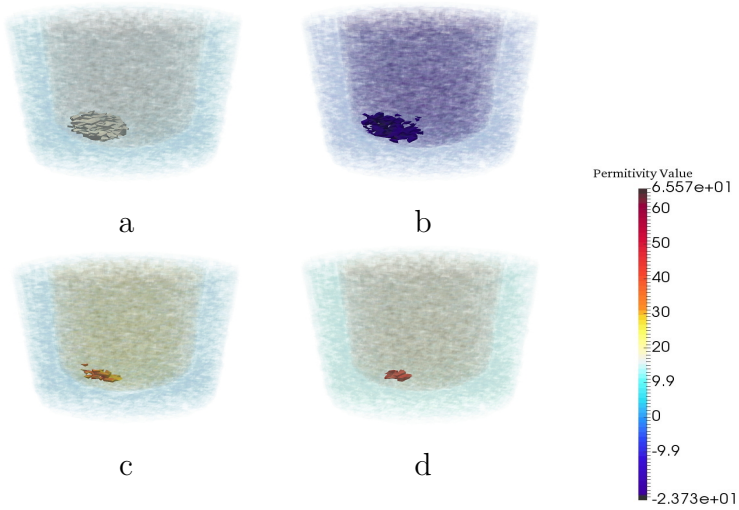

Figure 3.8: Reconstruction results for a particular example when the test images are CSI results for a breast phantom having a smaller fibroglandular region than those of the training set. The (a) real and (b) imaginary parts of the CSI reconstructions. (c) CNN reconstruction. (d) Ground truth.

described earlier for the fat and fibro regions; a 2 cm spherical phantom was used as the tumor region with properties similar to that of the tumor described in the numerical test cases. To mimic the properties close to those of a realistic breast, the fat region was filled with canola oil while a 20:80 ratio of water to glycerin is used to fill the fibroglanduar shell, and a 10:90 ratio of water to glycerin is used to fill the spherical inclusion representing a tumor. For these ratios, the permittivities of the canola oil and water/glycerin mixture are measured as 3.0-j0.193, 23.3-j18.1 and 50-j25 respectively for fat, fibrogladular, and tumor at 1.1 GHz [28]. It is worth noting that this simplistic phantom is used as a simple proof of concept target for inverting a high contrast multilayered medium in an air background and not testing the system against realistic breast phantoms.

In medical imaging, sometimes it is difficult to build a large experimental training data set. Therefore, it is desirable that a neural network trained on synthetic

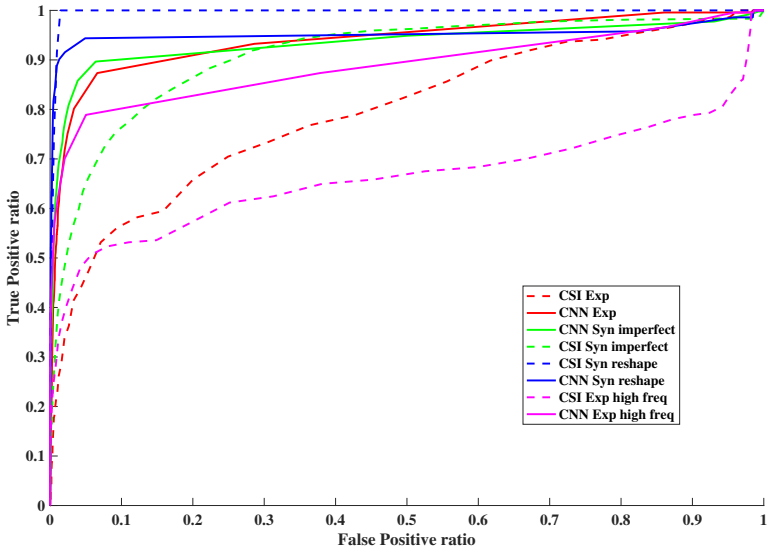

a

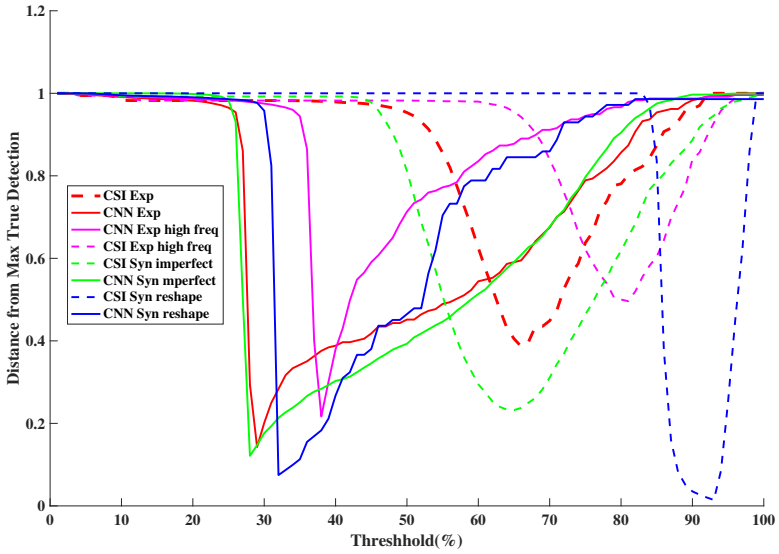

b

Figure 3.9: Detection performance based on the reconstructed outputs of CNN and CSI. (a) ROC curves derived from the reconstructed real part of the permittivity from CSI and CNN. (b) The DMTD. test cases are: Synthetic: imperfect permittivity prior, and true breast phantom with elongated fibroglandular region. Experimental: using data within the frequency band and much higher than the training frequency band.

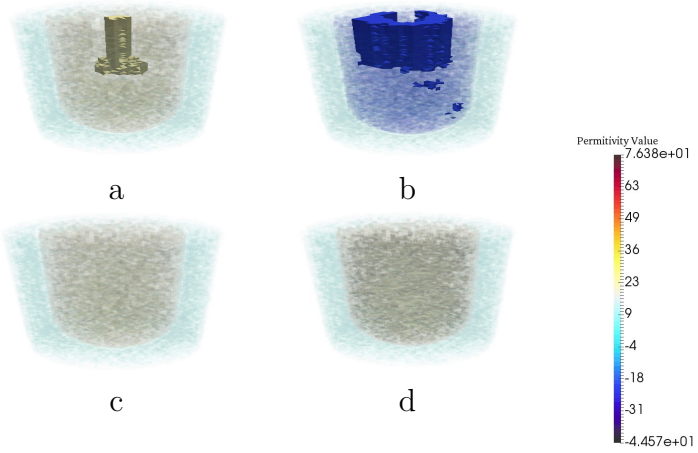

Figure 3.10: Reconstruction results for a particular example when the training images are CSI results with one or two tumors but the neural net was tested on a phantom with no tumor. The real (a) and imaginary (b) part of CSI reconstruction. (c) CNN reconstruction. (d) Ground truth.

data generalizes well when tested on experimental data. To investigate this, we collected experimental data using a wide range of frequencies (1.1 to 2.9 GHz). The performance of the trained network for experimental data is evaluated and shown in Fig. 3.11. Results illustrate that trained CNN improved the experimental CSI reconstructed images when frequencies similar or close to those for training data were used. However, when we tested the trained CNN with experimental images created with frequencies well beyond the band of frequencies used to create the training data, it is observed that that CNN is not able to detect the tumor. Fig. 3.13. One reason for this can be the significant change in the nature of the artifacts. In general, for the results presented in this manuscript, the artifacts at almost all lower frequency reconstructions have a lower permittivity compared to the value of the reconstructed tumor. However, the permittivities of the reconstruced artifacts at higher frequencies are higher than those of the reconstructed tumor.

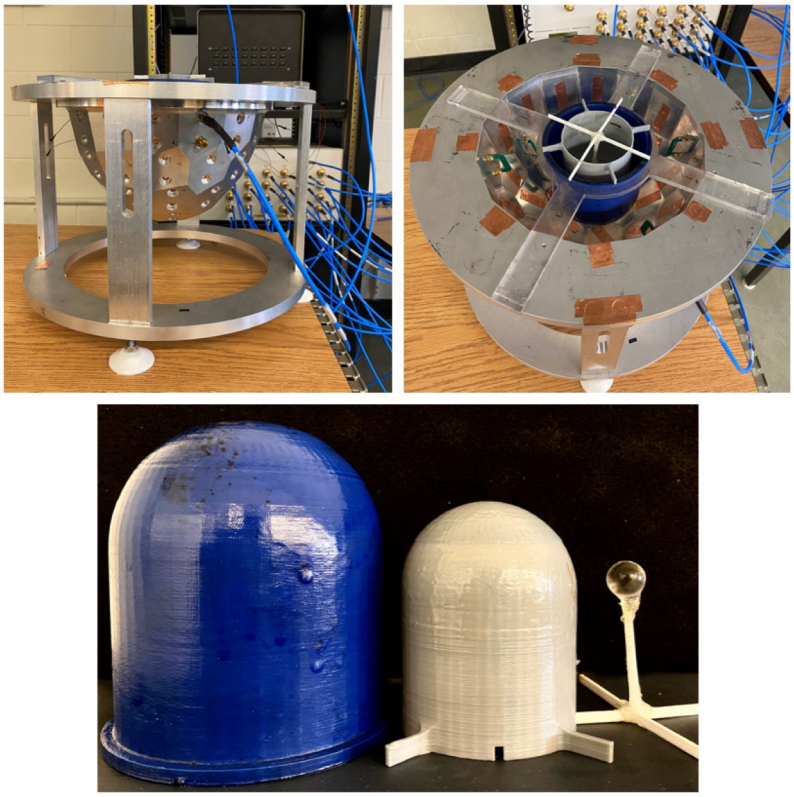

Figure 3.11: The experimental system including the three region breast phantom (Diameter of fat, fibroglanduar and tumor regions are 10,8 and 2 CM respectively).

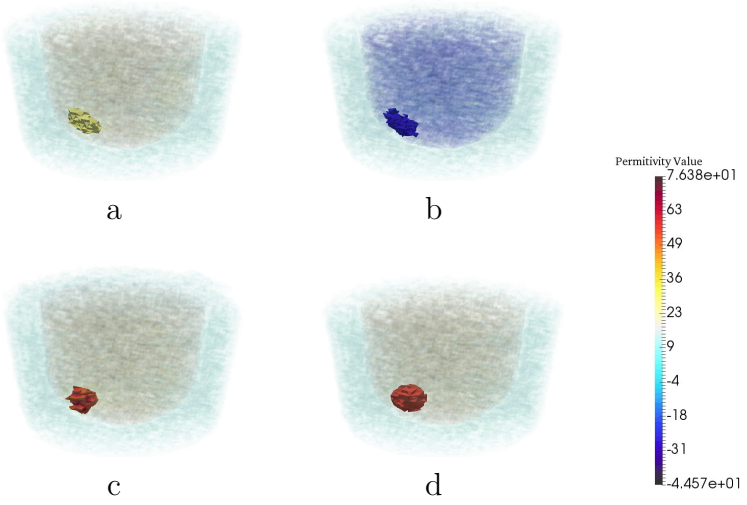

Figure 3.12: CNN performance for experimental result when the neural net was trained on Synthetic data. The real (a) and imaginary (b) part of CSI reconstruction. (c) CNN reconstruction. (d) Ground truth.

3.6 Conclusion

A deep learning technique using a 3D CNN was developed to improve the imaging performance of 3D MWI of the breast. The improvement manifests as the removal of artifacts in the 3D reconstructions of the complex-valued permittivity of the breast being imaged. These reconstruction artifacts are specific to the MWI system wherein the microwave scattered-field data is collected as well as to the numerical inversion algorithm, in our case CSI, being used to create the images. Using synthetic 3D images that take both these factors into account, a CNN was trained with the goal to reproduce the true permittivity image of the breast from the artifact-laden 3D reconstructions. The trained CNN was tested with synthetic images as well as with images created using experimentally obtained microwave scattered-field data from a MWI system: the same MWI system for which a numerical model was utilized in the

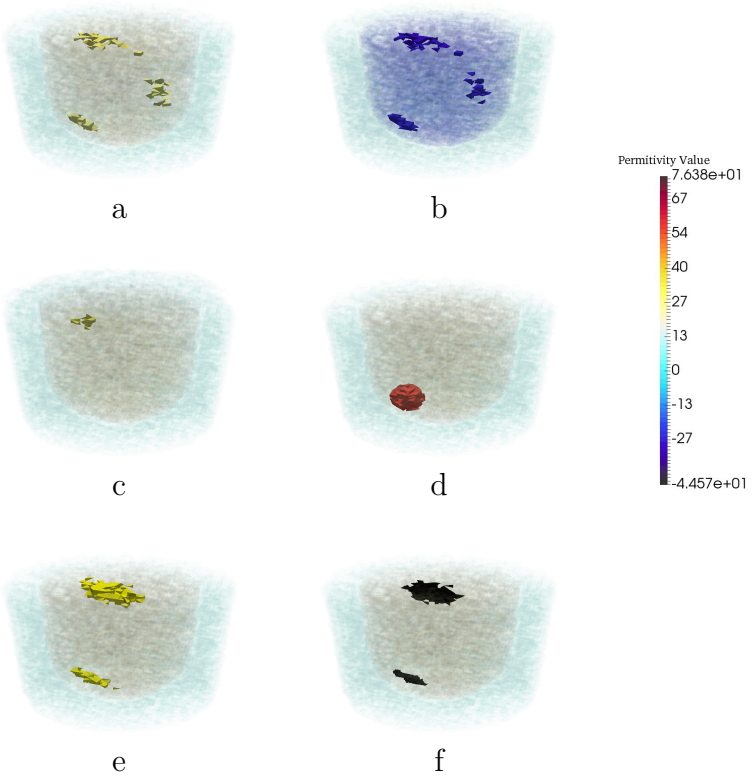

Figure 3.13: Reconstruction results for a particular example when the test images are CSI results in high frequencies but the neural net was trained on low frequencies. The real (a) and imaginary (b) part of CSI reconstruction. (c) CNN reconstruction. (d) Ground truth. (e) Intersection of real part of CSI reconstruction at all frequencies.(f) Intersection of imaginary part of CSI reconstruction at all frequencies(two intersection images are binary image)

creation of the synthetic 3D images.

The RMS error between the CNN-reconstructed images and the true images are improved over the corresponding error between the CSI-only reconstructions and the true images. In addition, tumor detection was evaluated using ROC-AUC metrics and these are much improved for the CNN-reconstructed images over the ROC-AUC results for the CSI-only reconstructions. The results show that this deep learning technique has the ability to improve 3D CSI reconstructions in three interdependent ways. First, and foremost, the CNN has shown its ability to remove reconstruction artifacts which are a great challenge for quantitative MWI. Secondly, the trained CNN successfully corrects the permittivity values which tend to be undershot in the CSI reconstructions. Finally, from a qualitative perspective, the tumor location is more accurately reconstructed with respect to its true position and size.

There are several limitations of this work, but the most critical is that numerical phantoms with a single, relatively simple, fibroglandular region were utilized for training and testing. This same region was reproduced in the physical phantom utilized for the experimental results. Our experience with utilizing a similar technique with 2D images showed that this limitation can be removed by training with breast models having several types of fibroglandular regions. Similarly, this work has shown that when the artifacts are due to reconstructions obtained from data generated with MWI system parameters that were not utilized in the training set, for example artifacts generated by using microwave frequencies that are much higher than what the MWI system was designed for, then the trained CNN was not able to identify these as artifacts. In fact, some of these artifacts were identified as tumors. This result limits the robustness of the trained CNN but this study has provided a good understanding of that robustness. We further note that due to the significant level of

computational resources required during the generation of forward data and inverse 3D CSI reconstructions, we generated only a moderately sized dataset consisting of 600 phantoms. Being aware of the limited number of training examples, we made extensive use of cross-validation and regularization techniques to avoid the possibility of model overfitting, which is evidenced by the generalization our CNN demonstrates on unseen examples. That said, having more training data would potentially help us to train a more robust CNN with better generalization properties. Techniques for overcoming some of these limitations will be investigated in planned future work.

4

Paper3: A Multi-Branch Deep Convolutional Fusion Architecture for 3D Microwave Inverse Scattering: Stored Grain Application

---

4.1 Abstract

In this paper, a multi-branch deep convolutional fusion architecture is proposed to solve electromagnetic inverse scattering problems. The conventional methods for solving inverse problems face various challenges, including strong ill-conditioning, expensive computational cost, and unavoidable intrinsic non-linearity. To overcome these difficulties, we designed a novel multi-branch Convolutional Neural Network (CNN) to reconstruct the 3D images of the moisture distribution in stored grain. Inspired by objective-function techniques for solving the electromagnetic inverse scattering problems, the proposed CNN architecture takes in the scattered-field data and prior information to produce 3D images of the moisture content. With the aim of using inputs of different formats, i.e., a complex-valued vector of scattered-field data and a 3D image of the background moisture distribution as prior information, we propose a multi-branch architecture consisting of decoder-only, and encoder-decoder, convolutional branches. The two branches are later fused to produce the final reconstructed

3D image. To train the CNN, we use the true numerical grain moisture distribution image, which were synthetically generated. The reconstructed moisture distribution images produced by the proposed CNN show that the network is not only able to reconstruct the 3D moisture distribution images directly from measured scattered-field data for high contrast objects-of-interest, but it also achieves a higher imaging quality compared with traditional inversion techniques in microwave imaging. Quantitative evaluations are reported using Receiver Operating Characteristics (ROC) curves for the hotspot detectability and RMS error. The proposed approach opens a novel path for the deep learning-based real-time quantitative microwave imaging.

4.2 Introduction

Microwave imaging has been used for a broad range of imaging applications such as breast cancer detection and treatment monitoring [3], subsurface prospecting [98], and stored-grain monitoring [5]. During the past few decades, different techniques have been developed to solve the associated quantitative inverse scattering problem which is ill-posed and nonlinear. Obtaining highly accurate reconstructions of the complex-valued permittivity generally requires the use of computationally expensive iterative techniques. This is especially true when trying to image highly inhomogeneous scatterers with high contrast values. Even with the advancements made during the last twenty years, images containg reconstruction artifacts still remain an issue, and for biomedical imaging the resolution is still much lower when compared to other available modalities. For industrial applications, such as the monitoring of stored grain, the resolution may not be an issue but the accuracy of the reconstructed complex valued permittivity is an issue, as is the high computational cost of traditional electromagnetic inversion techniques [19, 30–32].

In addition, for most cases the permittivity, an electromagnetic property, is not the desired final outcome. In biomedical imaging, for example, the desired result may be an image of tissue-types [50], or a classification of cancerous versus non-cancerous tissues (*i.e.*, tumor or cancerous tissue detection). In the stored-grain application, one is interested in the moisture content of the grain as a function of position within the grain bin. Thus, there is an implied mapping from the complex-valued permittivity to the physical property of interest. Such a mapping is difficult to incorporate directly into traditional inverse scattering algorithms although some progress has been made in this direction [51]. This subsequent mapping may also add to the inverse problem, now being defined as going from the electromagnetic field data to the property of interest. In some cases, an analytic expression for such a mapping may not be available (we discuss this below with respect to the moisture content of grains).

The safe storage of grains is crucial to securing the world's food supply. Estimates of storage losses vary from 2 to 30% depending on geographic location [99]. Grains are usually stored in large containers, referred to as grain silos/bins, after harvest. Because of non-ideal storage conditions, spoilage and grain loss are inevitable. Consequently, continuous monitoring of the stored grain is an essential part of the post-harvest stage for the agricultural industry. Recently, MWI has been proposed to monitor the stored grain [10,11]. The possibility of using electromagnetic waves to quantitatively image grains, and the motivation to do so, derives from the well-known fact that the dielectric properties of agri-cultural products vary with their physical attributes, such as the moisture content and the temperature, which, in turn, indicates their physiological state.

Deep learning techniques, in particular, convolutional neural networks (CNNs)

have already been applied to a very broad range of scientific and engineering problems. These include applications such as natural language processing, computer vision, and speech recognition [33]. Convolutional neural networks have also been applied to medical imaging for segmentation [40, 41], as well as detection and classification [42–44]. For the case of medical imaging DL techniques have been well investigated for many of the common modalities [47]. CNNs are deep neural networks that were designed specifically for handling images as inputs. In CNNs, the parameterized local convolutions, at successively subsampled image-sizes, allow learning feature maps at multiple scales of pixel-organization [**?**]. Historically, the most popular use of CNNs was as image classification neural networks [34–36]. However, with the advent of encoder-decoder architectures [37, 38], CNNs, and their variants, are increasingly being used for learning tensor-to-tensor (e.g. image-to-image, or vector-to-image) transformations, thereby enabling various data-driven, and learning based image reconstruction applications [39]. Here, we propose a CNN architecture for the application of electromagnetic imaging of grain bins which is an example of an electromagnetic inverse scattering problem.

In the case of electromagnetic inverse problems, researchers have been applying machine learning techniques to improve the performance of microwave imaging (MWI). State-of-the-art deep-learning-based MWI techniques fall into two categories. In the first category, CNNs have been combined with one of the traditional algorithms to enhance electromagnetic inversion's performance. Using DL as a prior (or regularization) term [13]; or using DL techniques as post-processing method for denoising and artifact removal [85, 100] have been studied to indicate the performance of combination of deep learning with traditional methods. In the second category, DL techniques are employed to reconstruct the image directly from the measurement

data [58, 101]. This second category is still quite preliminary but promising results have been published.

While promising studies have been done in using DL techniques to reconstruct the image directly from the measurement data for other imaging modalities like MRI [45] and Ultrasound [46], there is a great need to investigate how deep learning can be utilized to perform the inversion in microwave imaging. Most recently, Li et al. tried to utilize a deep neural network for nonlinear electromagnetic inverse scattering. They have shown that proposed DNN can learn a general model approximating the underlying EM inverse scattering system. However, the targets they used are simple homogeneous targets with low contrast. Besides, they are only limited to 2-D inverse problems [56]. In real-world imaging problems, the electromagnetic fields scatter, and propagate through three-dimensional (3D) objects. However, researchers usually attempt to simplify this 3D problem to a 2D model in order to reduce the time of image reconstruction and decrease the computational complexity. Studies have shown that using a 2D model can increase the level of artifacts in reconstructed images. In addition, when the object of interest is small, there is a chance that it places between two consecutive imaging slice; then, the reconstruction algorithm would not discover the target. Therefore, having a viable 3D imaging technique is vital for having an appropriate reconstruction technique [23].

In this study, a new convolution neural network architecture has been designed to directly reconstruct the 3D images of the moisture content (MC) of grain from the acquired electromagnetic field measurement data. Indeed, the proposed CNN learns a reconstruction mapping from the sensor-domain data (a complex-valued data array of transmitter-receiver measurements) to a 3D image of the MC. To the best of the author's knowledge, it is the first time that it is taken into account the fact

that in most imaging applications where electromagnetic inversion is utilized, the property of interest is somewhat distant from the complex-valued permittivity. One of the advantages of DL using CNNs is that the nonlinear transformation from the acquired raw data to the image of the desired property does not have to be explicitly modelled. Taking the stored-grain moisture monitoring application as an example a DL CNN could potentially learn (implicitly) the mapping from the collected scattered electromagnetic field data to a 3D moisture distribution throughout the grain. This by-passes, or at least ameliorates the so-called modelling error that can plague the use of traditional inverse scattering approaches. The trained CNN model achieves a higher imaging quality compare with traditional inversion techniques in microwave imaging. Note that using the trained CNN models enable us to use microwave imaging for online monitoring applications by eliminating the reconstruction time.

A brief description of the EM inverse scattering and how deep learning techniques would be utilized EM inverse scattering is provided in section 4.3.In the last part of this section, the proposed CNN architectures are described. Section 4.4 provide detailed information about the training data set and the parameters used for the network training. In continue, quantitative assessment and assessment of robustness for numerical experiments are described in section 4.5. Finally, in section 4.6 conclusion and explain our future work are presented.

4.3 Machine Learning Approach for EM inverse scattering

Electromagnetic (EM) inverse scattering can be formulated in several ways. This includes the different possible formulations of the forward model as well as the inverse

problem formulation which in our case takes the form of minimizing a functional. Therefore, part A describes the forward and inverse scattering problems as taken in this research. This provides a convenient comparison between the objective-function utilized in the classical formulation of the inverse scattering problem and learning techniques employed herein. We cast the classical inverse scattering problem in a general form for greator applicability. Next we provide a specific formulation of the inverse scattering problem, the Contrast Source Inversion (CSI) technique, one the most successful iterative methods, to set the context for our numerical examples which are performed using CSI with a Finite-Element (FEM) forward model (referred to as FEM-CSI).

4.3.1 Theory and formulation of Inverse Scattering

The representative configuration for a 2D electromagnetic inverse scattering (EMIS) problem is shown in Fig. 4.1. Note that while all the results presented in this paper deal with 3-D EMIS, here the 2-D problem is used to demonstrate inverse scattering methodology. As shown in Fig. 4.1, an imaging domain $\mathcal{D}$ is defined within the problem domain Ω. The illuminated scattered-field E^s is measured at M receiver locations around the object-of-interest (OI) on the surface $\mathcal{S}$. The OI is represented using the complex-valued relative permittivity $\epsilon_r(r)$ as a function of position. Typically, this is converted to the so-called contrast function $\chi(r) \triangleq \frac{\epsilon_r - \epsilon_{rb}}{\epsilon_{rb}}$ which for an air background, $\epsilon_{rb} = 1$, simply becomes $\epsilon_r - 1$.

The electromagnetic forward and inverse model can be conveniently written utilizing the Green's function integral equation:

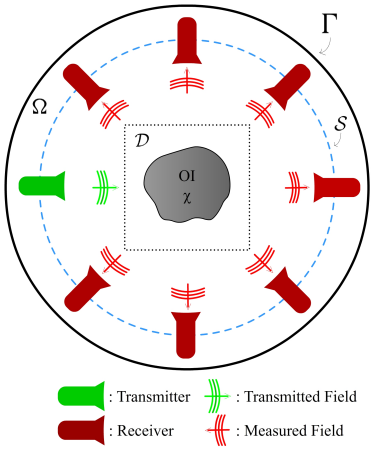

Figure 4.1: Schematic representation of a wavefield imaging setup.

$$E^s(r) = k_0^2 \int_{\mathcal{D}} G(r, r')\chi(r')E(r')dr' \tag{4.1}$$

where $G(r, r')$ is the Green's function for the problem which must be determined, r' is the integration variable that varies over the object domain $\mathcal{D}$, and r represents the position vector at any location within Ω. This integral equation relates the total field E to the scattered field E^s.

When the position vector is taken on the measurement surface $\mathcal{S}$, denoted r_R, this equation is refered to as the "data equation". It then describes the measured scattered field $d \triangleq E^s(r_R)$, the data, as a function of the total-field E and the contrast χ, both of which are unknown. Even if the total-field were known within $\mathcal{D}$ this would still represent an ill-posed first-kind linear integral equation for the contrast given the data d.

Alternatively, when the position vector is taken everywhere within Ω, and the contrast is assumed to be know, this equation becomes the so-called the "state" or "domain" equation which is a second-kind linear integral equation for the total-field.

Typically it is written as

$$E(r) = E^i(r) + k_0^2 \int_{\mathcal{D}} G(r, r')\chi(r')E(r')dr' \tag{4.2}$$

where the incident-field $E^i(r)$ is explicitly written, because it is the field within Ω in the ansence of the OI which can be easily modelled. The domain equation allows us to determine the total-field given the contrast and is typically a well-posed problem.

The final goal of EMIS problems is to reconstruct the relative permittivity ϵ_r of an OI from measured data d on S. The nonlinearity of the data equation generally means that iterative methods must be used that iterate between solving for the contrast in the data equation using an assumed total-field and solving for the total-field in the domain equation using an assumed contrast.

Alternatively, these two equations can be combined within an objective function $\mathcal{F}$ that is minimized with respect to both unknowns. In this paper, the CSI cost-functional, $\mathcal{F}^{\text{CSI}}$, is utilized which is formulated using the contrast sources , $w_t \triangleq \chi E_t$, which vary with transmitter t and the contrast, χ (see [24] for details). This functional is constructed as the sum of normalized data-error and domain-error functionals written as

$$\begin{aligned} \mathcal{F}^{\text{CSI}}(\chi, w_t) &= \mathcal{F}^{\mathcal{S}}(w_t) + \mathcal{F}^{\mathcal{D}}(\chi, w_t) \\ &= \frac{\sum_t \|d_t - \boldsymbol{\mathcal{M}}_{\mathcal{S}}\boldsymbol{\mathcal{L}}[w_t]\|_{\mathcal{S}}^2}{\sum_t \|d_t\|_{\mathcal{S}}^2} + \\ &\quad \frac{\sum_t \|\chi \odot E_t^i - w_t + \chi \odot \boldsymbol{\mathcal{M}}_{\mathcal{D}}\boldsymbol{\mathcal{L}}[w_t]\|_{\mathcal{D}}^2}{\sum_t \|\chi \odot E_t^i\|_{\mathcal{D}}^2} \end{aligned} \tag{4.3}$$

For each transmitter t, $\mathcal{F}^{\mathcal{S}}$ is the norm of the difference of the measured scattered-field data, d_t, and the calculated scattered-field $\boldsymbol{\mathcal{M}}_{\mathcal{S}}\boldsymbol{\mathcal{L}}[w_t]$ at the receiver locations.

Assuming an FEM model, the matrix $\boldsymbol{\mathcal{L}}$ is the inverse of the FEM matrix operator that transforms contrast source variables w_t in $\mathcal{D}$ to scattered-field values within the whole domain Ω, and the matrix operator $\boldsymbol{\mathcal{M}}_{\mathcal{S}}$ transforms field values from Ω to receiver locations on the measurement surface $\mathcal{S}$

On the other hand, $\mathcal{F}^{\mathcal{D}}$ is a functional over the imaging domain $\mathcal{D}$. It's calculated using an FEM model of the incident-field E_t^{inc} within $\mathcal{D}$, as well as the contrast, χ, and contrast sources w_t. Here, the matrix operator $\boldsymbol{\mathcal{M}}_{\mathcal{D}}$ transforms values from Ω to points inside $\mathcal{D}$. The notation $a \odot b$ denotes the Hadamard (*i.e.*, element-wise) product.

The CSI objective functional $\mathcal{F}^{\text{CSI}}(\chi, w_t)$ is minimized by updating the contrast sources w_t and the contrast χ variables sequentially in an iterative fashion using the conjugate gradient technique:

$$\underset{\chi, w_t}{\operatorname{argmin}}\ \mathcal{F}^{CSI}(\chi, w_t) \tag{4.4}$$

Full details of the method can be found in [24]. It should be noted that $\mathcal{F}^{\mathcal{D}}$ does not depend on the collected data and is sometimes referred to as the "Maxwellian regularizer". It is formulated using the forward model for the EM problem.

4.3.2 Objective-function vs. Learning Approaches

Methods for solving the inverse scattering problems can broadly be categorized into two types: (i) Objective-function based approaches, (ii) Data-driven learning techniques. Traditional EMIS iterative methods, such as the CSI method just described, are classified as objective-function approaches, also known as model-based approaches. These methods attempt to solve for a desired unknown, say a property image I_p, by

minimizing an inverse problem cost-function in terms of collected data d. For the above CSI formulation, the property image would be $I_p = \chi(r)$ or $\epsilon_r(r)$. The general form of the inverse problem cost-function can then be written as

$$\underset{x}{\operatorname{argmin}}\ E_0\left\{F(I_p), d\right\} + R(x) \tag{4.5}$$

where $R(x)$ is as a regularization function which depends only on the unknown to be reconstructed, x. In the CSI formulation, E_0 represents the data-error functional, $\mathcal{F}^{\mathcal{S}}$, whereas R represents the Maxwellian regularizer, $\mathcal{F}^{\mathcal{D}}$, and the forward model is represented by F.

Unlike the objective cost-function approaches which require an accurate forward model to solve the inverse problem, learning approaches do not require that an explicit forward model be known beforehand. Rather they utilize a large amount of data to implicitly learn a forward model while solving the inverse problem.

Learning approaches for inverse problems are classified as supervised learning because they employ a set of N ground-truth images $\{I_p^n\}$ and their corresponding measurements $\{d^n\}$ in the training phase. They learn a map IM_θ, defined by a set of training parameters θ in the space of Θ (i.e, $\theta \in \Theta$). In the training phase, the parameters θ are learned by solving a regression problem:

$$\underset{\theta}{\operatorname{argmin}} \sum_{n=1}^{N} E_L\left\{IM_\theta(x), d^n\right\} + R(\theta). \tag{4.6}$$

which at the end implicitly learns the inverse model IM_θ which maps whatever input is given to the inverse model to a property image. In what follows, the input x will take two forms. In the first case x will be just the acquired scattered-field data, whereas in the second case it will be the scattered-field data in conjunction with some

prior information regarding the background image that is assumed for the incident-field problem. To avoid overfitting, $R(\theta)$ is defined as a regularization function which depends on the training parameters.

In imaging applications the data-error functional, E_L, is often chosen as the pixel-wise mean squared error (MSE) between a desired image and the image that the network outputs. The mapping parameters θ are chosen by minimizing this functional over the training data-set. Once trained, the θ parameters become fixed and IM_θ represents the inverse model. Note that no forward model is required. Then in the testing phase, the trained IM_θ can quickly generate a prediction $IM_\theta(x)$ given new input data.

The objective function approach requires that an optimization problem be solved with each new data set and this is typically quite computationally expensive. On the other hand, the learning approach shifts the computational load to the training phase which is performed only once. When new data is obtained the learning approaches efficiently produces a guess corresponding to that new data.

In addition, obtaining an accurate forward model is crucial for objective function approaches and this can often be quite difficult for some applications like grain monitoring, where the physical property of interest is the moisture content of the stored grain. A forward model which produces predicted scattered-field data given the inhomogeneous moisture content of an unknown amount of grain stored in a grain-bin is quite difficult in its own right. For example, even the mapping from complex-valued permittivity to moisture content is quite difficult to obtain and has been a much studied area for the past several decades [102]. In comparison, the learning approach can be implemented to directly reconstruct any physical property one desires; the main difficulty shifts to one of obtaining a sufficient amount of training data.

4.3.3 Neural Network Architecture

Inspired by the mentioned advantages of learning approaches and to establish a proof-of-concept, we designed two different deep CNN architectures to perform microwave imaging inversion.

Architecture 1: The first architecture we propose is designed to accept, as input, the real and imaginary parts of the scattered field data at different frequencies, and produces, as output, the 3D images of the moisture content. The proposed neural network is a convolutional decoder that consists of two main stages. *Stage 1:* The first stage consists of a stack of four fully connected layers, followed by reshaping of the output of the fourth layer into a 3D image. This stage serves the purpose of transforming the input domain from scattered field data to a 3D moisture distribution image. Dropout layers have been used to prevent overfitting after each fully connected layer. Stage 2: The second stage consists of successive deconvolutional and upsampling layers to produce the reconstructed 3D volume of moisture content. Batch normalization has been used after each convolutional layer to accelerate convergence in the training phase.

Architecture 2: Inspired by several studies that have shown improvement in the performance of objective function based techniques using prior information in addition to the scattered field data [19, 30], and their success in the grain imaging application [5,10,11] we add an image of prior information as input data to our neural network. For the grain application, this consists of a background moisture image of the stored grain. It represents the assumed background for the incident field. The specific details of this prior information can be found in [5, 10, 11].

To incorporate this into our CNN we propose a multi-branch deep convolutional

fusion architecture consisting of two parallel branches as follows: the first branch comprises Architecture1 as described above and takes in the scattered field data as input; the second branch consists of a 3D U-Net that takes in the prior image as input. The U-Net consists of successive convolutional and downsampling layers, followed by successive deconvolutional and upsampling layers. In U-Net architecture, the downsampling side with convolutional layers acts as a feature extraction stage (encoder), while the upsampling side acts a reconstruction network (decoder). Concatenative layers have been added between the corresponding contractive and expansive layers to prevent the loss of information along the contractive path. [37]. The outputs of the two branches i.e. the decoder-only branch (Architecture1) and the U-Net, are then fused together through a parameterized linear combination. Our rationale to use a simple additive fusion approach is to force the individual branches to contribute as much as possible to the reconstruction task, by learning meaningful feature representations along the layers of each branch. Using a complicated fusion model, on the other hand, entails the risk of putting more burden on the fusion model itself; it could learn idiosyncratic mappings, given its complexity, at the cost of not learning intrinsically useful representations along each of the input branches. Moreover, a simple fusion strategy has the added advantage of introducing interpretability to our architecture in terms of how much scattered field data and prior information contribute to the final reconstruction. The schematic for both architectures is shown in Fig. 4.2. and Fig. 4.3.

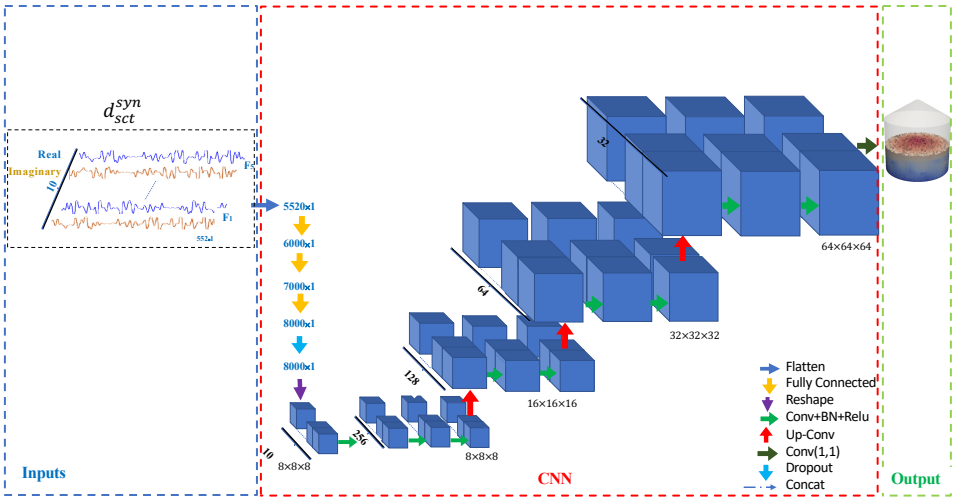

Figure 4.2: Schematic of the Architecture1 for the proposed moisture reconstruction. The input to the network is the normalized real and imaginary part of scattered field data for five different frequencies, and the network is trained to output the corresponding true 3D volume of moisture content.

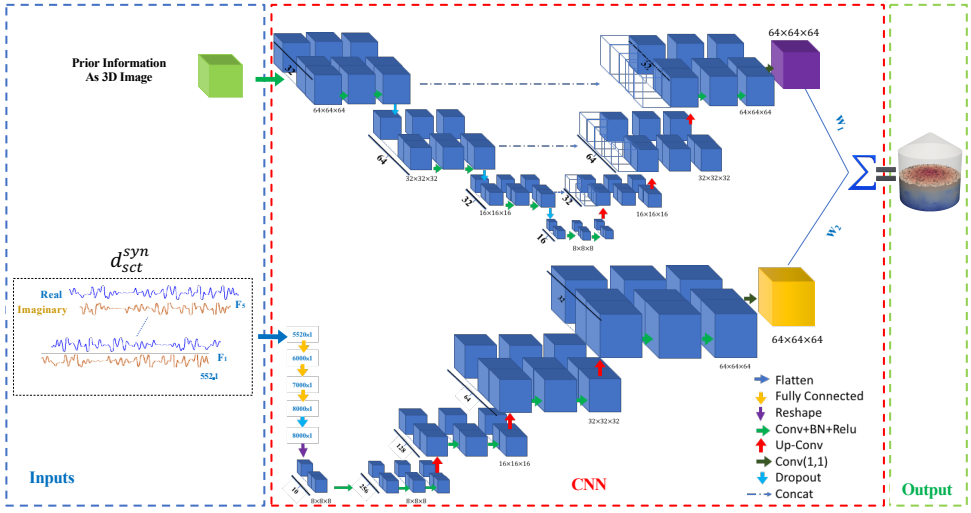

Figure 4.3: Schematic of the Architecture 2 for the proposed moisture reconstruction. The inputs to the network are the normalized real and imaginary part of scattered field data for five different frequencies and prior information as an image, and the network is trained to output the corresponding true 3D volume of moisture content.

4.4 Numerical Experiments

4.4.1 Dataset

In order to train and test the proposed CNNs, a numerical dataset for a full-scale grain bin is generated. To generate the dataset, a 24 ft grain bin, as illustrated in Fig. 3, was modeled in our 3D-FEM electromagnetic field solver algorithm, which is described in [28]. Our dataset consists of 900 numerical grain bins with a random grain height, cone angle, grain's permittivity (corresponding to grain moisture), and high moisture region (hotspot). To achieve a proper grain moisture distribution, two radial basis functions, one at the peak of the grain at the center of the bin, and one at the bottom corner of the bin, with two different mositure values, randomly selected in the range of 12%-17% (on wet bases) for each case, were used. This allowed for modeling a gradient distribution of grain's moisture in the bin with the highest moisture at the center peak of the grain and the lowest moisture at the bottom of the bin. As for the high moisture region, a permittivity of $5.17 - j0.76$, corresponding to a moisture level of 20% for corn (wet bases), was selected. The high moisture regions were added to each model by selecting a random initial tetrahedron within the imaging model, growing it in random directions till a random diameter criterion, selected randomly from 1.1-1.5 m, was satisfied. This procedure is performed at different frequencies, and for the work considered herein, the frequency band of 65 MHz to 77 MHz is used. Finally, the generated data is normalized over the entire training set at each frequency. Then, the normalized data for all frequencies are used as an input to the CNN.

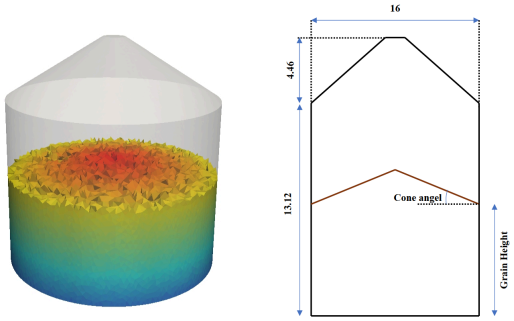

Figure 4.4: Hopper style grain bin layout (dimensions are all in meters) modeled.

4.4.2 Network Training

Python 3.6 and Keras 2.0.6 with Tensorflow backend has been used to implement proposed CNNs. A Windows 10 computer with a Tesla P100 PCIE-12GB graphic processor and Intel(R) CPU(3.50 GHz) is utilized. In order to have an appropriate scale, Xavier initialization was used for the convolutional layer weights [79]. We trained the CNN with a batch size of 5 for 50 iterations using the Adam optimizer [103]. A four-fold cross-validation strategy was utilized to avoid the possibility of overfitting. The real and imaginary parts for five different frequencies are fed to the CNN as input. With 900 grain bins in our dataset, each fold in four-fold cross-validation consisted of 225 examples. For every fold, training was done using 675 cases, while the testing set consisted of the held-out 225 models. Thus all 900 cases featured as test examples when they were not part of the training set. For the loss function, we use pixel wise weighted mean squared error between the ground truth image and the CNN reconstructed image which penalizes the loss within hotspot regions more than elsewhere as follows:

$$RMSError = \frac{1}{LMN}\sum_{x=1}^{L}\sum_{y=1}^{M}\sum_{z=1}^{N}[w_{x,y,z}(I^{GT}_{x,y,z} - I^{CNN}_{x,y,z})]^2 \tag{4.7}$$

where $I^{CNN}_{x,y,z}$ represents a 3D image reconstructed by the CNN and $I^{GT}_{x,y,z}$ represents a 3D ground truth image. $w_{x,y,z}$ represents the weighting mask that is used to emphasize on hotspot region (three for hotspot pixels and one for everywhere else).

4.5 Results

4.5.1 Quantitative Assessment

The Root Mean Squared (RMS) reconstruction error between the CNN reconstructed image and the true moisture distribution image have been evaluated to assess the CNN reconstruction performance for both architectures. In addition, the Area Under the Curve (AUC) of the pixel-wise Receiver Operating Characteristics (ROC) using the reconstructed moisture value as a score has been used to quantify the hotspot segmentation performance. We compare the performance of the two proposed CNNs with the aforementioned conventional inversion technique: the contrast source inversion (CSI) method [24, 76, 81]. The RMS reconstruction error and ROC analysis has also been computed for the FEM-CSI reconstructed images. Furthermore, the distance from any location on the ROC curve to the top-left corner of the plot is another metric that can be used to compare the hotspot segmentation performance (we call this the "distance-to-maxTD" or "DMTD" plot). The ROC curves carry information about how well each approach can distinguish between classes, however, the information about the distributions of thresholds at which the different ratios (false-positives and true-positives) fall are lost in this curve. Therefore, we use the

DTMD curve as a complementary metric to display/analyze the relation between the true-positive detection as well as the threshold at which a certain true-positive to false-positve ratio happens.

The results of this quantitative evaluation using the four-fold cross-validation strategy for all 900 images are shown in Fig. 4.5 and Table 4.1. Based on the AUC and RMS error metrics, it can be concluded that Architecture 2 performs the best in terms of both the accuracy of the reconstructed 3D image and hotspot segmentation. Significantly, Architecture 1 performs worse than FEM-CSI. This is not surprising because FEM-CSI as implemented in this work and described in [76, 81] uses the prior information in addition to the scattered-field data whereas Architecture 1 does not use the prior information. We see that when the deep-learning technique is provided with the prior information, as it is in Architecture 2, it clearly outperforms the conventional imaging technique.

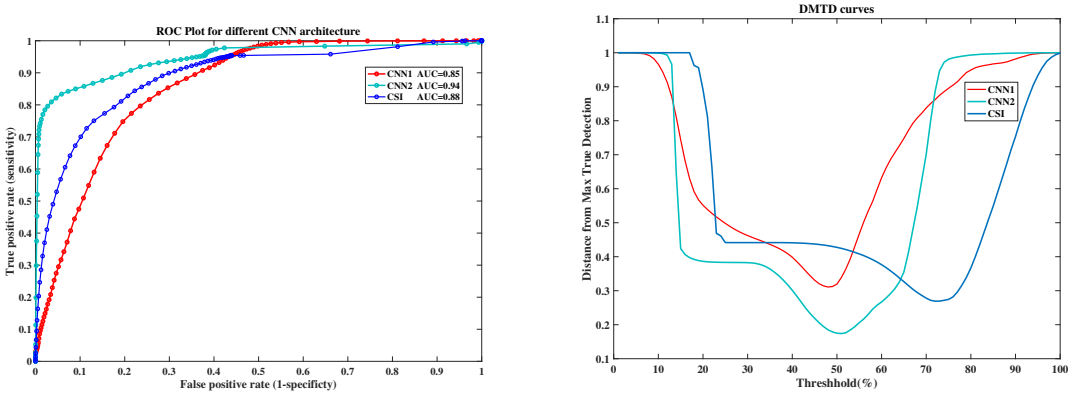

a b

Figure 4.5: The detection performance using the reconstructed outputs of the both proposed CNNs and CSI. (a) ROC curves derived from the reconstructions. (b) The DMTD curve.

Figs. 4.6 and 4.7 provide a qualitative comparison of the performance of the trained model (Architecture 2) in comparison with the CSI reconstruction for two

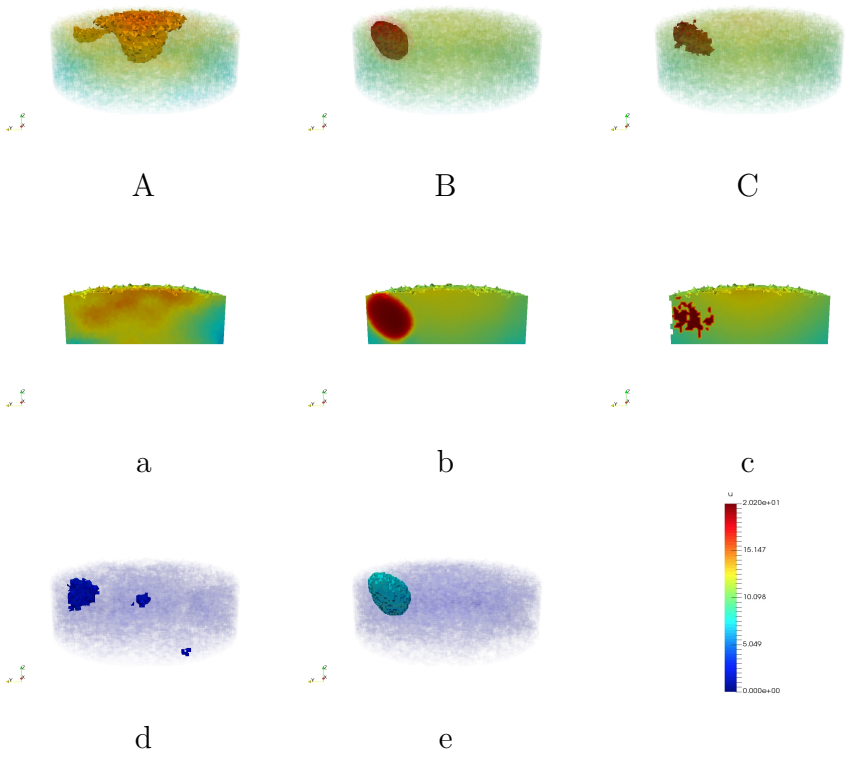

Figure 4.6: Architecture 2 reconstruction results for a particular grain bin (one quarter full bin) with one hotspot. (A) 3D moisture distribution mapped from CSI results at 71 MHz , (B) CNN reconstruction, (C) The Ground truth moisture distribution (a) A vertical slice of 3D moisture distribution mapped from CSI results, (b) A vertical slice of CNN reconstruction, and (c) A vertical slice of ground truth, (e) 3D contrast image (The difference between the prior background and the CSI reconstruction), and (f) 3D contrast image (The difference between the prior background and the CNN reconstruction)

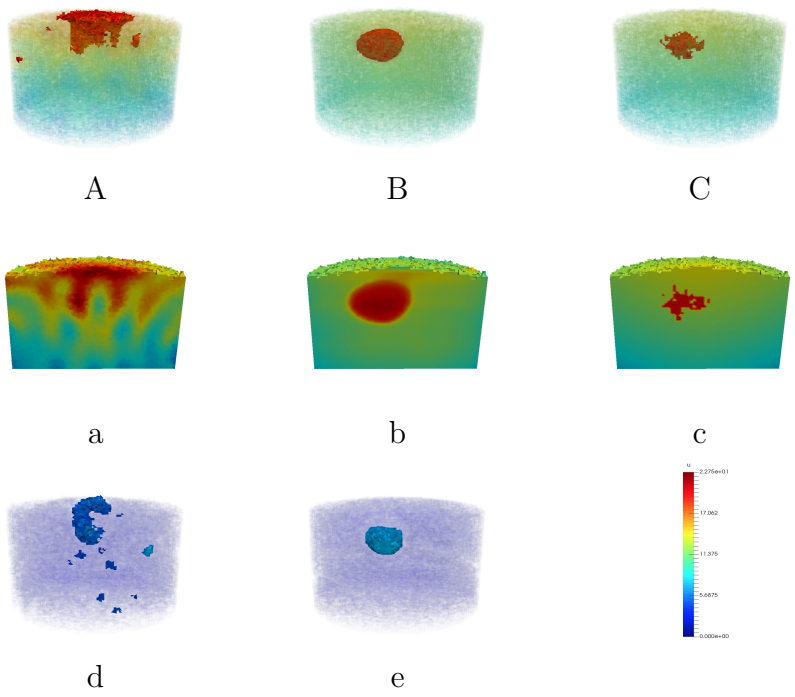

Figure 4.7: Reconstruction results for a particular grain bin (half-full bin) with one hotspot. (A) 3D moisture distribution mapped from CSI results at 71 MHz , (B) CNN reconstruction, (C) The Ground truth moisture distribution, (a) A vertical slice of 3D moisture distribution mapped from CSI results at 71 MHz, (b) A vertical slice of CNN reconstruction, (c) A vertical slice of ground truth, (e) 3D contrast image (The difference between the prior background and the CSI reconstruction), and (f) 3D contrast image (The difference between the prior background and the CNN reconstruction)

Table 4.1: Comparison of reconstruction and tumor detection performance

	CNN1	**CNN2**	**CSI**
RMS Error	1.4	0.9	1.2
AUC	0.85	0.94	0.88

arbitrary examples each consisting of a partially filled grain bin with one moisture hotspot. As was the case in our previous study wherein a CNN architecture was used to enhance the FEM-CSI images [100], these representative images show that the moisture level of the hotspot is more accurately resconstruted by the CNN than by the FEM-CSI algorithm. It has been our experience that FEM-CSI has difficulties in reaching the peak-value of the expected permittivity within the recosnstructed image, especially in 3D. This has been found to be the case for both grain-bin imaging as well as for breast tumor imaging [100].

With respect to artifacts, it is clear that the CNN reconstructed images contain much fewer artifacts. Notice that the FEM-CSI reconstructions produce artifacts at the location where the background moisture level is highest (*i.e.*, near the peak of the grain). The moisture contrast images shown in d) and e) of Figs. 4.6 and 4.7 reveal that these artifacts are not as visible when displaying the thresholded contrast of the moisture compared to displaying the actual moisture shown in a) and b). (The moisture contrast is defined as the hotspot moistuse minus the background moisture.) Of course, this depends on the threshold that is chosen. Note that the top row and bottom row of these figures contain thresholded voxels or tetrahedrals on a transparent 3D image of the moisture level. The colorbar provides the moisture level scale.

4.5.2 Special cases

It is important to assess the robustness of our trained neural network when being tested on images different from those used during training. Therefore, we investigate three aspects of variation in test data as compared to the training data: (i) changes in prior-information, (ii) generalizability to grain bins with more hotspots, and (iii) Grain bin with no hotspot.

Robustness to Imperfections in Prior Information

In order to evaluate the robustness of the proposed model against the noisy data, we generated test cases with artificially induced artifacts into the scattered field data by utilizing incorrect, or imperfect, prior information. Clearly, using perfect prior information results in very good scattered field data; however, perfect prior information regarding the structural shape of the grain region as well as the permittivity of the grain is difficult to obtain in practical circumstances. In previous study [104], it was shown that by using a deep learning model we were able to find the structural shape of the grain region; however, having the exact value of grain permittivity as a prior information is still an open question. It is well known that other inverse scattering techniques, such as CSI, with imperfect prior information produce various reconstruction artifacts. To evaluate this aspect of robustness, we introduced 10 percent error in the permittivity of the grain region used as prior information. Fig. 4.8 shows the performance of the CNN when tested with scattered field data using imperfect permittivity in a structurally perfect grain region. When imperfection increased beyond ten percent, it was found that neither the CSI nor the CNN reconstructions performed well.

Generalizability to grain bin with more hotspots

The next test was designed to evaluate the performance of CNN when the test case has two hotspots while the network was trained on grain bins with only one hotspot. Fig 4.10 shows the performance of the trained CNN for a particular example with two hotspots. As can be seen, the CNN is able to reconstruct the 3D moisture distribution image.

Robustness to grain bin with no hotspot

Given that the CNN was trained only on grain bins in presence of hotspot, we also conduct a test to check the performance of the trained CNN for a grain bin with no hotspot. Note that to prevent having zero scattered field data, we have to use imperfect prior information. We introduced 5 percent error in the permittivity value of the grain region used as prior information. Fig 4.9 shows the performance of the trained CNN when the inputs are scattered field data and prior information image for a grain bin with no hotspot. As can be seen, the CNN is able to reconstruct the 3D moisture distribution image correctly when the test case does not have any hotspot.

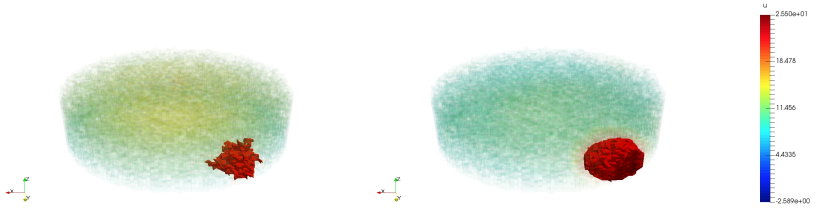

a b

Figure 4.8: Reconstruction results for a particular example with one hotspot when the training inputs are scattered field data which are obtained by utilizing perfect prior information, but the neural net was tested on scattered field data by utilizing imperfect prior information. (a) The Ground truth, (b) CNN reconstruction.

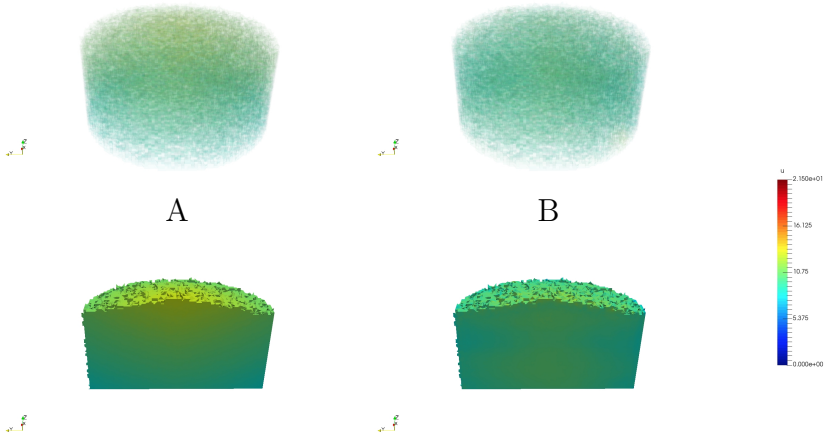

Figure 4.9: Reconstruction results for a particular grain bin with no hotspot. (a) The Ground truth, (b) CNN2 reconstruction, (A) a vertical slice of ground truth and (B) a vertical slice of CNN reconstruction.

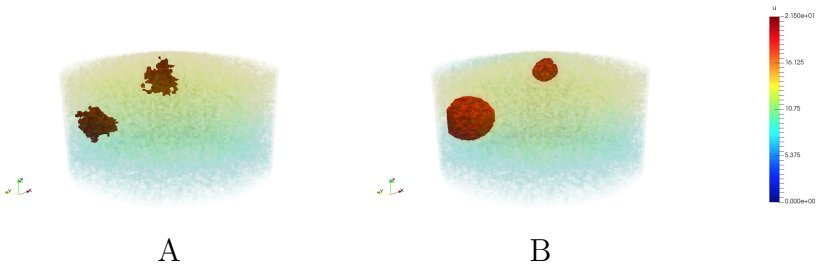

Figure 4.10: Reconstruction results for a particular grain bin with two hotspot. (a) The Ground truth, (b) CNN2 reconstruction, (A) a vertical slice of ground truth and (B) a vertical slice of CNN reconstruction.

4.6 Conclusion

Two new CNN architectures have been proposed to implement physical property imaging using electromagnetic scattered-field data. This effectively solves the electromagnetic inverse scattering problem and goes beyond traditional EM imaging techniques in that we have shown the ability to image physical properties that are more distantly related to the electromagnetic scattering problem than, *e.g.*, permittivity. That is, in the application considered herein it has been shown how the moisture content of stored grain can be directly imaged without first reconstructing an image of the complex-valued permittivity. The CNN architecture producing the best results takes in the raw scattered-field data as well as prior information in the form of a background moisture content image to reconstruct the moisture distribution of stored grain. Training of the CNNs was performed using a synthetically generated dataset consisting of 900 grain bins filled with inhomogeneous grain having a random grain height, cone angle, and a number of randomly sized and located moisture hotspots.

The performance of both proposed CNN architectures was compared to that of the CSI method as a baseline representative of traditional inverse scattering approaches. The RMS error between the CNN-reconstructed images and the true images was improved over the corresponding error between the CSI reconstructions and the true images. In addition, hotspot detection was evaluated using ROC-AUC metrics and these were much improved for the CNN-reconstructed images over the CSI reconstructions. The results show that compared with the CSI method, the proposed deep learning technique improves the reconstructions in different interdependent ways. First, and foremost, while artifacts are a great challenge for quantitative MWI, the proposed CNN was able to remove the artifacts. Secondly, the trained CNN successfully corrects

the moisture values which tend to be undershot in the CSI reconstructions. Finally, the proposed CNN method for electromagnetic inverse scattering problems offers a novel tool to realize quantitative microwave imaging in real-time. The encouraging results motivate future work that will involve the use of experimental scattered-field data obtained from actual grain bins.

5

Conclusions and Future Work

5.1 Conclusions

This thesis was focused on using deep learning techniques to improve microwave imaging. As described in Chapter 1, deep learning could be utilized in different ways in the microwave imaging process. As the first step, in Chapter 2, we developed a convolutional neural network as a post-processing technique to enhance the reconstructed images obtained from the FEM-CSI iterative method. The CNN's input is the 2D tomographic reconstructed image of the complex-valued permittivity of the breast obtained using the CSI technique. The CNN attempts to generate a quantitative 2D image that is much closer to the true permittivity. The results showed that the CNN can remove some of the typical reconstruction artifacts in CSI reconstructed images. The trained CNN improved the RMS error between the reconstructed CNN images and the true permittivity images. In addition, it has been shown that a simple thresholding detection method can accurately detect tumors in the CNN reconstructed images that are not detectable in CSI reconstructions. Our data set contained 1200 numerically generated phantoms; we employed a numerical breast model derived from magnetic resonance tomography images to produce multimodal

MW/US reconstructions. It should be noted that our training examples were generated based on three different types of breast phantoms from the BI-RADS breast density table. The generalizability of the trained network has been assessed by testing the performance of the network when it takes in the examples that differ from the training examples. These test cases vary in terms of breast models and geometric transformations. As expected, the CNN, which was trained with three types of breasts, provides the most robust model: it consistently improved the reconstruction (RMS error) and detection (AUC) performance over the CSI results. The results also show that when particular breast model-types were missing from the training set, reconstruction performance is still improved, but sometimes the detection performance degrades. Therefore, the most significant finding of this research is that having a wide diversity of breast-types in our training dataset would improve the performance and robustness of the final model.

While these results are encouraging, for a real world microwave imaging setting reconstructions are required in 3D. Therefore, in the next chapter, we have developed a 3D CNN to improve the performance of 3D microwave imaging of the breast. Similar to Chapter 2, to enhance the artifact-laden 3D reconstructed images, a 3D U-net based convolutional neural network was developed. It was shown that compared with 2D reconstruction, 3D cases suffer more severely from artifacts (The generated artifacts in reconstructed images are specific to the MWI scattering field data acquisition system and the inversion algorithm (in our case CSI)). The proposed CNN model was trained using 3D synthetic images that take these two factors into account and try to reconstruct 3D images that are much closer to the true permittivity. The results show that the CNN can remove artifacts in the 3D reconstructions of the breast's complex-valued permittivity. To test the CNN's performance, synthetic and experimental

images were used. The experimental images were obtained using microwave scattered-field data from a MWI system. It should be noted that the experimental MWI system is the same as the MWI system for which a numerical model was utilized in the creation of the synthetic 3D images

Since generating forward data and 3D CSI reconstruction images need a significant level of computational resources, a medium-sized dataset (600 phantoms) is generated for the training phase. The CNN's performance on unseen examples proves the generalization of our trained model. Recognizing that access to a bigger dataset in the training phase would potentially improve the generalizability of our model; some of the possible techniques to overcome these limitations are discussed as future works.

The RMS errors show that compared with CSI-only reconstructed images, the CNN-reconstructed images are closer to the true images. Additionally, to evaluate both methods' performance in terms of tumor detection, ROC-AUC metrics have been used. The ROC-AUC results confirm that compared with CSI-only reconstruction, CNN-reconstructed images have better tumor detection performance. Based on these results, we can conclude that the proposed deep learning technique improved the 3D CSI reconstructions in three interdependent ways. First and foremost, the proposed CNN can remove the reconstruction artifacts, which are a critical challenge for quantitative MWI. Secondly, while 3D CSI reconstructed permittivity values tend to be undershot, the proposed CNN successfully corrects the permittivity values. Finally, it has been shown that the size and location of the tumors are reconstructed more accurately with respect to their true position and size.

Using numerical phantoms with a single, relatively simple, fibroglandular region for both the training and testing phase could be considered as the most critical limitation of the study. Our experimental results were also produced based on the same

simple physical phantom. However, our experience with 2D images in the previous chapter illustrates that training the proposed CNN using a large dataset, consisting of several types of fibroglandular regions, can eliminate this limitation. This study also shows that changing the MWI system parameters between the training and testing datasets is the reason for generating reconstruction artifacts (for instance, artifacts caused by using microwave frequencies that are much higher than what the MWI system was designed for), recognizing these artifacts are difficult for the trained CNN. As a matter of fact, sometimes, these artifacts were identified as tumors. This issue limits the robustness of the proposed CNN; however, this investigation provides good insight into the proposed model's robustness.

Finally, in Chapter 4, to the best of the author's knowledge, for the first time a multi-arm deep neural architecture capable of reconstructing the 3D microwave images directly from measured scattered data for high contrast objects-of-interest has been developed. In this chapter, two new CNN architectures have been proposed to implement physical property imaging using electromagnetic scattered-field data. The proposed technique effectively solves the electromagnetic inverse scattering problem and goes beyond traditional EM imaging techniques in that we have shown the ability to image physical properties that are more distantly related to the electromagnetic scattering problem than, *e.g.*, permittivity. That is, in the application considered herein it has been shown how the moisture content of stored grain can be directly imaged without first reconstructing an image of the complex-valued permittivity. The CNN architecture producing the best results takes in the raw scattered-field data as well as prior information in the form of a background moisture content image to reconstruct the moisture distribution of stored grain. Training of the CNNs was performed using a synthetically generated dataset consisting of 900 grain bins filled

with inhomogeneous grain having a random grain height, cone angle, and a randomly sized and located moisture hotspot.

5.2 Future Work

- As discussed in Chapter 2, a wide diversity of breast-types in the training phase of CNNs would improve the generalizability and robustness of the DL model. While, it is more common that large datasets are available in other imaging modalities like MRI, it is often difficult to find large enough data for microwave imaging. One possible solution to overcome this challenge is to create microwave imaging datasets based on existing MRI datasets. It would be beneficial to map the MRI derived images into microwave images in order to have large labeled datasets for training.

- The ability to work effectively with experimental data is the ultimate goal of any MWI technique, including traditional techniques and learning approaches. On the other hand, the calibration of experimental data has been shown to have a significant impact on the performance of both traditional iterative methods and proposed deep learning methods. Therefore, applying state-of-the-art DL techniques as a calibration technique should be considered as a future research direction. Machine learning techniques can improve the calibration performance, thereby enhancing the performance of the final reconstructed image. In addition, as we have shown in Chapter 3, having a reliable calibration would allow us to train a CNN with synthetic data and use the trained model for experimental data. As has been mentioned, it is hard to provide a large labeled experimental microwave dataset in oder to train a CNN with experimental data due to well-known challenges.

- Over the past decades, researchers have gained deep domain knowledge that can be used to devise approximate direct inversion models or effective iterative solvers. Therefore, MWI researchers should try to design new machine learning architectures based on their knowledge about the problem and avoid using DL as a totally data-driven black-box solver. A future approach is to integrate the physical and mathematical information provided by traditional iterative and non-iterative algorithms into CNN architectures to reduce the nonlinearity of the mapping function from the input to the output of models.

- Generative Adversarial Networks (GANs) are generative models that can generate new examples for the training stage. They consist of a generator NN that learns to produce the target output and a discriminator NN that learns to distinguish ground-truth data from the generator's output. Recent studies have demonstrated GANs' capability for data augmentation in other modalities [105, 106]. Besides, based on my experience during this research, the lack of large enough datasets is one of the most critical challenges in utilizing the state-of-the-art deep learning techniques in microwave imaging. Therefore, adjusting GANs architecture based on physical and mathematical microwave imaging knowledge may solve the lack of large enough datasets for supervised learning techniques.

References

[1] A. Abubakar and P. M. Van den Berg, "Non-linear three-dimensional inversion of cross-well electrical measurements," *Geophysical Prospecting*, vol. 48, no. 1, pp. 109–134, 2000.

[2] I. Aliferis, C. Pichot, J.-Y. Dauvignac, and E. Guillanton, "Tomographic reconstructions of buried objects using nonlinear and regularized and inversion method," in *Non-Linear Electromagnetic Systems*, ser. Studies in Applied Electromagnetics and Mechanics. IOS Press, 2000, pp. vol.18, 237–240. [Online]. Available: https://hal.archives-ouvertes.fr/hal-00980396

[3] P. M. Meaney, M. W. Fanning, Dun Li, S. P. Poplack, and K. D. Paulsen, "A clinical prototype for active microwave imaging of the breast," *IEEE Transactions on Microwave Theory and Techniques*, vol. 48, no. 11, pp. 1841–1853, 2000.

[4] A. H. Golnabi, P. M. Meaney, S. Geimer, and K. D. Paulsen, "Microwave imaging for breast cancer detection and therapy monitoring," in *2011 IEEE Topical Conference on Biomedical Wireless Technologies, Networks, and Sensing Systems*, 2011, pp. 59–62.

[5] M. Asefi, I. Jeffrey, J. LoVetri, C. Gilmore, P. Card, and J. Paliwal, "Grain bin monitoring via electromagnetic imaging," *Computers and Electronics in Agriculture*, vol. 119, pp. 133 – 141, 2015.

[6] C. M. Bishop, *Pattern Recognition and Machine Learning*. Springer, 2006.

[7] D. M. Sheen, D. L. McMakin, and T. E. Hall, "Three-dimensional millimeter-wave imaging for concealed weapon detection," *IEEE Transactions on Microwave Theory and Techniques*, vol. 49, no. 9, pp. 1581–1592, 2001.

[8] M. Lazebnik, D. Popovic, L. McCartney, C. B. Watkins, M. J. Lindstrom, J. Harter, S. Sewall, T. Ogilvie, A. Magliocco, T. M. Breslin *et al.*, "A large-scale study of the ultrawideband microwave dielectric properties of normal, benign and malignant breast tissues obtained from cancer surgeries," *Physics in Medicine & Biology*, vol. 52, no. 20, p. 6093, 2007.

[9] R. J. Halter, T. Zhou, P. M. Meaney, A. Hartov, R. J. B. Jr, K. M. Rosenkranz, W. A. Wells, C. A. Kogel, A. Borsic, E. J. Rizzo, and K. D. Paulsen, "The correlation of in vivo and ex vivo tissue dielectric properties to validate electromagnetic breast imaging: initial clinical experience," *Physiological Measurement*, vol. 30, no. 6, p. S121, 2009.

[10] J. LoVetri, M. Asefi, C. Gilmore, and I. Jeffrey, "Innovations in electromagnetic imaging technology: The stored-grain-monitoring case," *IEEE Antennas and Propagation Magazine*, 2020.

[11] C. Gilmore, M. Asefi, J. Paliwal, and J. LoVetri, "Industrial scale electromagnetic grain bin monitoring," *Computers and Electronics in Agriculture*, vol. 136, pp. 210 – 220, 2017.

[12] K. Nemez, "A faceted chamber for magnetic field microwave breast imaging," Master's thesis, 2017.

[13] K. Brown, "Implementation of parallel 3-d dgm-csi and dgm-gni for electromagnetic imaging applications," Master's thesis, 2019.

[14] A. Zakaria, "The finite-element contrast source inversion method for microwave imaging applications," Master's thesis, 2012.

[15] I. Jeffrey, N. Geddert, K. Brown, and J. LoVetri, "The time-harmonic discontinuous galerkin method as a robust forward solver for microwave imaging applications," *Progress in Electromagnetics Research*, vol. 154, pp. 1–21, 2015.

[16] J. Jin, "The finite element method in electromagnetics," *New York: Wiley*, 1993.

[17] A. Abubakar, "2.5d forward and inverse modeling for interpreting low-frequency electromagnetic measurements," *Geophysics*, vol. 73, no. 4, pp. 165–177, 2008.

[18] A. Zakaria, A. Baran, and J. LoVetri, "Estimation and use of prior information in femcsi for biomedical microwave tomography," *IEEE Antennas and Wireless Propagation Letters*, vol. 11, pp. 1606–1609, 2012.

[19] D. Kurrant, A. Baran, J. LoVetri, and E. Fear, "Integrating prior information into microwave tomography part 1: Impact of detail on image quality," *Medical Physics*, vol. 44, no. 12, pp. 6461–6481, 2017.

[20] P. Solin, K. Segeth, and I. Dolezel, "Higher-order finite element methods," *Progress in Electromagnetics Research*, 2004.

[21] J. Hadamard, "Lectures on cauchys problem in linear partial differential equations," *New Haven Yale University Press*, 1923.

[22] X. Chen, *Computational methods for electromagnetic inverse scattering*. Wiley Online Library, 2018.

[23] A. Golnabi, P. Meaney, N. Epstein, and K. Paulsen, "Microwave imaging for breast cancer detection: advances in three–dimensional image reconstruction," *Conf Proc IEEE Eng Med Biol Soc*, p. 5730?5733, 2011.

[24] P. M. van den Berg and R. E. Kleinman, "A contrast source inversion method," *Inverse Problems*, vol. 13, no. 6, p. 1607, 1997.

[25] N. Joachimowicz, C. Pichot, and J.-P. Hugonin, "Inverse scattering: An iterative numerical method for electromagnetic imaging," *IEEE Transactions on Antennas and Propagation*, vol. 39, no. 12, pp. 1742–1753, 1991.

[26] P. Mojabi and J. LoVetri, "Overview and classification of some regularization techniques for the gauss-newton inversion method applied to inverse scattering problems," *IEEE Transactions on Antennas and Propagation*, vol. 57, no. 9, pp. 2658–2665, 2009.

[27] P. M. Van Den Berg, A. Abubakar, and J. Fokkema, "Multiplicative regularization for contrast profile inversion," *Radio Science*, vol. 38, pp. 1–10, 2003.

[28] M. Asefi, A. Baran, and J. LoVetri, "An experimental phantom study for air-based quasi-resonant microwave breast imaging," *IEEE Transactions on Microwave Theory and Techniques*, 2019.

[29] M. Bertero and P. Boccacc, *Introduction to Inverse Problems in Imaging*. U.K.: IOP Publishing, 1998.

[30] A. Baran, D. Kurrant, E. Fear, and J. LoVetri, "Integrating prior information into microwave tomography part 2: Impact of errors in prior information on microwave tomography image quality," *Medical Physics*, vol. 44, no. 12, pp. 6482–6503, 2017.

[31] A. H. Golnabi, P. M. Meaney, S. D. Geimer, and K. D. Paulsen, "3-d microwave tomography using the soft prior regularization technique: Evaluation in anatomically realistic mri-derived numerical breast phantoms," *IEEE Transactions on Biomedical Engineering*, vol. 66, no. 9, pp. 2566–2575, Sep. 2019.

[32] O. TG, "Breast imaging artifacts," *Radiol Technol*, vol. 87, 2015.

[33] I. Goodfellow, Y. Bengio, and A. Courville, *Deep Learning*. MIT Press, 2016, http://www.deeplearningbook.org.

[34] K. Simonyan and A. Zisserman, "Very deep convolutional networks for large-scale image recognition," 2014.

[35] K. He, X. Zhang, S. Ren, and J. Sun, "Deep residual learning for image recognition," in *2016 IEEE Conference on Computer Vision and Pattern Recognition (CVPR)*, 2016, pp. 770–778.

[36] C. Szegedy, W. Liu, Y. Jia, P. Sermanet, S. E. Reed, D. Anguelov, D. Erhan, V. Vanhoucke, and A. Rabinovich, "Going deeper with convolutions," *CoRR*, vol. abs/1409.4842, 2014. [Online]. Available: http://arxiv.org/abs/1409.4842

[37] O. Ronneberger, P. Fischer, and T. Brox, "U-net: Convolutional networks for biomedical image segmentation," *ArXiv*, vol. abs/1505.04597, 2015.

[38] J. Schlemper, J. Caballero, J. V. Hajnal, A. N. Price, and D. Rueckert, "A deep cascade of convolutional neural networks for dynamic mr image reconstruction," *IEEE Transactions on Medical Imaging*, vol. 37, no. 2, pp. 491–503, 2018.

[39] A. S. Lundervold and A. Lundervold, "An overview of deep learning in medical imaging focusing on mri," *Zeitschrift für Medizinische Physik*, vol. 29, no. 2, pp. 102 – 127, 2019, special Issue: Deep Learning in Medical Physics. [Online]. Available: http://www.sciencedirect.com/science/article/pii/S0939388918301181

[40] O. Ronneberger, P. Fischer, and T. Brox, "U-net: Convolutional networks for biomedical image segmentation," *CoRR*, vol. abs/1505.04597, 2015. [Online]. Available: http://arxiv.org/abs/1505.04597

[41] G. Wang, W. Li, M. A. Zuluaga, R. Pratt, P. A. Patel, M. Aertsen, T. Doel, A. L. David, J. Deprest, S. Ourselin, and T. Vercauteren, "Interactive medical image segmentation using deep learning with image-specific fine tuning," *IEEE Transactions on Medical Imaging*, vol. 37, no. 7, pp. 1562–1573, July 2018.

[42] H. Shin, H. R. Roth, M. Gao, L. Lu, Z. Xu, I. Nogues, J. Yao, D. Mollura, and R. M. Summers, "Deep convolutional neural networks for computer-aided detection: Cnn architectures, dataset characteristics and transfer learning," *IEEE Transactions on Medical Imaging*, vol. 35, no. 5, pp. 1285–1298, May 2016.

[43] M. T. McCann, K. H. Jin, and M. Unser, "Convolutional neural networks for inverse problems in imaging: A review," *IEEE Signal Processing Magazine*, vol. 34, no. 6, pp. 85–95, Nov 2017.

[44] Y. Xie, Y. Xia, J. Zhang, Y. Song, D. Feng, M. Fulham, and W. Cai, "Knowledge-based collaborative deep learning for benign-malignant lung nodule classification on chest ct," *IEEE Transactions on Medical Imaging*, vol. 38, no. 4, pp. 991–1004, April 2019.

[45] B. Zhu, J. Z. Liu, S. F. Cauley, B. R. Rosen, and M. S. Rosen, "Image reconstruction by domain-transform manifold learning," *Nature*, vol. 555, p. 487?492, 2018.

[46] W. Zhao, H. Wang, H. Gemmeke, K. W.A.van Dongen, T. Hopp, and J. Hesser, "Ultrasound transmission tomography image reconstruction with fully convolutional neural network," *IEEE TRANSACTIONS ON MEDICAL IMAGING*, 2017.

[47] L. June-Goo, J. Sanghoon, C. Young-Won, L. Hyunna, K. Guk Bae, S. Joon Beom, and K. Namkug, "Deep learning in medical imaging: General overview," *kjr*, vol. 18, no. 4, pp. 570–584, 2017. [Online]. Available: http://www.e-sciencecentral.org/articles/?scid=1027354

[48] G. Litjens, T. Kooi, B. E. Bejnordi, A. A. A. Setio, F. Ciompi, M. Ghafoorian, J. A. van der Laak, B. van Ginneken, and C. I. Sánchez, "A survey on deep learning in medical image analysis," *Medical Image Analysis*, vol. 42, pp. 60 – 88, 2017. [Online]. Available: http://www.sciencedirect.com/science/article/pii/S1361841517301135

[49] P. M. Meaney, K. D. Paulsen, S. D. Geimer, S. A. Haider, and M. W. Fanning, "Quantification of 3-d field effects during 2-d microwave imaging," *IEEE Transactions on Biomedical Engineering*, vol. 49, no. 7, pp. 708–720, July 2002.

[50] P. Mojabi and J. LoVetri, "Composite tissue-type and probability image for ultrasound and microwave tomography," *IEEE Journal on Multiscale and Multiphysics Computational Techniques*, vol. 1, pp. 26–35, 2016.

[51] M. Hughson, J. LoVetri, and I. Jeffrey, "Microwave breast imaging incorporating material property dependencies," in *2019 IEEE MTT-S International Microwave Symposium (IMS)*, 2019, pp. 1450–1453.

[52] S. Caorsi and P. Gamba, "Electromagnetic detection of dielectric cylinders by a neural network approach," *IEEE Transactions on Geoscience and Remote Sensing*, vol. 37, no. 2, pp. 820–827, 1999.

[53] P. Shah, G. Chen, and M. Moghaddam, "Learning nonlinearity of microwave imaging through deep learning," in *2018 IEEE International Symposium on Antennas and Propagation USNC/URSI National Radio Science Meeting*, 2018, pp. 699–700.

[54] B. Gerazov and R. C. Conceicao, "Deep learning for tumour classification in homogeneous breast tissue in medical microwave imaging," in *IEEE EUROCON 2017-17th International Conference on Smart Technologies*. IEEE, 2017, pp. 564–569.

[55] L. Wang and J. Xu, "Deep convolutional neural networks for breast image analysis on holographic microwave imaging," 11 2018, p. V003T04A029.

[56] L. Li, L. G. Wang, F. L. Teixeira, C. Liu, A. Nehorai, and T. J. Cui, "Deepnis: Deep neural network for nonlinear electromagnetic inverse scattering," *IEEE Transactions on Antennas and Propagation*, vol. 67, no. 3, p. 1819?1825, Mar 2019. [Online]. Available: http://dx.doi.org/10.1109/TAP.2018.2885437

[57] K. Edwards, N. Geddert, K. Krakalovich, R. Kruk, M. Asefi, J. Lovetri, C. Gilmore, and I. Jeffrey, "Stored grain inventory management using neural-network-based parametric electromagnetic inversion," *IEEE Access*, vol. 8, pp. 207 182–207 192, 2020.

[58] H. M. Yao, W. E. I. Sha, and L. Jiang, "Two-step enhanced deep learning approach for electromagnetic inverse scattering problems," *IEEE Antennas and Wireless Propagation Letters*, vol. 18, no. 11, pp. 2254–2258, 2019.

[59] Z. Wei and X. Chen, "Deep-learning schemes for full-wave nonlinear inverse scattering problems," *IEEE Transactions on Geoscience and Remote Sensing*, vol. 57, no. 4, pp. 1849–1860, 2019.

[60] P. Ran, Y. Qin, and D. Lesselier, "Electromagnetic imaging of a dielectric microstructure via convolutional neural networks," in *2019 27th European Signal Processing Conference (EUSIPCO)*, 2019, pp. 1–5.

[61] X. Chen, Z. Wei, M. Li, , and P. Rocca, "A review of deep learning approaches for inverse scattering problems (invited review),," *Progress In Electromagnetics Research*, vol. 167, pp. 67–81, 2020.

[62] M. Pastorino, *Microwave imaging*. John Wiley & Sons, 2010.

[63] M. Haynes and M. Moghaddam, "Large-domain, low-contrast acoustic inverse scattering for ultrasound breast imaging," *IEEE Transactions on Biomedical Engineering*, vol. 57, no. 11, pp. 2712–2722, Nov 2010.

[64] M. Sak, N. Duric, P. Littrup, M. Sherman, and G. Gierach, "Ultrasound tomography imaging with waveform sound speed: Parenchymal changes in women undergoing tamoxifen therapy," in *Medical Imaging 2017: Ultrasonic Imaging and Tomography*, vol. 10139, 2017, p. 101390W.

[65] J.-C. Bolomey, *Crossed Viewpoints on Microwave-Based Imaging for Medical Diagnosis: From Genesis to Earliest Clinical Outcomes*. Cham: Springer International Publishing, 2018, pp. 369–414.

[66] D. O'Loughlin, M. J. O'Halloran, B. M. Moloney, M. Glavin, E. Jones, and M. A. Elahi, "Microwave breast imaging: Clinical advances and remaining challenges," *IEEE Transactions on Biomedical Engineering*, 2018.

[67] M. T. Bevacqua, G. G. Bellizzi, T. Isernia, and L. Crocco, "A method for effective permittivity and conductivity mapping of biological scenarios via segmented contrast source inversion," vol. 164, 2019, pp. 1–15.

[68] M. Omer, P. Mojabi, D. Kurrant, J. LoVetri, and E. Fear, "Proof-of-concept of the incorporation of ultrasound-derived structural information into microwave radar imaging," *IEEE Journal on Multiscale and Multiphysics Computational Techniques*, vol. 3, pp. 129–139, 2018.

[69] N. Abdollahi, D. Kurrant, P. Mojabi, M. Omer, E. Fear, and J. LoVetri, "Incorporation of ultrasonic prior information for improving quantitative microwave imaging of breast," *IEEE Journal on Multiscale and Multiphysics Computational Techniques*, vol. 4, pp. 98–110, 2019.

[70] Z. Wei and X. Chen, "Deep-learning schemes for full-wave nonlinear inverse scattering problems," *IEEE Transactions on Geoscience and Remote Sensing*, vol. 57, no. 4, pp. 1849–1860, April 2019.

[71] K. H. Jin, M. T. McCann, E. Froustey, and M. Unser, "Deep convolutional neural network for inverse problems in imaging," *CoRR*, vol. abs/1611.03679, 2016. [Online]. Available: http://arxiv.org/abs/1611.03679

[72] K. H. Jin, M. T. McCann, E. Froustey, and M. Unser, "Deep convolutional neural network for inverse problems in imaging," *IEEE Transactions on Image Processing*, vol. 26, no. 9, pp. 4509–4522, Sep. 2017.

[73] Y. A. Rahama, O. A. Aryani, U. A. Din, M. A. Awar, A. Zakaria, and N. Qaddoumi, "Novel microwave tomography system using a phased-array antenna," *IEEE Transactions on Microwave Theory and Techniques*, vol. 66, no. 11, pp. 5119–5128, Nov 2018.

[74] I. T. Rekanos, "Neural-network-based inverse-scattering technique for online microwave medical imaging," *IEEE transactions on magnetics*, vol. 38, no. 2, pp. 1061–1064, 2002.

[75] L. Li, L. G. Wang, F. L. Teixeira, C. Liu, A. Nehorai, and T. J. Cui, "Deepnis: Deep neural network for nonlinear electromagnetic inverse scattering," *IEEE Transactions on Antennas and Propagation*, vol. 67, no. 3, pp. 1819–1825, March 2019.

[76] A. Zakaria, C. Gilmore, and J. LoVetri, "Finite-element contrast source inversion method for microwave imaging," *Inverse Problems*, vol. 26, no. 11, p. 115010, 2010.

[77] M. Omer and E. C. Fear, "Automated 3d method for the construction of flexible and reconfigurable numerical breast models from mri scans," *Medical & biological engineering & computing*, vol. 56, no. 6, pp. 1027–1040, 2018.

[78] C. Trabelsi, O. Bilaniuk, Y. Zhang, D. Serdyuk, S. Subramanian, J. F. Santos, S. Mehri, N. Rostamzadeh, Y. Bengio, and C. Pal, "Deep complex networks," 2018, arxiv:1705.09792. [Online]. Available: https://iclr.cc/Conferences/2018/Schedule?showEvent=2

[79] X. Glorot and Y. Bengio, "Understanding the difficulty of training deep feedforward neural networks," in *In Proceedings of the International Conference on Artificial Intelligence and Statistics (AISTATS'10). Society for Artificial Intelligence and Statistics*, 2010.

[80] C. M. Bishop, *Pattern Recognition and Machine Learning*. Springer, 2006.

[81] A. Abubakar, P. M. van den Berg, and J. J. Mallorqui, "Imaging of biomedical data using a multiplicative regularized contrast source inversion method," *IEEE Transactions on Microwave Theory and Techniques*, vol. 50, no. 7, pp. 1761–1771, July 2002.

[82] E. Kang, J. Min, and J. C. Ye, "A deep convolutional neural network using directional wavelets for low-dose x-ray ct reconstruction," *Medical Physics*, vol. 44, no. 10, pp. e360–e375, 2017. [Online]. Available: https://aapm.onlinelibrary.wiley.com/doi/abs/10.1002/mp.12344

[83] Y. Han, J. J. Yoo, and J. C. Ye, "Deep residual learning for compressed sensing CT reconstruction via persistent homology analysis," *CoRR*, vol. abs/1611.06391, 2016. [Online]. Available: http://arxiv.org/abs/1611.06391

[84] Y. Han, J. Yoo, H. H. Kim, H. J. Shin, K. Sung, and J. C. Ye, "Deep learning with domain adaptation for accelerated projection-reconstruction mr," *Magnetic Resonance in Medicine*, vol. 80, no. 3, pp. 1189–1205, 2018. [Online]. Available: https://onlinelibrary.wiley.com/doi/abs/10.1002/mrm.27106

[85] V. Khoshdel, A. Ashraf, and J. LoVetri, "Enhancement of multimodal microwave-ultrasound breast imaging using a deep-learning technique," *Sensors*, 2019.

[86] S. P. Rana, M. Dey, G. Tiberi, L. Sani, A. Vispa, G. Raspa, M. Duranti, M. Ghavami, and S. Dudley, "Machine learning approaches for automated lesion

detection in microwave breast imaging clinical data," *Scientific reports*, vol. 9, pp. 1–12, 2019.

[87] J. Cano, Gil and, A. Fasoula, L. Duchesne, and G. Bernard, "Wavelia breast imaging: The optical breast contour detection subsystem," *Applied Science*, vol. 10, p. 1234, 2020.

[88] W. C. Chew and Y. M. Wang, "Reconstruction of two-dimensional permittivity distribution using the distorted born iterative method," *IEEE Transactions on Medical Imaging*, vol. 9, no. 2, pp. 218–225, 1990.

[89] A. Franchois and C. Pichot, "Microwave imaging-complex permittivity reconstruction with a levenberg-marquardt method," *IEEE Transactions on Antennas and Propagation*, vol. 45, no. 2, pp. 203–215, Feb 1997.

[90] A. Bulyshev, S. Semenov, A. Souvorov, R. Svenson, A. Nazarov, Y. Sizov, and G. Tatsis, "Computational modeling of three-dimensional microwave tomography of breast cancer," *IEEE Transactions on Biomedical Engineering*, vol. 48, no. 9, pp. 1053–1056, Sept. 2001.

[91] P. M. Meaney, S. D. Geimer, and K. D. Paulsen, "Two-step inversion with a logarithmic transformation for microwave breast imaging," *Medical Physics*, vol. 44, no. 8, pp. 4239–4251, 2017. [Online]. Available: https://aapm.onlinelibrary.wiley.com/doi/abs/10.1002/mp.12384

[92] P. van den Berg, A. Abubakar, and J. Fokkema, "Multiplicative regularization for contrast profile inversion," *Radio Science*, vol. 38, pp. 23.1–23.10, 2003.

[93] A. Zakaria, I. Jeffrey, and J. LoVetri, "Full-vectorial parallel finite-element contrast source inversion method," *Progress In Electromagnetics Research.*, vol. 142, pp. 463–483, 2013.

[94] K. Nemez, A. Baran, M. Asefi, and J. LoVetri, "Modeling error and calibration techniques for a faceted metallic chamber for magnetic field microwave imaging," *IEEE Trans. Microw. Theory Techn.*, Accepted Mar. 2017.

[95] A. Krizhevsky, I. Sutskever, and G. E. Hinton, "Imagenet classification with deep convolutional neural networks," *Advances in Neural Information Processing Systems 25*, pp. 1097–1105, 2012. [Online]. Available: http://papers.nips.cc/paper/4824-imagenet-classification-with-deep-convolutional-neural-networks.pdf

[96] I. Goodfellow, Y. Bengio, and A. Courville, *Deep Learning*. MIT Press, 2016, http://www.deeplearningbook.org.

[97] J. Hanley and B. McNeil, "The meaning and use of the area under a receiver operating characteristic (roc) curve," *Radiology*, vol. 43, pp. 29–36, 1982.

[98] S. Lambot, E. C. Slob, I. van den Bosch, B. Stockbroeckx, and M. Vanclooster, "Modeling of ground-penetrating radar for accurate characterization of subsurface electric properties," *IEEE Transactions on Geoscience and Remote Sensing*, vol. 42, no. 11, pp. 2555–2568, 2004.

[99] D. S. Jayasand N. D. G. Whiteand W. E. Muirand Eds. New York and M. Dekker, "The stored-grain ecosystem," *Stored Grain Ecosystems*, vol. 1, pp. 1–32, 1995.

[100] V. Khoshdel, M. Asefi, A. A, and J. LoVetri, "Full 3d microwave breast imaging using a deep-learning technique," *Journal of Imaging*, vol. 6, no. 8, p. 80, 2020.

[101] G. Chen, P. Shah, J. Stang, and M. Moghaddam, "Learning-assisted multimodality dielectric imaging," *IEEE Transactions on Antennas and Propagation*, vol. 68, no. 3, pp. 2356–2369, 2020.

[102] S. O. Nelson, "Dielectric properties of agricultural products-measurements and applications," *IEEE Transactions on Electrical Insulation*, vol. 26, no. 5, pp. 845–869, 1991.

[103] D. P. Kingma and J. Ba, "Adam: A method for stochastic optimization," 2014. [Online]. Available: http://arxiv.org/abs/1412.6980

[104] K. Edwards, K. Krakalovich, R. Kruk, V. Khoshdel, J. LoVetri, C. Gilmore, and I. Jeffrey, "The implementation of neural networks for phaseless parametric inversion," in *URSI GASS 2020*, 2020.

[105] S. Kazeminia, C. Baur, A. Kuijper, B. van Ginneken, N. Navab, S. Albarqouni, and A. Mukhopadhyay, "Gans for medical image analysis," *Artificial Intelligence in Medicine*, vol. 109, p. 101938, 2020.

[106] I. Goodfellow, "Nips 2016 tutorial: Generative adversarial networks," 2017.